日本磁気学会
ISSN 2432-0250
Journal of the Magnetics Society of Japan
Electronic Journal URL: https://www.jstage.jst.go.jp/browse/msjmag

Vol.45 No.4 2021

Journal

JOURNAL OF THE MAGNETICS SOCIETY OF JAPAN

Vol.45 No.4 2021

日本磁気学会

ISSN 2432-0250

HP: http://www.magnetics.jp/ e-mail: msj@bj.wakwak.com

Electronic Journal: http://www.jstage.jst.go.jp/browse/msjmag

世界初！
高温超電導型VSM

新製品

世界初*、高温超電導マグネットをVSMに採用することで
測定速度 当社従来機1/20を実現。
0.5mm cube磁石のBr, HcJ高精度測定が可能と
なりました。
*2014年7月 東英工業調べ

測定結果例

高温超電導VSMによるNdFeB(sint.) 0.5mm cube BHカーブ

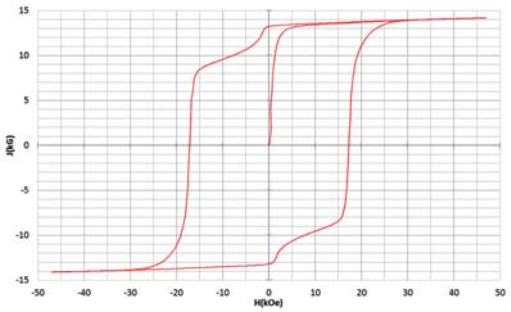

磁化測定レンジ：0.2emu
Br = 13.2kG　　HcJ = 17.2kOe

高温超電導VSMによるNdFeB(sint.) 1mm cube BHカーブ

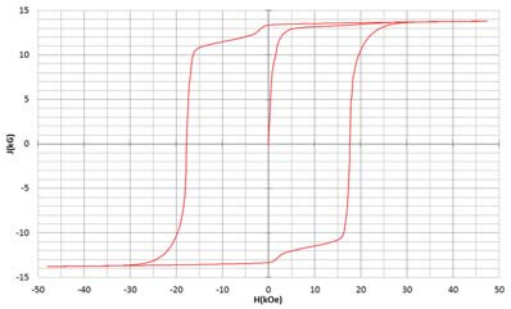

磁化測定レンジ：2emu
Br = 13.3kG　　HcJ = 17.7kOe

高温超電導VSMによるNdFeB(sint.) 4mm cube BHカーブ

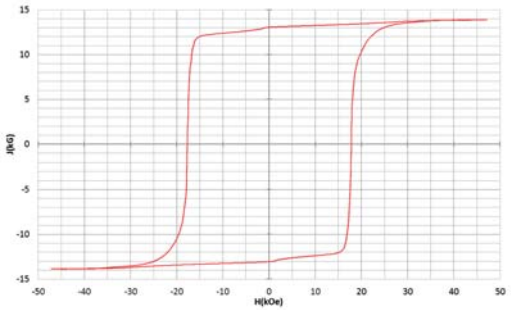

磁化測定レンジ：100emu
Br = 13.1kG　　HcJ = 17.8kOe

高速測定を実現

高温超電導マグネット採用により、高速測定を実現しました。Hmax= 5Tesla, Full Loop 測定が2分で可能です。
（当社従来機：Full Loop測定　40分）

小試料のBr,HcJ高精度測定

0.5mm cube 磁石のBr,HcJ高精度測定ができ、表面改質領域を切り出しBr,HcJの強度分布等、微小変化量の比較測定が可能です。
また、試料の加工劣化の比較測定が可能です。

試料温度可変測定

−50℃～+200℃温度可変UNIT（オプション）

磁界発生部の小型化

マグネットシステム部寸法：0.8m×0.3m×0.3m

TOEI 東英工業株式会社
http://www.toeikogyo.co.jp
〒194-0035 東京都町田市忠生1-8-13
TEL：042-791-1211 FAX：042-792-0490
E-mail : sales@toeikogyo.co.jp

Journal of the Magnetics Society of Japan
Vol. 45, No. 4

Electronic Journal URL: https://www.jstage.jst.go.jp/browse/msjmag

CONTENTS

J. Magn. Soc. Jpn., **45**, 75-78 (2021)

Letter

Estimation of magnetic domain size in chiral antiferromagnet Mn_3Ir by the anomalous Hall measurements

Yuta Kobayashi, Tetsuya Ikebuchi, Yoichi Shiota, Teruo Ono*, and Takahiro Moriyama

Institute for Chemical Research, Kyoto University, *Gokasho Uji, Kyoto 611-0011, Japan*
*Center for Spintronics Research Network (CSRN), Graduate School of Engineering Science, Osaka University, *Toyonaka, Osaka 560-8531, Japan*

Chiral antiferromagnets have recently been drawing attention due to their unique magnetic transport properties such as the giant anomalous Hall effect. We previously reported an experimental demonstration of the giant anomalous Hall effect in the chiral antiferromagnet Mn_3Ir thin films with quite blunt hysteresis curves suggesting a large distribution of magnetic properties associated with magnetic domains. In this work, we measured the anomalous Hall effect and its hysteresis curve in the Mn_3Ir of various device sizes. By comparing the experimental data with our developed statistical model, we characterize a distribution of the magnetic domain size in our Mn_3Ir films.

Keywords: anomalous Hall effect, chiral antiferromagnet, Mn_3Ir, magnetic domain, thin film, statistical analysis

Chiral antiferromagnets, a new class of non-collinear antiferromagnets, have recently been drawing attention owing to their intriguing transport properties. The non-collinear magnetic structure with broken space inversion symmetry causes a large Berry curvature which gives rise to a giant anomalous Hall effect (AHE)[1),2)], anomalous Nernst effect (ANE)[3)-6)], and magneto-optical Kerr effect[7)-9)]. Chiral antiferromagnets have been investigated in the context of not only the topological physics[10),11)], but also antiferromagnetic spintronics[12)] where their small net magnetization[1)] and the high-speed magnetic response[13)] are advantageous for spintronic devices such as spin-torque magnetic memories[14)-16)]. Most of these leading-edge researches have been successful with a particular chiral antiferromagnet, $D0_{19}$-ordered Mn_3Sn, which is one of the chiral antiferromagnetic compounds Mn_3X (X = Sn, Ge, Ga, Ir, Pt, and Rh) family[17)-23)]. Mn_3Ir which is focused on in this paper is much less investigated although the relatively large anomalous Hall conductivity is predicted among the Mn_3X family[22)].

We previously reported the fabrication of $L1_2$-ordered Mn_3Ir thin films and the demonstration of the giant AHE. The AHE hysteresis curves emerges due to the reversal of the chiral domain associating with the reversal of the small net magnetization[24)]. As $L1_2$-Mn_3Ir have a large magnetocrystalline anisotropy due to a large spin-orbit interaction of Ir[25),26)], the coercive field, or the switching field, is found larger than several Tesla[24)]. Our previously observed hysteresis curves of the anomalous Hall effect were quite blunt with a large switching field, suggesting that the magnetic reversal is not uniform but is driven by magnetic domains. To further explore the potential of the Mn_3Ir as a chiral antiferromagnet, it is important to understand the magnetic reversal giving rise to the AHE[27),28)].

In this work, we investigate the hysteresis curves of AHE in Mn_3Ir to characterize the "magnetic domain" size within which the magnetizations uniformly rotate to give rise to the AHE[29)]. We took a distribution of the hysteresis curves for various sizes of the Hall cross devices which should be significantly affected by the relative size of the magnetic domains to the device size. Assuming there are two key distributions; one is the magnetic domain size distribution and the other is the AHE distribution in each magnetic domain. For instance, in the limit where the magnetic domain is much larger than the device size, the distribution of the hysteresis curves simply reflects the AHE distribution. On the other hand, in the opposite limit, the AHE distribution would be averaged out by the many domains and would be smaller. The device size dependence of the distribution was analyzed by a statistical model based on the above assumption to determine the domain size.

Mn_3Ir thin films of thickness 20 nm were grown by magnetron sputtering on a thermally oxidized Si substrate at the substrate temperature T_s = 700 °C in the

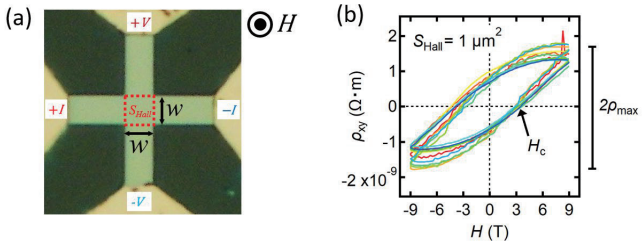

Fig. 1. (a) The Hall cross device. w is the channel width of the Hall cross bar. (b) The transverse resistivity ρ_{xy} for the Hall cross area S_{Hall} = 1μm² as a function of magnetic field.

Corresponding author:
T. Moriyama (e-mail: mtaka@scl.kyoto-u.ac.jp).

chamber with the base pressure of 1.5×10^{-5} Pa. The fabrication process is identical to our previous report[24]. During the deposition, we rotate the sample holder along its normal axis to ensure a uniform composition and thickness. A plate of arc-melted Mn75%-Ir alloy was used for the sputtering target. SiO_2 of thickness 5 nm was deposited on top of the Mn_3Ir film to prevent the oxidation. For the transport measurements, the films were photolithographically patterned into a Hall cross structure with the channel width w ranging from 1 μm to 10 μm (Fig. 1(a)). Hall measurements were carried out at room temperature with an external field applied perpendicular to the sample plane, by using the current-spinning technique to remove any parasitic offset voltage due to geometrical imperfections of the Hall cross structure[30]. Any residual offset should be intrinsically linked to the material property in response to the magnetic field.

Figure 1(b) shows transverse resistivity ρ_{xy} as a function of external field H of typical Hall cross area S_{Hall} $(=w^2)$ equal to 1 μm², the Hall cross area which is relevant to the anomalous Hall effect (see Fig. 1 (a)). We measured at least 10 different devices for each Hall cross area S_{Hall} =1, 4, 9, 25, 49, and 100 μm².

Since the hysteresis curves do not saturate with the external magnetic field available in the lab (< 9 Tesla), all the AHE hysteresis curves are considered as a minor loop. Therefore, the coercive field H_c is not a good physical quantity and does not directly reflect the distribution of the coercive field in each domain $H_{\mathrm{c,domain}}$. We instead take the maximum ρ_{xy} for each hysteresis curve to evaluate a distribution of the hysteresis curves, as,

$$\rho_{\max} = \frac{\rho_{xy}(9\mathrm{T}) - \rho_{xy}(-9\mathrm{T})}{2} \qquad (1)$$

The histogram of $\rho_{\max}$ from which we take the standard deviation is shown in Fig. 2.

We now explain the statistical model to estimate the magnetic domain size from the standard deviation of $\rho_{\max}$ (Fig. 3). The model is developed based on two critical assumptions; (i) the magnetic domain size has a normal distribution in the blanket film (ii) each domain has an expected hysteresis curve with normally populated coercive field $H_{\mathrm{c,domain}}$. With the assumption (i), we can

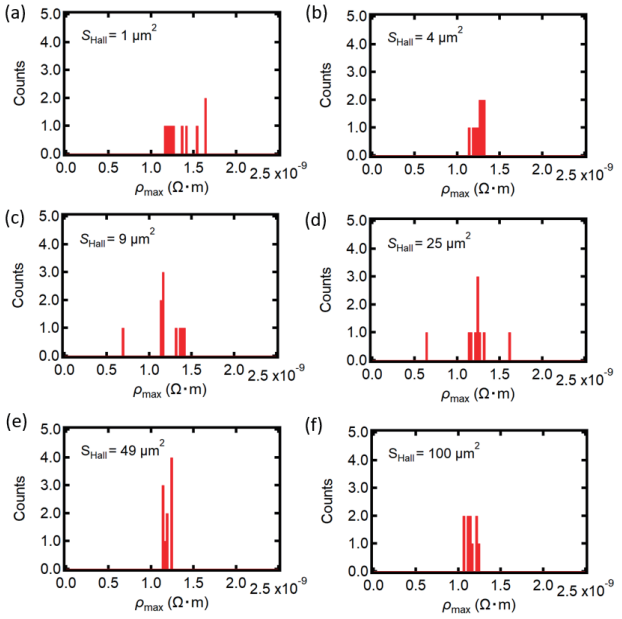

Fig. 2. Histogram of $\rho_{\max} = \frac{\rho_{xy}(9\mathrm{T}) - \rho_{xy}(-9\mathrm{T})}{2}$ for various Hall cross area S_{Hall}.

hypothesize that our Hall cross pattern cut out the magnetic domain(s) on the blanket film having distribution of the domain size. We then simulate the hysteresis curve by calculating the sum of the AHE hysteresis curves arisen by each magnetic domain based on the assumption (ii).

With this framework, the simulation is performed by the following procedure. First, sizes of the magnetic domains $S_{domain,k}$ is assumed to be normally populated in the blanket film (Assumption (i)) with the mean size $S_{domain,mean}$ and the standard deviation $S_{domain,dev}$. We then randomly and repeatedly pick up $S_{domain,k}$ from the population until the Hall cross is fully filled, i.e. $\sum_{k=1}^{n} S_{domain,k} \geqq S_{Hall}$ where the repetition number n is the number of magnetic domains occupying the Hall cross. Second, we stochastically assign a hysteresis curve to the magnetic domain(s) from a normally distributed population of the hysteresis curves characterized by coercive field $H_{\mathrm{c,domain}}$, the mean $H_{\mathrm{c,mean}}$, and the standard deviation $H_{\mathrm{c,dev}}$. For convenience, we utilize

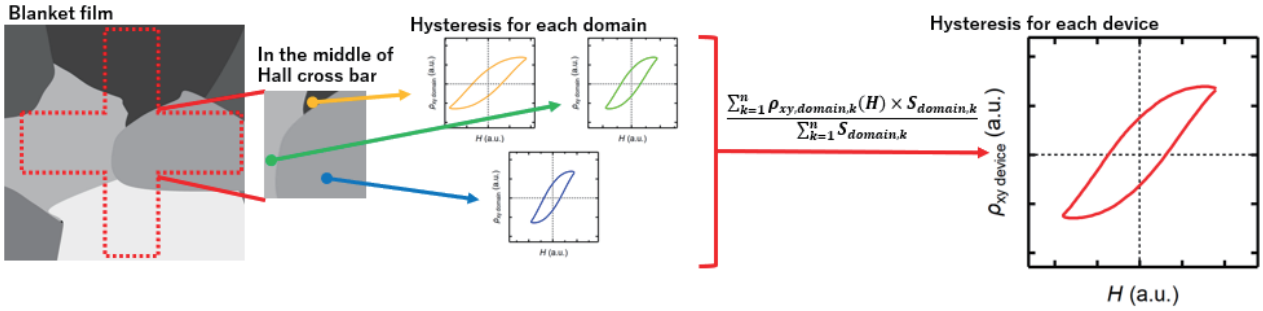

Fig. 3. The statistical model and procedure for estimating the magnetic domain size from the standard deviation of $\rho_{\max}$.

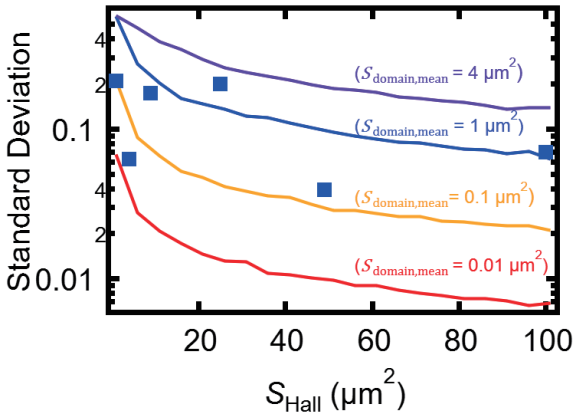

Fig. 4. Normalized standard deviation of the simulated results D_{sim} (solid lines) and the experimental result D_{obs} (square points) as a function of S_{Hall}. $S_{domain,dev}$ is set to half of S_{Hall}.

the error function $\mathrm{erf}(H) = \frac{2}{\sqrt{\pi}}\int_0^H e^{-t^2}dt$ to represent the hysteresis curve as,

$$\rho_{xy,domain,k}(H) = \mathrm{erf}\left(N \times \left(H - H_{c,domain}\right)\right) \quad (-9\ \mathrm{T} \leqq H \leqq 9\ \mathrm{T}) \quad (2)$$

where $\rho_{xy,domain,k}(H)$ is a pseudo hysteresis function of the AHE taking values ranging from -1 to 1 which reproduces a half of the AHE hysteresis curve. N is an adjustable coefficient to mimic the hysteresis curve obtained in the experiment. We should note that the use of the error function is not necessary condition but can be any function if it can reasonably mimic the hysteresis curve. Considering that the saturation field of the AHE hysteresis curve is close to 24 T[24], we set the population of $\rho_{xy,domain,k}(H)$ with $H_{\mathrm{c,mean}}$ = 12 T and $H_{\mathrm{c,dev}}$ = 6 T. Coefficient N is set to 9.0×10^{-6}. We do not set any correlation between $\rho_{xy,domain,k}(H)$ and S_k. It is worthwhile to note that the function for each $\rho_{xy,domain,k}$ and coefficient N has little influence on the final results, since the aim of this model is to evaluate the distribution depending on relative size of magnetic domains to S_{Hall}. The AHE hysteresis curve of the Hall cross device is the sum of n hysteresis curves with a weight of the size of the magnetic domain as,

$$\rho_{xy,device}(H) = \frac{\sum_{k=1}^{n}\rho_{xy,domain,k}(H) \times S_{domain,k}}{\sum_{k=1}^{n} S_{domain,k}} \quad (3)$$

This procedure is iterated 1000 times to derive a distribution of $\rho_{xy,device}(9T)$. Since the average value of the measurement results and the simulation value are different, the standard deviation was normalized by dividing by the mean of $\rho_{xy,device}(9\mathrm{T})$.

Fig. 4 shows normalized standard deviation of simulated results D_{sim} and experimental results D_{obs} as a function of S_{Hall}. The solid line shows the D_{sim}, and the square points show the D_{obs}. D_{obs} is within the range of D_{sim} curves for S_{domain} = 0.01 ~ 4 μm^2, suggesting that the magnetic domains of $L1_2$-Mn_3Ir could be within the range of 0.01 to 4 μm^2. The estimated size of the magnetic domain is larger than previous reports[31] and this result suggests that the magnetic domains of Mn_3Ir could be observable by commonly used imaging method, e.g. magneto-optical Kerr effect. On the other hand, the general trend of the experimental results deviates so much from the expected D_{sim} curves. To increase the reliability of this model, we need to increase number of experimental samples. However, the nature of the present measurements which requires 9T magnetic field using the superconducting magnet does not allow to increase the number of samples further due to the time constrain. We emphasize that our model can be more reliably applied to broad range of magnetic materials when sufficient number of samples are taken.

In summary, we explored the Hall cross area dependence of anomalous Hall effect in $L1_2$-Mn_3Ir. By developing the statistical model, we attempted to estimate the magnetic domain size of the Mn_3Ir thin films. Although the detailed analysis revealed that the present number of samples cannot be sufficient to guarantee a good statistical confidence, the data infers that the magnetic domain size can range from 0.01 to 4 μm^2. The present result is a step forward to elucidate the magnetization process of the chiral antiferromagnets.

Acknowledgements This work was supported by JSPS KAKENHI Grant Numbers JP19K21972, JP19J21253, JP20H05665, JP20H00332, JP20K15161, and JP21H04562.

References

1) H. Chen, Q. Niu, and A.H. MacDonald, *Phys. Rev. Lett.* **112**, 017205 (2014).
2) S. Nakatsuji, N. Kiyohara, and T. Higo, *Nature* **527**, 212-215 (2015).
3) M M. Ikhlas, T. Tomita, T. Koretsune, M. Suzuki, D. Hamane, R. Arita, Y. Otani, and S. Nakatsuji, *Nature Physics* **13**, 1085-1090 (2017).
4) H. Narita, M. Ikhlas, M. Kimata, A. A. Nugroho, S. Nakatsuji, and Y. Otani, *Appl. Phys. Lett.* **111**. 202404 (2017).
5) C. Wuttke, F. Caglieris, S. Sykora, F. Scaravaggi, A. U. B. Wolter, K. Manna, V. Süss, C. Shekhar, C. Felser, B. Büchner, and C. Hess, *Phys. Rev. B* **100**, 085111 (2019).
6) H. Narita, T. Higo, M. Ikhlas, S. Nakatsuji, and Y. Otani, *Appl. Phys. Lett.* **116**, 072404 (2020).
7) T. Higo, H. Man, D. B. Gopman, L. Wu, T. Koretsune, O. van 't Erve, Y. P. Kabanov, D. Rees, Y. Li, M. Suzuki, S. Patankar, M. Ikhlas, C. L. Chien, R. Arita, R. D. Shull, J. Orenstein, and S. Nakatsuji, *Nature Photonics* **12**, 73-78 (2018).
8) A. L. Balk, N. H. Sung, S. M. Thomas, P. F. S. Rosa, R. D. McDonald, J. D. Thompson, E. D. Bauer, F. Ronning, and S. A. Crooker, *Appl. Phys. Lett.* **114**, 032401 (2019).
9) M. Wu, H. Isshiki, T. Chen, T. Higo, S. Nakatsuji, and Y. Otani, *Appl. Phys. Lett.* **116**, 132408 (2020).
10) K. Kuroda, T. Tomita, M.-T. Suzuki, C. Bareille, A. A. Nugroho, P. Goswami, M. Ochi, M. Ikhlas, M. Nakayama, S. Akebi, R. Noguchi, R. Ishii, N. Inami, K. Ono, H. Kumigashira, A. Varykhalov, T. Muro, T. Koretsune, R.

Arita, S. Shin, Takeshi Kondo, and S. Nakatsuji, *Nature Materials* **16**, 1090-1095 (2017)
11) H. Yang, Y. Sun, Y. Zhang, W. Shi, S. S. P. Parkin, and B. Yan, *New J. Phys.* **19**, 015008 (2017).
12) V. Baltz, A. Manchon, M. Tsoi, T. Moriyama, T. Ono, and Y. Tserkovnyak, *Rev. Mod. Phys.* **90**, 015005 (2018).
13) T. Matsuda, N. Kanda, T. Higo, N. P. Armitage, S. Nakatsuji, and R. Matsunaga, *Nature Communication* **11**, 909 (2020).
14) H. Tsai, T. Higo, K. Kondou, T. Nomoto, A. Sakai, A. Kobayashi, T. Nakano, K. Yakushiji, R. Arita, S. Miwa, Y. Otani, and S. Nakatsuji, *Nature* **580**, 608-613 (2020).
15) T. Hajiria, S. Ishino, K. Matsuura, and H. Asano, *Appl. Phys. Lett.* **115**, 052403 (2019).
16) H. Tsai, T. Higo, K. Kondou, A. Kobayashi, T. Nakano, K. Yakushiji, S. Miwa, Y. Otani, and S. Nakatsuji, *AIP Advances* **11**, 045110 (2021).
17) A. K. Nayak, J. E. Fischer, Y. Sun, B. Yan, J. Karel, A. C. Komarek, C. Shekhar, N. Kumar, W. Schnelle, J. Kübler, C. Felser, and S. S. P. Parkin, *Sci. Adv.* **2** e1501870 (2016).
18) T. Higo, D. Qu, Y. Li, C. L. Chien, Y. Otani, and S. Nakatsuji, *Appl. Phys. Lett.* **113**, 202402 (2018).
19) N. An, M. Tang, S. Hu, H. Yang, W. Fan, S. Zhou, and X. Qiu, *Science China Physics, Mechanics & Astronomy* **63**, 297511 (2020).
20) A. Sakuma, R. Y. Umetsu, and K. Fukamichi, *Phys. Rev. B* **66**, 014432 (2020).
21) F. Hu, G. Xu, Y. You, Z. Zhang, Z. Xu, Y. Gong, Er. Liu, H. Zhang, E. Liu, W. Wang, and Feng Xu, *Journal of Applied Physics* **123**, 103902 (2018).
22) Y. Zhang, Y. Sun, H. Yang, J. Železný, S. P. P. Parkin, C. Felser, and B. Yan, *Phys. Rev. B* **95**, 075128 (2017).
23) Y. Kobayashi, T. Ikebuchi, H. Iwaki, Y. Shiota, T. Ono, and T. Moriyama, *Appl. Phys. Express* **13**, 073001 (2020).
24) H. Iwaki, M. Kimata, T. Ikebuchi, Y. Kobayashi, K. Oda, Y. Shiota, T. Ono, and T. Moriyama, *Appl. Phys. Lett.* **116**, 022408 (2020).
25) L. Szunyogh, B. Lazarovits, L. Udvardi, J. Jackson, and U. Nowak, *Phys. Rev. B* **79**, 020403(R) (2019).
26) S. Jenkins, R. W. Chantrell, T. J. Klemmer, and R. F. L. Evans, *Phys. Rev. B* **100**, 220405(R) (2019).
27) X. Li, C. Collignon, L. Xu, H. Zuo, A. Cavanna, U. Gennser, D. Mailly, B. Fauqué, L. Balents, Z. Zhu, and K. Behnia, *Nature Communications* **10**, 3021 (2019).
28) J. M. Taylor, A. Markou, E. Lesne, P. K. Sivakumar, C. Luo, F. Radu, P. Werner, C. Felser, and S. S. P. Parkin, *Phys. Rev. B* **101**, 094404 (2020).
29) H. Bai, W. Zhu, Y. You, X. Chen, X. Zhou, F. Pan, and C. Song, *Appl. Phys. Lett.* **117**, 052404 (2020).
30) T. Kosub, M. Kopte, F. Radu, O. G. Schmidt, and D. Makarov, *Phys. Rev. Lett.* **115**, 097201 (2015).
31) J.M. Taylor, E. Lesne, A. Markou, F. K. Dejene, P. K. Sivakumar, S. Pöllath, K. G. Rana, N. Kumar, C. Luo, H. Ryll, F. Radu, F. Kronast, P. Werner, C. H. Back, C Felser, and S. S. P. Parkin, *Appl. Phys. Lett.* **115**, 062403 (2019).

Received Apr. 20, 2021; Revised May 7, 2021; Accepted May 13, 2021

J. Magn. Soc. Jpn., **45**, 79-85 (2021)

<Paper>

Adjacent Track Interference in Three-Dimensional Heat-Assisted Magnetic Recording

T. Kobayashi, Y. Nakatani*, and Y. Fujiwara

Graduate School of Engineering, Mie Univ., *1577 Kurimamachiya-cho, Tsu 514-8507, Japan*

*Graduate School of Informatics and Engineering, Univ. of Electro-Communications, *1-5-1 Chofugaoka, Chofu 182-8585, Japan*

We examine the adjacent track interference (ATI) problem that arises during three-dimensional heat-assisted magnetic recording (3D HAMR) at 2 Tbpsi per layer (total density of 4 Tbpsi) where the medium consists of a high Curie temperature (HC) layer and a low Curie temperature (LC) layer. To evaluate the grain error distribution, the expected magnetization value is calculated using the grain error probability. Prior to considering the ATI in 3D HAMR, we examine the ATI problem for conventional HAMR. Since the temperature of the LC layer in the adjacent tracks while writing in the HC layer (HC writing) exceeds the LC Curie temperature, HC writing will erase the data of the LC layer in the adjacent tracks. Therefore, we investigate 3D HAMR combined with shingled magnetic recording. The ATI in an LC (upper, namely, surface) / HC (lower) layer structure is compared with that in an HC / LC layer structure. The latter is disadvantageous in relation to ATI caused by the small thermal gradient in the LC layer.

Key words: HAMR, 3D HAMR, ATI, information stability, error distribution

1. Introduction

Heat-assisted magnetic recording (HAMR) is a candidate as a next-generation magnetic recording method for achieving a high recording capacity. HAMR is a recording technique where the medium is heated to reduce coercivity during the writing period. Three-dimensional HAMR (3D HAMR) has been proposed[1] where the medium consists of a high mean Curie temperature T_{HC} (HC) layer and a low mean Curie temperature T_{LC} (LC) layer with an isolation layer inserted between the two layers to suppress exchange coupling between them. With 3D HAMR, once data have been written in the HC layer, other data can be written in the LC layer by employing lower temperature heating. Yamane *et al.* reported dual structure, namely 3D, HAMR on bit patterned media[2].

On granular media, we have previously discussed the information stability in the LC and HC layers for 10 years of archiving[3], the stability of the information in the HC layer while writing is under way in the LC layer[3], 3D HAMR media design[4], and the comparison of two layer structures of an LC (upper, namely, surface) / HC (lower) layer and an HC / LC layer[5]. In the LC / HC layer structure, the LC layer has a T_{LC} of 650 K and a layer thickness h_{LC} of 4.5 nm, and the HC layer has a T_{HC} of 750 K and an h_{HC} of 6.0 nm. A T_{HC} of 725 K may be applicable with the aim of improving the heat resistance of the writing head and/or the surface lubricant by reducing their temperatures[5]. On the other hand, the HC layer has a T_{HC} of 750 K and an h_{HC} of 3.5 nm, and the LC layer has a T_{LC} of 550 K and an h_{LC} of 7.0 nm in the HC / LC layer structure. The results show that each of the two layer structures has benefits and drawbacks. On the basis of our examination, we believe the LC / HC layer structure to be preferable.

In this paper, we discuss the information stability in adjacent tracks during the writing period, namely, adjacent track interference (ATI). To evaluate the grain error distribution, the expected value of the magnetization is calculated using the grain error probability. First, we examine the ATI problem for conventional HAMR, and then we concentrate on ATI for 3D HAMR combined with shingled magnetic recording in the LC / HC and HC / LC layer structures.

Corresponding author: T. Kobayashi (e-mail: kobayasi @phen.mie-u.ac.jp).

2. Calculation Method and Conditions

2.1 Grain arrangement and writing conditions

We assumed the medium to be granular and the recording density to be 2 Tbpsi per layer (total density of 4 Tbpsi). The bit pitch D_B and track width D_T are both 18 nm as shown in Fig. 1, and therefore the bit aspect ratio D_T/D_B is one. One bit has m = 3 grains (i = 1, 2, m) in the cross-track (row) direction and n = 3 grains in the down-track (column) direction, and thus there are $m \times n$ = 9 grains/bit.

We examine ATI, namely, the information stability in the N-th track while writing in the $(N+1)$-th track. The Curie temperature T_c distribution was assumed to be normal with a mean Curie temperature T_{cm} and a standard deviation σ_{Tc}/T_{cm} of 2 %. The writing temperature of the grains at the track edges was assumed to be $T_{cm} + 2\sigma_{Tc}$, taking account of the T_c distribution. While writing in the $(N+1)$-th track, the probabilities are 93.3 and 99.8 % where the T_c values of all 3 grains and 2 grains or more are lower than $T_{cm} + 2\sigma_{Tc}$, respectively, at the track edge. Furthermore, the probability is more than 99.9 % where the T_c value of all 3 grains is lower than the temperature at the track center. Therefore, almost all grains are heated above their T_c values during the writing period. If we use a

writing temperature of $T_{cm} + \sigma_{Tc}$ instead of $T_{cm} + 2\sigma_{Tc}$, the probability is only 59.6 % where the T_c value of all 3 grains is lower than $T_{cm} + \sigma_{Tc}$ at the track edge, and then we can assume that there will be a write-error increase. Although the condition of $T_{cm} + \sigma_{Tc}$ is useful for reducing the medium surface temperature, which relates to the heat resistance of the writing head and/or the surface lubricant, the condition $T_{cm} + 2\sigma_{Tc}$ may be required.

Figure 2 shows schematic illustrations of the (a) LC / HC and (b) HC / LC layer structures published in a previous paper[5]. The Curie temperatures (T_{LC} and T_{HC}) and layer thicknesses (h_{LC} and h_{HC}) were determined taking account of the information stability in the LC and HC layers for 10 years of archiving and the stability of the information in the HC layer while writing in the LC layer (LC writing) under conditions where T_{HC} = 750 K and $h_{HC} + h_{LC}$ = 10.5 nm[5]. The readout temperature was assumed to be 330 K.

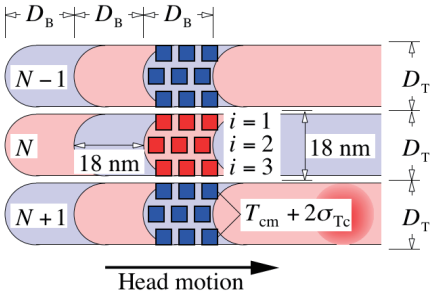

Fig. 1 Grain arrangement and writing conditions.

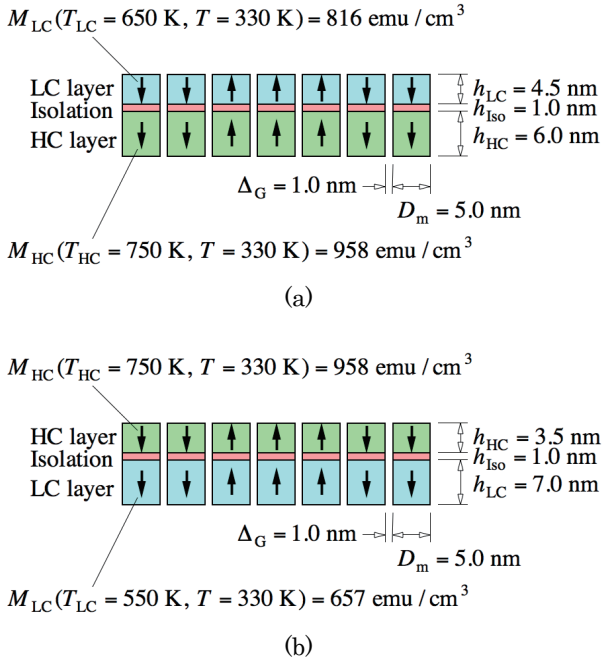

Fig. 2 Layer structures for (a) LC / HC and (b) HC / LC[5].

We assumed that the grain size D distribution was log-normal with a mean grain size D_m of 5.0 nm and a standard deviation σ_D/D_m of 15 %. The intergrain spacing Δ_G was 1.0 nm. The isolation layer is used to suppress exchange coupling between the upper and lower layers. The layer thickness h_{Iso} must be smaller in order to obtain a high field strength from the lower layer at the reader. We chose an h_{Iso} value of 1.0 nm. This problem is a future subject.

2.2 Magnetic properties

The temperature dependence of the magnetization M_s was calculated by employing a mean field analysis[6], and that of the anisotropy constant K_u was assumed to be proportional to $M_s^{2.7}$[7]. $M_s(T_c, T)$ is a function of T_c and temperature T. And $M_s(T_c = 770\ \mathrm{K}, T = 300\ \mathrm{K})$ = 1000 emu/cm^3 was assumed for FePt. With this assumption, the M_s value can be calculated for all T_c and T values.

We introduced an HAMR design parameter, namely, the medium anisotropy constant ratio K_u/K_{bulk}[8], which is the intrinsic ratio of the medium K_u to bulk FePt K_u regardless of T_c. Although a low T_c medium is easy to write when employing HAMR, a high K_u/K_{bulk} is needed for a low T_c medium for 10 years of archiving[9], and a medium with a high K_u/K_{bulk} is difficult to manufacture regardless of T_c [10]. Moreover, a high K_u/K_{bulk} must be achieved in 3D HAMR[3]. $K_u(T_c, K_u/K_{bulk}, T)$ is a function of T_c, K_u/K_{bulk}, and T. And $K_u(T_c = 770\ \mathrm{K}, K_u/K_{bulk} = 1, T = 300\ \mathrm{K})$ = 70 Merg/cm^3 was assumed for bulk FePt. We used a K_u/K_{bulk} value of 0.8 in this paper. With this assumption, the K_u value can be calculated for all T_c and T values. No intrinsic distribution of K_u was assumed. However, there was a fluctuation in K_u caused by σ_{Tc}.

The T_c value can be adjusted by adjusting the Cu composition z for $(Fe_{0.5}Pt_{0.5})_{1-z}Cu_z$.

2.3 Temperature profile

We used data published in a previous paper[5], in which a heat transfer simulation was carried out using Poynting for Optics software (Fujitsu Ltd.), for the temperature profiles of the LC and HC layers during the writing period. The light spot diameter was about 9.0 nm (FWHM) in the down-track and cross-track directions. The linear velocity was 10 m/s. The ambient temperature T_{amb} is the maximum working temperature of the hard disk drive, and was assumed to be 330 K.

We focused on the thermal gradient $\partial T/\partial y$ in the cross-track directions at the track edges during LC and HC writing, the medium surface temperature T_{surf} at the track center during HC writing, and the grain temperature difference ΔT_{HL} between the HC and LC layers at the track edges during LC writing. The $\partial T/\partial y$ value is important for ATI.

We have previously reported the thermal gradient in 3D HAMR[4]:

(1) The thermal gradient for the upper layer is intrinsically larger than that for the lower layer due to a heat flow in the in-plane direction in the deep part of the layer.

(2) The thermal gradient $\partial T_H/\partial y$ for the HC layer is intrinsically larger than $\partial T_L/\partial y$ for the LC layer due to their respective Curie temperatures as given by

$$\frac{\partial T_H}{\partial y} = \frac{T_{HC}+2\sigma_{THC}-T_{amb}}{T_{LC}+2\sigma_{TLC}-T_{amb}} \cdot \frac{\partial T_L}{\partial y}. \quad (1)$$

The result calculated with a heat transfer simulation was used as the temperature profile for the cross-track direction during the writing period in **3.2**, **3.3**, and **3.4**.

2.4 Information stability

The information stability for ATI was estimated using the grain error probability P[3],

$$P = 1 - \exp\left(-f_0 t \exp\left(-\frac{K_{ueff}V}{kT}\left(1+\frac{H_w}{H_{keff}}\right)^2\right)\right), \quad (2)$$
$$(|H_w| < H_{keff})$$

taking account of the shape anisotropy $M_sH_d/2$ using a self-demagnetizing field H_d[4] where $K_{ueff} = K_u - M_sH_d/2$, $V = D \times D \times h$, k, and $H_{keff} = 2K_{ueff}/M_s$ are the effective anisotropy constant, the grain volume, the Boltzmann constant, and the effective anisotropy field, respectively. The writing field H_w and time t were assumed to be -10 kOe and 1 ns, respectively. The attempt frequency f_0 is a function of the damping constant α, and we used an α value of 0.1. The calculation bit number was 1E+7.

To evaluate the grain error distribution, we calculated the expected value of the magnetization $E[M_s]$,

$$E[M_s] = (1-P)M_s + P(-M_s) = (1-2P)M_s. \quad (3)$$

The $E[M_s]$ value was averaged over one row of grains (n = 3) as

$$E[M_{si}] = \frac{\sum_{j=1}^{n}(1-2P_{ij})M_{sij}(T_{cij},\ 330\ \mathrm{K})}{n} \quad (4)$$

for the information stability in the N-th track while writing in the $(N+1)$-th track since there is a temperature distribution in the cross-track direction.

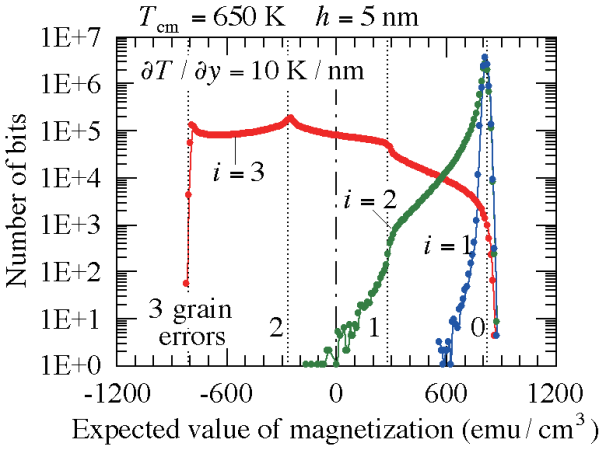

Fig. 3 Number of bits against expected value of magnetization $E[M_{si}]$ in the N-th track while writing in the $(N+1)$-th track.

3. Calculation Results

3.1 ATI for conventional HAMR

In 3D HAMR, T_{cm}, h, and $\partial T/\partial y$ change in a complex manner for each layer. Therefore, first, we examined the ATI problem for conventional HAMR by changing only one calculation parameter. The magnetic properties were calculated by the method described in **2.2**.

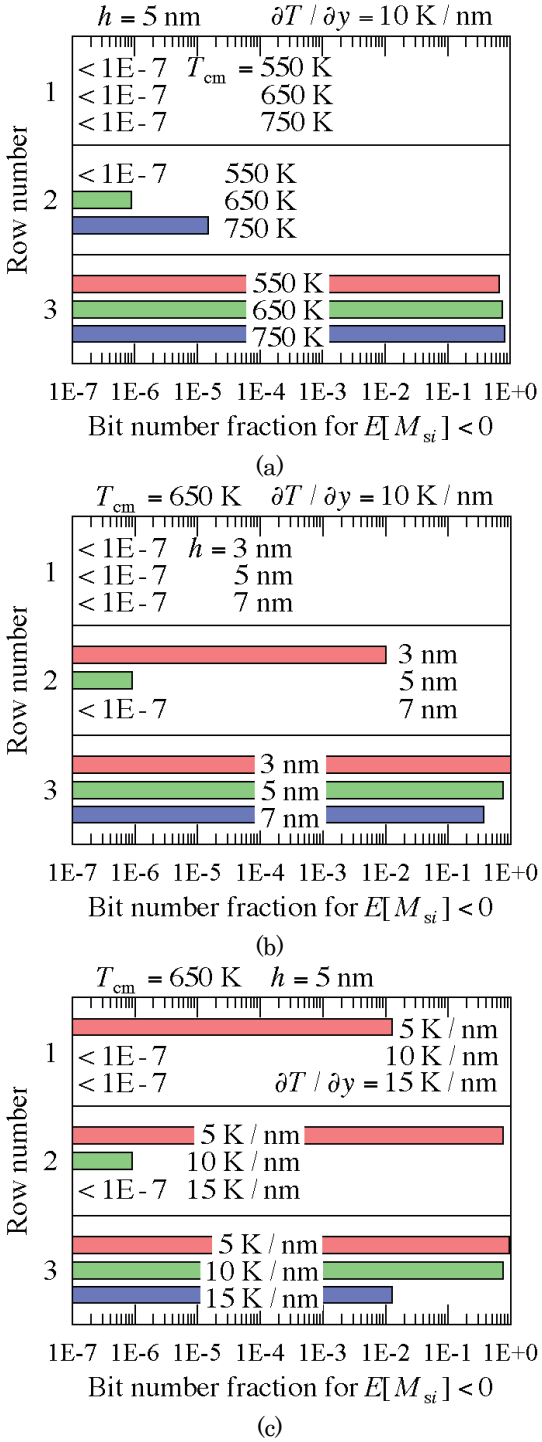

Fig. 4 Bit number fraction for $E[M_{si}] < 0$ in the N-th track while writing in the $(N+1)$-th track for various (a) T_{cm}, (b) h, and (c) $\partial T/\partial y$ values.

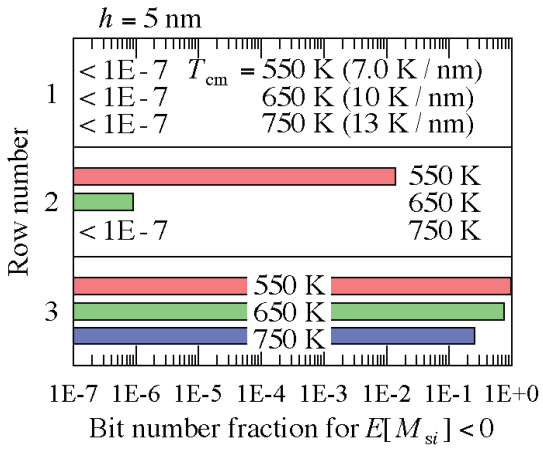

Fig. 5 Bit number fraction for $E[M_{si}] < 0$ in the N-th track while writing in the $(N+1)$-th track for T_{cm} = 550 K ($\partial T/\partial y$ = 7.0 K/nm), 650 K (10 K/nm), and 750 K (13 K/nm).

The bit error rate is a function of various parameters, *e.g.* the magnetization direction, the grain size, and the readout track width. Since the bit error rate depends on the readout track width, the bit error rate was not examined in this paper. We focused on the magnetization direction using $E[M_{si}]$ to evaluate the grain error distribution for the cross-track direction. The bit error rate will increase qualitatively as the bit number for the negative $E[M_{si}]$ increases since the negative $E[M_{si}]$ means that the magnetization direction is opposite to the recorded direction. The number of bits against $E[M_{si}]$ in the N-th track while writing in the $(N+1)$-th track, namely, the grain error distribution, is shown in Fig. 3 for T_{cm} = 650 K, h = 5 nm, and $\partial T/\partial y$ = 10 K/nm which was assumed to be constant everywhere. The peaks in the figure represent grain error for the grain with the mean Curie temperature, and the $E[M_{si}]$ value is negative for 2 or 3 grain errors since the total row grain number is three. For all grains, the negative $E[M_{si}]$ represents more than half of 3 grain errors. The grain error increases in the order of i = 1, 2, and 3 since the temperature increases in this order. Some information degradation can be seen even in the 2nd row (i = 2) grains. Since there is a large degradation of the information in the 3rd row (i = 3) grains, at least the 3rd row grains must be used as a guard band for ATI.

Figure 4 shows the bit number fraction for $E[M_{si}] < 0$, namely, the ratio of the bit number for $E[M_{si}] < 0$ in Fig. 3 to all the bits, for various (a) T_{cm}, (b) h, and (c) $\partial T/\partial y$ values. The fraction increases slightly and ATI worsens as T_{cm} increases, as shown in Fig. 4 (a). Although K_{ueff} increases as T_{cm} increases, T also increases as T_{cm} increases. Therefore, the $K_{ueff}V/(kT)$ value in Eq. (2) decreases as T_{cm} increases. When h is thin, ATI worsens as shown in Fig. 4 (b) since the $K_{ueff}V/(kT)$ value simply becomes smaller. When $\partial T/\partial y$ is small, ATI becomes worse not only in the 2nd row (i = 2) grains but in the 1st row (i = 1) grains as shown in Fig. 4 (c) since K_{ueff} is small and T is high.

The T_{cm} and the $\partial T/\partial y$ values are closely related by Eq. (1). Therefore, ATI was calculated by changing the $\partial T/\partial y$ and T_{cm} values at the same time according to Eq. (1) under the condition $\partial T/\partial y$ = 10 K/nm when T_{cm} = 650 K. As a result, ATI becomes worse as T_{cm} decreases, as shown in Fig. 5.

3.2 ATI for 3D HAMR

Next, we examined the ATI problem for 3D HAMR. Figure 6 shows the temperature profiles of the LC and HC layers in the cross-track direction during HC writing. The solid lines indicate the temperatures at the layer boundaries, and the dotted lines indicate those at the layer centers.

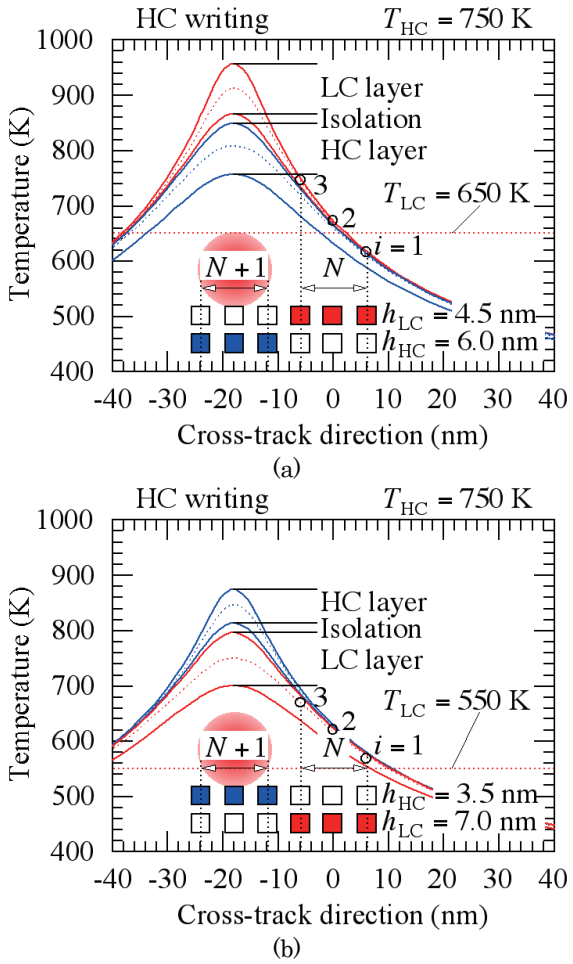

Fig. 6 Temperature profile in cross-track direction for (a) LC / HC and (b) HC / LC layer structures during HC writing.

The writing temperature of the HC layer in the $(N+1)$-th track at −12 and −24 nm is $T_{HC} + 2\sigma_{THC}$ = 780 K. For the LC / HC layer structure shown in Fig. 6 (a), the temperatures of the LC layer in the N-th track at 6 (i = 1), 0 (i = 2), and −6 nm (i = 3) are 616, 671, and 745 K, respectively. The temperatures at 0 (i = 2) and −6 nm (i = 3) are higher than the T_{LC} of 650 K. On the other hand, for the HC / LC layer structure shown in Fig. 6 (b), although the LC layer in the N-th track at 6 (i = 1), 0 (i

= 2), and −6 nm (i = 3) has low temperatures of 573, 617, and 669 K, respectively, since LC is the lower layer, all temperatures are higher than T_{LC} of 550 K since the T_{LC} value must be reduced to realize information stability in the HC layer during LC writing[5].

Since the temperature of the LC layer in the adjacent tracks during HC writing exceeds the LC Curie temperature, HC writing will erase the data of the LC layer in the adjacent tracks. Therefore, it is necessary to devise a suitable writing method to address this issue, *e.g.* combination with shingled magnetic recording. The following deals with shingled 3D HAMR.

3.3 ATI for LC / HC layer structure

In this section, we discuss the information stability in the N-th track of the LC and HC layers while writing in the $(N+1)$-th track of the LC and HC layers (LC and HC ATI), respectively, for the LC / HC layer structure.

We have carried out a heat transfer simulation for 3D HAMR media as reported in a previous paper[5]. The results are summarized in Table 1. The difference between the $\partial T/\partial y$ values for LC and HC writing is relatively small due to the combinations of the upper LC layer and the lower HC layer. The T_{surf} value of 957 K is relatively high since HC is the lower layer. This is disadvantageous in terms of the heat resistance of the writing head and/or the surface lubricant. The ΔT_{HL} value of − 42 K is negative, which means that the temperature in the HC layer during LC writing is lower than that in the LC layer, and this is advantageous in relation to the information stability in the HC layer.

Table 1 Results of heat transfer simulation for LC / HC layer structure[5].

	LC writing	HC writing
LC / HC layer structure		
T_{cm} (K)	650	750
h (nm)	4.5	6.0
$\partial T / \partial y$ (K / nm)	12.0	9.0
T_{surf} (K)		957
ΔT_{HL} (K)	–42	

The grain error distribution is shown in Fig. 7 as regards (a) LC and (b) HC ATI. Although the LC layer is thinner than the HC layer, the thermal gradient of the LC layer is larger than that of the HC layer (see Fig. 4). Then the error distributions are roughly the same for (a) LC and (b) HC ATI since the vertical axis is the logarithmic scale. Although some information degradation can be seen in the 2nd row (i = 2) grains, the bit number for $E[M_{si}] < 0$ is small.

Figure 8 shows the bit number fraction for $E[M_{si}] < 0$. The fractions are less than 1E-7 in both the LC and HC layers for i = 1, and are only 4E-5 and 3E-7 in the LC and HC layers, respectively, for i = 2. However, the fractions are as high as 7E-1 and 6E-1 in the LC and HC layers, respectively, for i = 3. The magnetization reversal for more than half of the grains can be seen for i = 3.

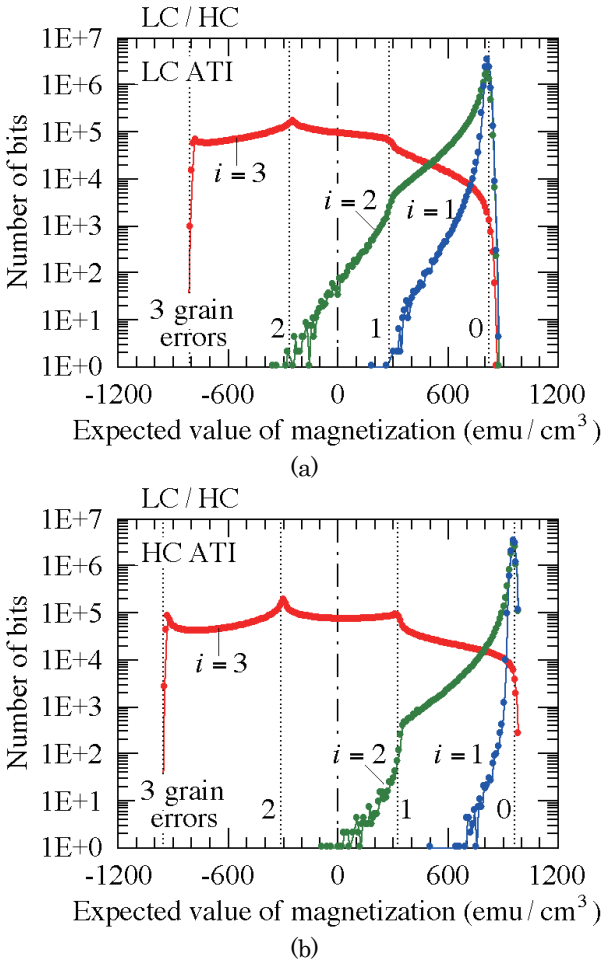

Fig. 7 Number of bits against expected value of magnetization $E[M_{si}]$ in (a) the N-th track of the LC layer while writing in the $(N+1)$-th track of the LC layer (LC ATI) and (b) HC ATI for LC / HC layer structure.

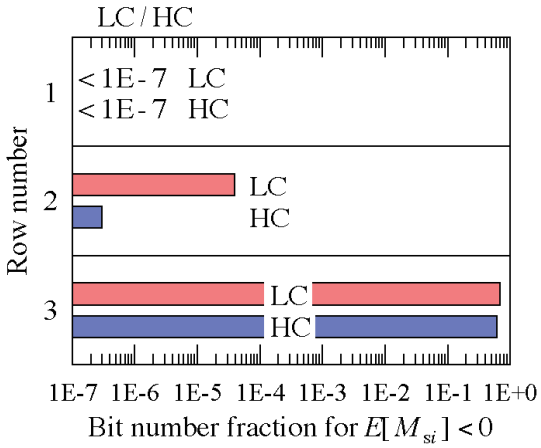

Fig. 8 Bit number fraction for $E[M_{si}] < 0$ in LC and HC ATI for LC / HC layer structure.

Using the above result, we illustrate ATI for shingled 3D HAMR schematically in Fig. 9, in which the gray regions indicate the magnetization transition. The 3rd row (i = 3) grains used as a guard band, and the readout track width effectively decreases to about 12 nm from 18 nm as shown in Fig. 1.

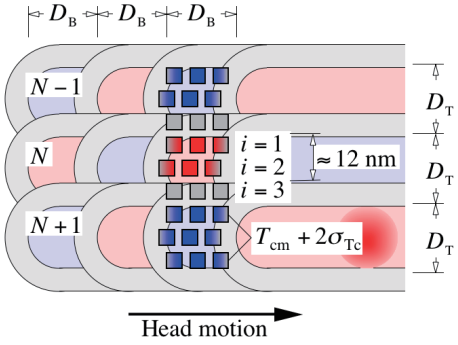

Fig. 9 Schematic illustration of ATI for LC / HC layer structure.

3.4 ATI for HC / LC layer structure

Next, we discuss ATI for the HC / LC layer structure.

The results of a heat transfer simulation reported in a previous paper[5] are summarized in Table 2. The T_{surf} value of 874 K compared with the value of 957 K in Table 1 is relatively low since HC is the upper layer. This is advantageous in terms of heat resistance. The positive ΔT_{HL} value of 35 K compared with −42 K in Table 1 is disadvantageous in relation to the information stability in the HC layer during LC writing. Therefore, the T_{LC} value must be lower than that in Table 1. As a result, compared with the results in Table 1, the difference between the $\partial T/\partial y$ values for HC and LC writing is relatively large due to the lower T_{LC} value in addition to the combinations of the upper HC layer and the lower LC layer.

Table 2 Results of heat transfer simulation for HC / LC layer structure[5].

	HC writing	LC writing
HC / LC layer structure		
T_{cm} (K)	750	550
h (nm)	3.5	7.0
$\partial T / \partial y$ (K / nm)	16.4	5.0
T_{surf} (K)	874	
ΔT_{HL} (K)		35

The grain error distribution is shown in Fig. 10 as regards (a) HC and (b) LC ATI. Compared with the result in Table 1, although the HC layer in Table 2 is thinner, the HC thermal gradient is larger (see Fig. 4). Then the error distributions are roughly the same in Fig. 7 (b) and Fig. 10 (a). In contrast, large information degradation can be seen even in the 2nd row (i = 2) grains for the LC layer as shown in Fig. 10 (b) since the LC thermal gradient is small (see Fig. 4) as shown in Table 2.

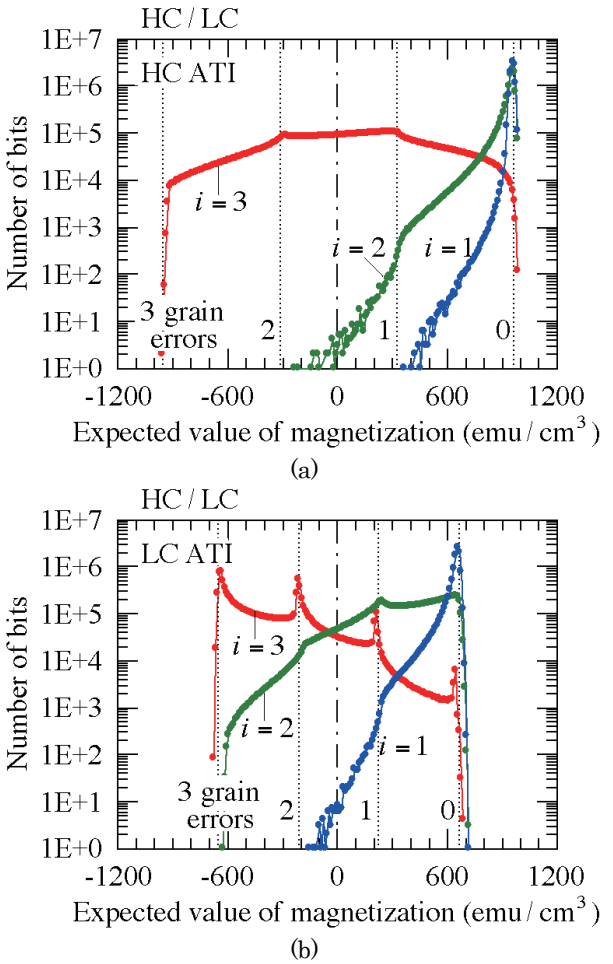

Fig. 10 Number of bits against expected value of magnetization $E[M_{si}]$ as regards (a) HC and (b) LC ATI for HC / LC layer structure.

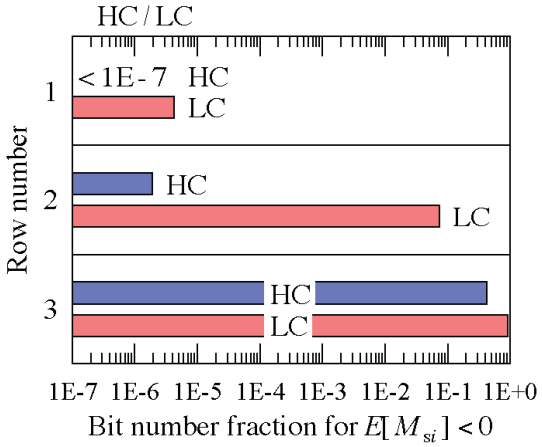

Fig. 11 Bit number fraction for $E[M_{si}] < 0$ in HC and LC ATI for HC / LC layer structure.

The above results are reflected in the results in Fig. 11 which shows the bit number fraction for $E[M_{si}] < 0$. The fraction in the LC layer reaches 7E-2 for $i = 2$ and 9E-1 for $i = 3$. Therefore, both the 3rd row ($i = 3$) and 2nd row ($i = 2$) grains are used as a guard band in the LC layer, and the readout track width will be narrow as shown in Fig. 12.

In conclusion, the LC / HC layer structure is preferable as regards ATI.

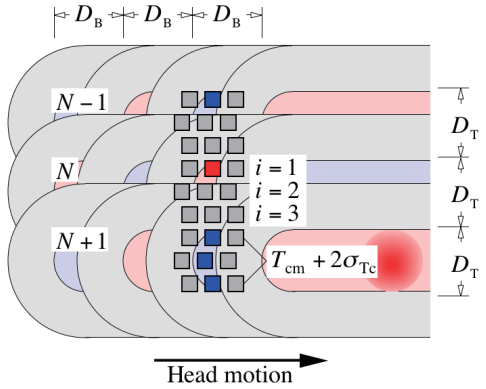

Fig. 12 Schematic illustration of LC ATI for HC / LC layer structure.

4. Conclusions

We examined the adjacent track interference (ATI) problem in conventional HAMR and 3D HAMR combined with shingled magnetic recording in LC (upper, namely, surface) / HC (lower) and HC / LC layer structures.

(1) Conventional HAMR

When the medium is thin, ATI worsens since the grain volume simply becomes smaller.

Curie temperature and thermal gradient are closely related. Therefore, ATI worsens as the Curie temperature decreases since the thermal gradient decreases at the same time.

(2) Shingled 3D HAMR

The thermal gradient in the LC layer is small for the HC / LC layer structure since LC is the lower layer, and the LC Curie temperature is lower than that in the LC / HC layer structure. Therefore, ATI in the LC layer is worse for the HC / LC layer structure.

The LC / HC layer structure is preferable as regards ATI.

Acknowledgement We acknowledge the support of the Advanced Storage Research Consortium (ASRC), Japan.

References

1) Western Digital: private communication.
2) H. Yamane, S. J. Greaves, and Y. Tanaka: *IEEE Trans. Magn.*, **57**, 3200706-1-6 (2021).
3) T. Kobayashi, Y. Nakatani, and Y. Fujiwara: *J. Magn. Soc. Jpn.*, **44**, 34 (2020).
4) T. Kobayashi, Y. Nakatani, and Y. Fujiwara: *J. Magn. Soc. Jpn.*, **44**, 122 (2020).
5) T. Kobayashi, Y. Nakatani, and Y. Fujiwara: *J. Magn. Soc. Jpn.*, **45**, 16 (2021).
6) M. Mansuripur and M. F. Ruane: *IEEE Trans. Magn.*, **MAG-22**, 33 (1986).
7) J. -U. Thiele, K. R. Coffey, M. F. Toney, J. A. Hedstrom, and A. J. Kellock: *J. Appl. Phys.*, **91**, 6595 (2002).
8) T. Kobayashi, Y. Isowaki, and Y. Fujiwara: *J. Magn. Soc. Jpn.*, **39**, 8 (2015).
9) T. Kobayashi, Y. Nakatani, and Y. Fujiwara: *J. Magn. Soc. Jpn.*, **43**, 114 (2019).
10) T. Kobayashi, Y. Nakatani, and Y. Fujiwara: *J. Magn. Soc. Jpn.*, **42**, 110 (2018).

Received Mar. 13, 2021; Accepted Apr. 20, 2021

J. Magn. Soc. Jpn., **45**, 86-95 (2021)

<Paper>

Void-Defect Induced Magnetism and Structure Change of Carbon Material-Ⅲ: Hydrocarbon Molecules

Norio Ota[1], Aigen Li[2], and Laszlo Nemes[3]

[1]Graduate school of Pure and Applied Sciences, University of Tsukuba, *1-1-1 Tennodai, Tsukuba-City Ibaraki 305-8571, Japan*
[2]Department of Physics and Astronomy, University of Missouri, *Columbia, MO 65211, USA*
[3]Research Center for Natural Sciences, Ötvös Lóránd Research Network, *Budapest 1519, Hungary*

Void-defect induced magnetism of graphene molecule was recently reported in our previous paper of this series study. This paper investigated the case of hydrogenated graphene molecule, in chemical term, polycyclic aromatic hydrocarbon (PAH). Molecular infrared spectrum obtained by density functional theory was compared with astronomical observation. Void-defect on PAH caused serious structure change. Typical example of $C_{23}H_{12}$ had two carbon pentagon rings among hexagon networks. Stable spin state was non-magnetic singlet state. This is contrary to pure carbon case of C_{23}, which show magnetic triplet state. It was discussed that Hydrogen played an important role to diminish magnetism by creating an SP3-bond among SP2-networks. Such a structure change affected molecular vibration and finally to photoemission spectrum in infrared region. The dication-$C_{23}H_{12}$ showed featured bands at 3.2, 6.3, 7.7, 8.6, 11.2, and 12.7 micrometer. It was surprising that those calculated bands coincided well with astronomically observed bands in many planetary nebulae. To confirm our study, large size molecule of $C_{53}H_{18}$ was studied. Calculation reproduced again similar astronomical bands. Also, small size molecule of $C_{12}H_8$ showed good coincidence with the spectrum observed for young stars. This paper would be the first report to indicate the specific PAH in space.

Key words: PAH, void, spin state, DFT, planetary nebula, infrared spectrum

1. Introduction

Graphene and graphite like carbon materials are candidates for showing carbon based ferromagnetism[1)-6)]. There are many capable explanations based on impurities[7)], edge irregularities[8)-10)] or defects[11)-16)]. However, origin of magnetic ordering could not be thoroughly understood. We previously reported in the same series paper[17)] that void defect in graphene nano ribbon (GNR) induces highly spin polarized magnetism investigated by density functional theory (DFT). Calculated result showed good coincidence with experiments[18)-20)]. Also, in our recent series paper[21)] we applied to graphene molecule. Void induced molecule was deformed to a featured structure having one carbon pentagon ring among hexagon networks. It was a surprise that most of graphene molecules show magnetism with the stable spin state of triplet, not singlet. Unfortunately, on laboratory experiment, such small pure carbon molecule did not show any magnetic feature. The reason may be molecule-to-molecule interaction at high molecular density conditions on earth of 10^{10}~10^{23} molecules/cm^3, which may bring paramagnetic canceling. We tried to look at astronomical carbon dust floating in interstellar and circumstellar space under ultra-low-density condition of 1~100 molecules/cm^3. It is almost isolate molecule. While DFT calculation gives solution on isolate molecule. It was a surprise that calculated infrared spectrum showed good coincide with astronomically observed infrared spectrum, especially spectra of carbon rich planetary nebulae[22)23)].

In this paper, we like to try the case of hydrogenated graphene molecule, which is named polycyclic aromatic hydrocarbon (PAH) in chemistry. It is well known that PAH does not show any magnetic feature, which is typical diamagnetic material. Our question is that such non-magnetic property is common even for a case of void-defect induced PAH. Here again, we like to compare DFT calculated infrared spectrum with astronomically observed one. Molecular structure affects to molecular vibration, finally to infrared spectrum. The interstellar gas and dust show featured mid-infrared emission at 3.3, 6.2, 7.6, 7.8, 8.6, 11.2, and 12.7 μm, which are ubiquitous peaks observed at many astronomical objects[22)-29)]. Current common understanding is that these astronomical spectra come from the vibrational modes of PAH. There are many laboratory spectroscopy data[30)-33)] and DFT analysis[34)-39)]. However, despite long-term efforts, until now there is not any identified specific PAH. In this study, we will indicate unexpected coincidence of calculated emission spectrum of specific void induced PAH with above

Corresponding author: Norio Ota (n-otajitaku@nifty.com).

ubiquitously observed spectrum. In addition, to confirm our finding, larger size molecule and smaller one will be compared.

2. Model Molecules and Calculation Method

2.1 Model molecules

Model molecules are illustrated in Fig. 1. Starting mother molecule is typical PAH of coronene-($C_{24}H_{12}$) having seven carbon hexagon rings. In this paper, we apply one assumption of single void-defect on initial molecule. On laboratory experiment, void will be created by an attack of high-speed particle as like proton or Argon. In interstellar and circumstellar space, high speed cosmic ray, mainly proton and electron, may attack on PAH. As illustrated on top of Fig. 1, high speed particle attacks mother molecule ($C_{24}H_{12}$) and kick out one carbon atom. Deformed molecular structure depends on void position as marked by red letters of c, d, and e. Void induced molecule is also named by suffixing as ($C_{23}H_{12}$-c), ($C_{23}H_{12}$-d) and ($C_{23}H_{12}$-e). DFT calculation resulted that there occurs serious structure change as shown in columns of Fig. 1. In case of ($C_{23}H_{12}$-c), two carbon pentagon rings are created among hexagon-ring network. Side view shows Y-shaped configuration. In case of ($C_{23}H_{12}$-d), one pentagon ring is created, where one extra hydrogen atom bonded with a carbon. Molecular structure is umbrella like curved one. Fragment of (C-H) will be kicked out in case of void-e to induce ($C_{23}H_{11}$-e) having one pentagon ring on a flat molecule. In this study, we suppose isolate molecule, which means no molecule-to-molecule interaction, and no energy competition between species. All species will be realized. To find size dependence, we will add larger molecule of ($C_{54}H_{18}$) in section 6, and smaller one of ($C_{13}H_9$) in section 7.

2.2 Calculation Methods

In calculation, we used DFT[40, 41] with the unrestricted B3LYP functional[42]. We utilized the Gaussian09 software package[43] employing an atomic orbital 6-31G basis set[44]. Unrestricted DFT calculation was done to have the spin dependent atomic structure. The required convergence of the root-mean-square density matrix was 10^{-8}. Based on such optimized molecular configuration, fundamental vibrational modes were calculated, such as C-H and C-C stretching modes, C-H bending modes and so on, using the same Gaussian09 software package. This calculation also gives harmonic vibrational frequency and intensity in infrared region. The standard scaling is applied to the frequencies by employing a scale factor of 0.965 for PAH from the laboratory experimental value on coronene ($C_{24}H_{12}$)[45]. Correction due to anharmonicity was not applied to avoid uncertain fitting parameters. To each spectral line, we assigned a Gaussian profile with a full width at half maximum (FWHM) of 4cm^{-1}.

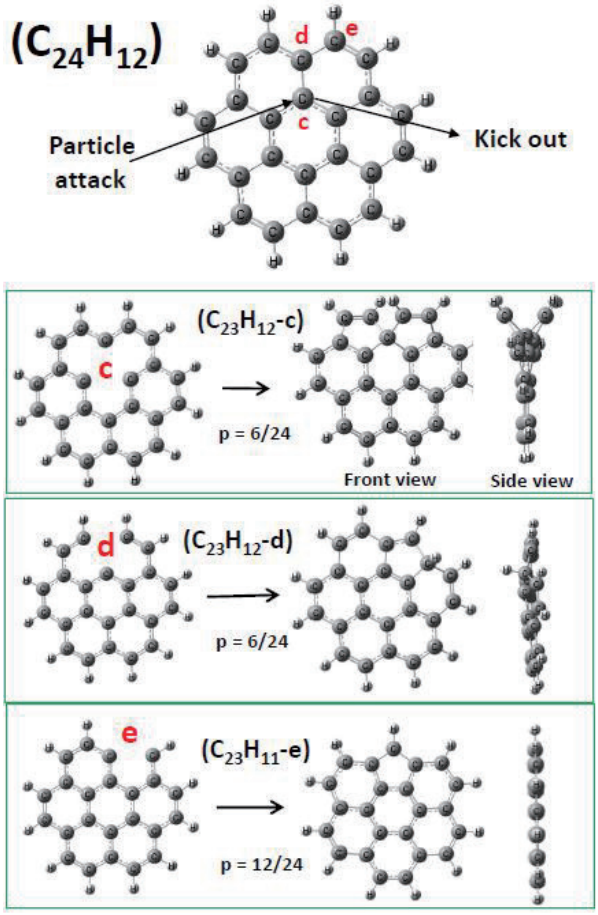

Fig. 1 Void defect on mother molecule ($C_{24}H_{12}$). Deformed structure depends on void position suffixed by c, d, and e.

3. Spin State Analysis

Spin-multiplicity was studied for charge neutral molecules. In this study, we dealt total molecular spin $\boldsymbol{S}$ (vector). Molecule is rotatable material, easily follows to the external magnetic field of z-direction. Projected component to z-direction is maximum value of S_z, which becomes a good quantum parameter. In molecular magnetism, S_z=2/2 is named as triplet spin-state. Example is shown in Fig. 2 for void-c type molecule. As shown in (A), discussed in our previous paper[21], pure carbon molecule of (C_{23}-c) has 3 radical carbons holding 6 spins as initial void. One radical carbon holds two spins, which are forced to be parallel up-up spins (by red arrows in Fig. 2) or down-down spins (blue) for avoiding large coulomb repulsion due to Hund's rule[46]. Capable spin-states are S_z=0/2, 2/2, 4/2 and 6/2. Three couples of spin-pair will be partially cancelled and remain one pair to be triplet. The most stable spin-state was S_z=2/2, which is 0.49 eV lower energy than that of S_z=0/2. Other spin states of S_z=4/2, and 6/2 were rather unstable. DFT calculated spin cloud of S_z=2/2 is mapped on right showing up-spin by

red and down-spin by blue.

Here, important question is that such magnetism is the same or not, even the case of void induced PAH as like ($C_{23}H_{12}$-c). It was interesting that calculated result was contrary to pure carbon case. Resulted spin configuration was illustrated in (B) of Fig. 2. The most stable spin state was S_z=0/2 to be nonmagnetic. Calculated energy of S_z=2/2 was 1.2eV higher (unstable) than that of S_z=0/2. Other void position cases also show that void-defect induced PAH have stable spin-state of S_z=0/2.

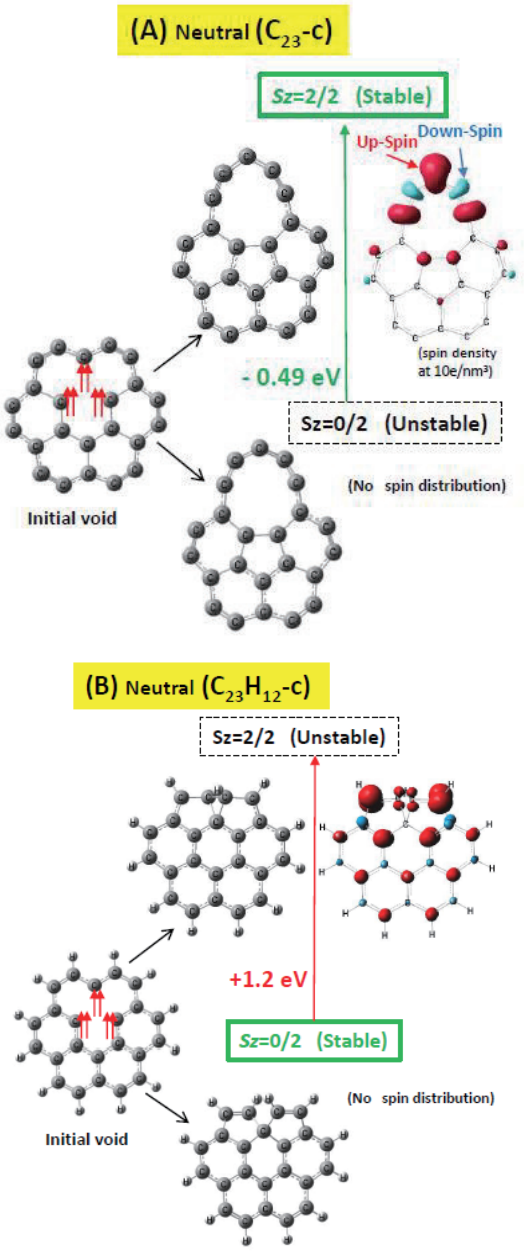

Fig. 2 Stable spin state of void induced pure carbon (C_{23}-c) is triplet as shown in (A), while singlet for hydrocarbon ($C_{23}H_{12}$-c) in (B).

Hydrogen played an important role to diminish magnetism by bringing SP3-bond among SP2-network. Detailed molecular structure of ($C_{23}H_{12}$-c) is shown in Fig. 3. There is one SP3 bond marked by blue circle. Four carbons (1C, 2C, 3C and 4C) are bonded to a center carbon (0C). Six electrons in an initial void are used to make such SP3 bond and to diminish initial paired spins. There remains no spin-pair. Coulomb repulsive force between two hydrogen atoms (+0.14e for 1H and 2H) place them as far as possible, while carbon (0C) has negative charge of -0.26e, which attracts above hydrogen atoms. These forces bring SP3-bond.

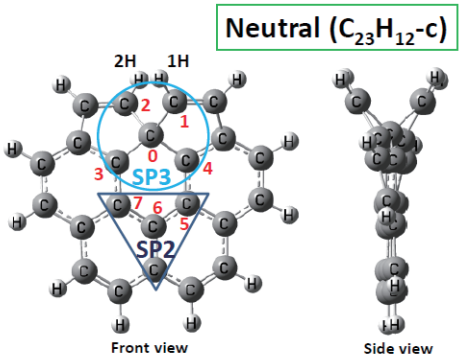

	Distance	(nm)	Angle	(degree)
SP3	1C-0C	0.157	1C-0C-2C	94.7
	2C-0C	0.157	1C-0C-3C	127.1
	3C-0C	0.151	1C-0C-4C	99.4
	4C-0C	0.151		
SP2	4C-5C	0.141	0C-4C-5C	124.3
	6C-5C	0.144	4C-5C-6C	120.6
	7C-6C	0.144	5C-6C-7C	119.2

Atom	Charge
1H	+0.14
2H	+0.14
1C	-0.09
2C	-0.09
0C	-0.26

Fig. 3 Molecular structure of neutral ($C_{23}H_{12}$-c).

4. Ionized Molecule and Infrared Spectrum

It is well known that PAH species having odd number molecular electrons show paramagnetic feature. Typical example is ionized PAH's. In case of ($C_{23}H_{12}$-c), energy diagram for ionization was illustrated on left of Fig. 4. It takes 6.50 eV to extract one electron from neutral molecule, which induce mono-cation $(C_{23}H_{12}\text{-c})^{1+}$. Similarly, di-cation needs additional 10.66 eV. On laboratory, high energy photo-illumination can realize such ionization. In interstellar space, central star can do such illumination on cosmic dust [29]. By photoionization, angle of 1C-0C-2C varies from 94.7 to 95.4 degree. Permanent dipole moment D increases from 0.65 to 1.20 Debye. Such structure change affects molecular vibration and infrared spectrum.

As illustrated on top of Fig. 5, high energy photon kicks out one electron of the highest occupied molecular orbit (HOMO). Remained one electron give rise to mono cation with spin-state of S_z=1/2. Spin distribution was calculated as shown on bottom left, which comes from the difference of total up-spins and

total down-spins. HOMO is a major part of remained spin, of which orbital was illustrated on bottom right, where green cloud is positive sign wave-function and dark red negative one.

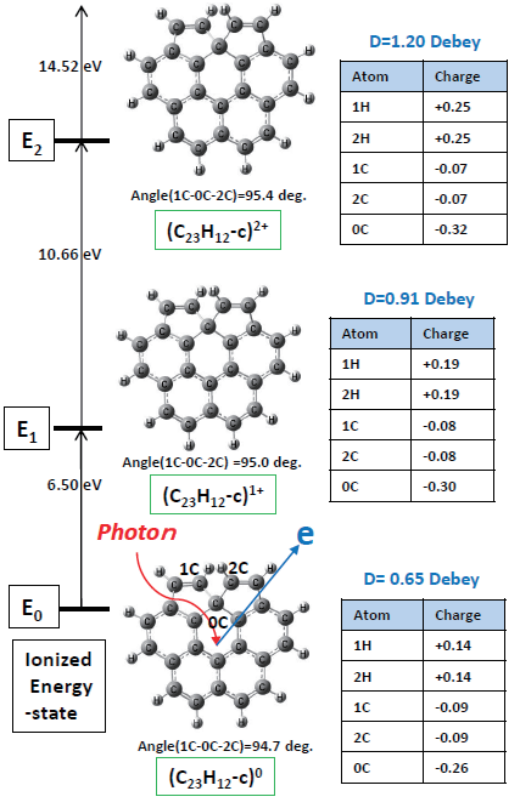

Fig. 4 Energy diagram of ionized ($C_{23}H_{12}$-c).

Calculated infrared spectra are shown in Fig. 6. Molecules are mother molecule ($C_{24}H_{12}$), void induced molecules of ($C_{23}H_{12}$-c), ($C_{23}H_{12}$-d) and ($C_{23}H_{11}$-e). It should be noted that infrared spectrum is sensitive to ionization. Neutral molecule showed single main band, whereas mono-cation three or more major bands, and di-cation more complex one.

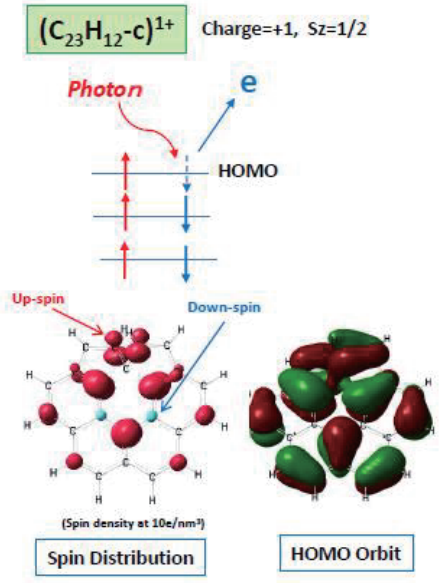

Fig. 5 Spin distribution and HOMO orbit of $(C_{23}H_{12}\text{-c})^{1+}$.

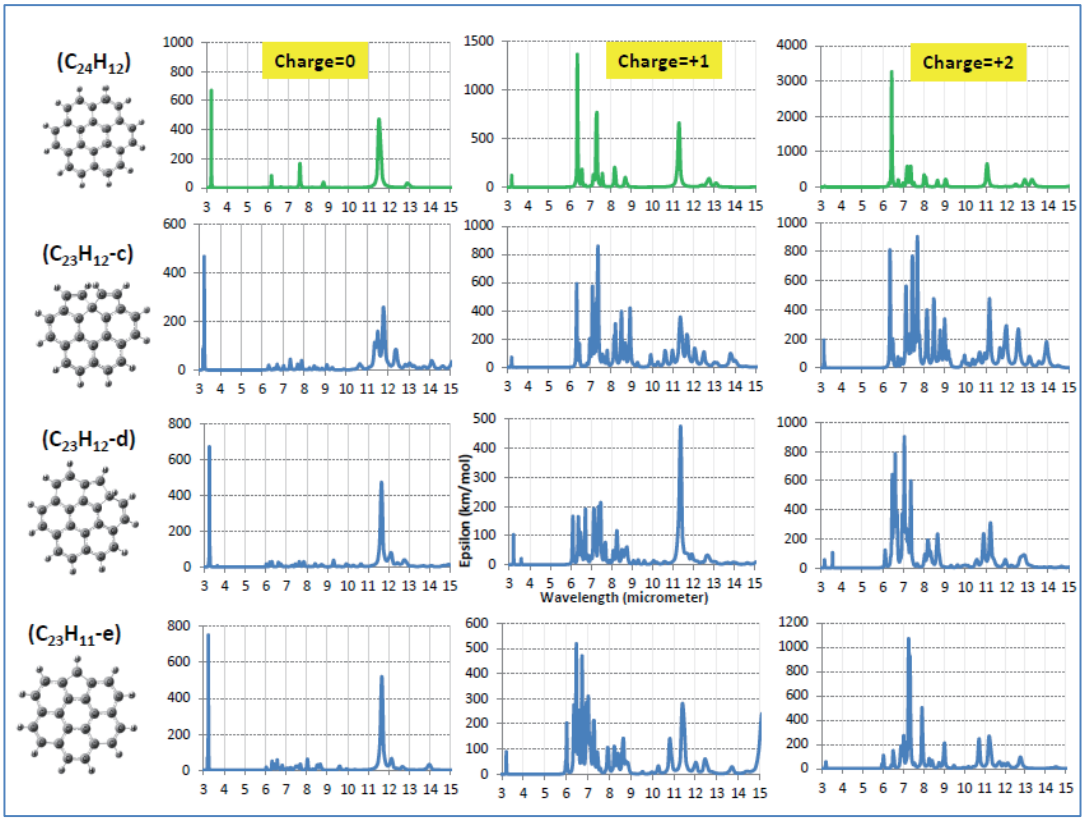

Fig. 6 Calculated infrared spectra of ($C_{24}H_{12}$) family.

5. Comparison with Astronomical Observation

5.1 Infrared spectrum of planetary nebula

Vacuum level on earth is in a range of 10^9-10^{14} molecules/cm^3. While in interstellar and circumstellar space, molecular density will be 1-100 molecules/cm^3. Molecule has almost no interaction with other molecules. Additionally, cosmic dust will be kept under temperature less than 10K. Those conditions are favorable for comparing DFT calculation, because that DFT essentially gives isolate and temperature-zero solution.

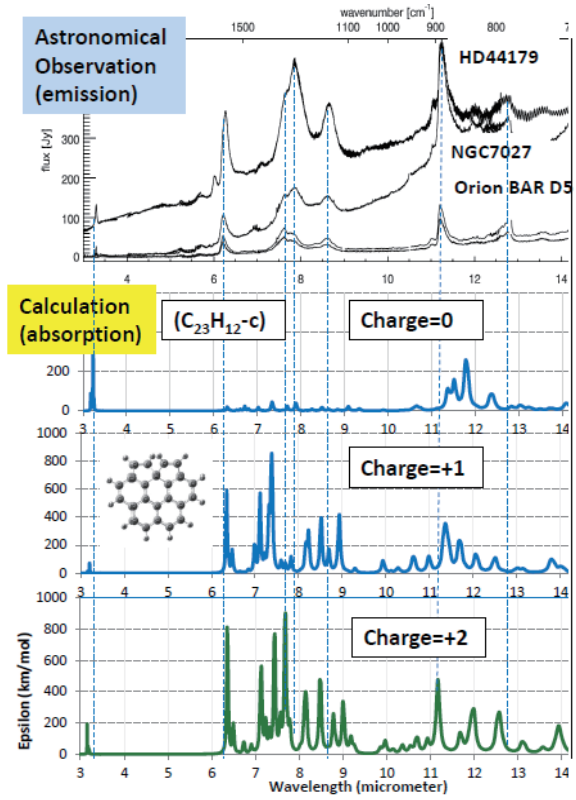

Fig. 7 Calculated infrared spectra compared with astronomically well observed bands. We can see good coincidence with di-cation $(C_{23}H_{12}\text{-}c)^{2+}$.

On top of Fig. 7, astronomical spectra are illustrated for cases of planetary nebulae HD44179, NGC7027, and Orion Bar D5, reported by Boersma et al.[47]. They are few thousand light-years away, very far distance each other. It should be noted that those spectra show common infrared bands at 3.3, 6.2, 7.6, 7.8, 8.6, 11.2, and 12.7 μm. Such observation suggests the common essential mechanism on the creation and evolution of PAH in space. DFT calculated spectra listed in Fig. 6 were compared with such observed spectra. Among them, di-cation $(C_{23}H_{12}\text{-}c)^{2+}$ show major bands at 3.2, 6.3, 7.6, 7.8, 8.6, 11.2, and 12.6 μm. It was amazing that $(C_{23}H_{12}\text{-}c)^{2+}$ could well reproduce observed one as shown on bottom of Fig. 7. This may be first indication to suggest the existence of specific PAH in space. Despite over 30 years many efforts, until now there is not any identified specific PAH. In this study, we like to check whether our finding is an accidental coincidence or reasonable one by trying larger and smaller molecules in later sections.

5.2 Emission spectrum and fundamental mode

It should be noted that the astronomically observed spectra are seen in emission. A central star of nebula may illuminate cosmic molecules and excites them to give rise to infrared emission. Detailed discussion was reported by Li and Drain[48)49)]. Emission calculation on $(C_{23}H_{12}\text{-}c)^{2+}$ was done by Dr. Christiaan Boersma, NASA Ames laboratory, based on our fundamental vibrational mode analysis in private communication in 2014. He tried emission calculation supposing 6eV photoexcitation, scaling factor of 0.958, and FWHM of 15cm^{-1}. Result is shown in Fig. 8 by red on bottom compared with his observed data on NGC7023 nebula on top. Again, it was a surprise that emission calculation shows good coincidence with observation. Also, we regard that, in case of sufficient large photoexcitation, calculated absorption spectrum is a mirror image of emission one due to the theory of Einstein's emission coefficient[48),49)]. In this study, we like to compare astronomical spectrum simply with DFT calculated spectra.

Fundamental mode was analyzed on Table 1. There are 99 modes for 35 atoms. Zero-point vibrational energy is 7.44 eV above total electronic energy. The highest vibrational energy of mode-99 is 3284 cm^{-1} (=0.407 eV) above zero-point vibrational energy. Mode-98 corresponds to observed 3.3 μm band, which comes from C-H stretching at carbon pentagon sites. Similarly, mode-87 by C-C stretching at hexagon sites corresponds to observed 6.2 μm band, also mode-71 by C-H in-plane bending and C-C stretching to 7.6 μm observed band, mode-69 to 7.8 μm observed band. Both mode61 and 62 may contribute to 8.6 μm observed band. Mode-43 was featured by C-H out-of-plane bending at all outer carbon sites, correspond to 11.2 μm observed band.

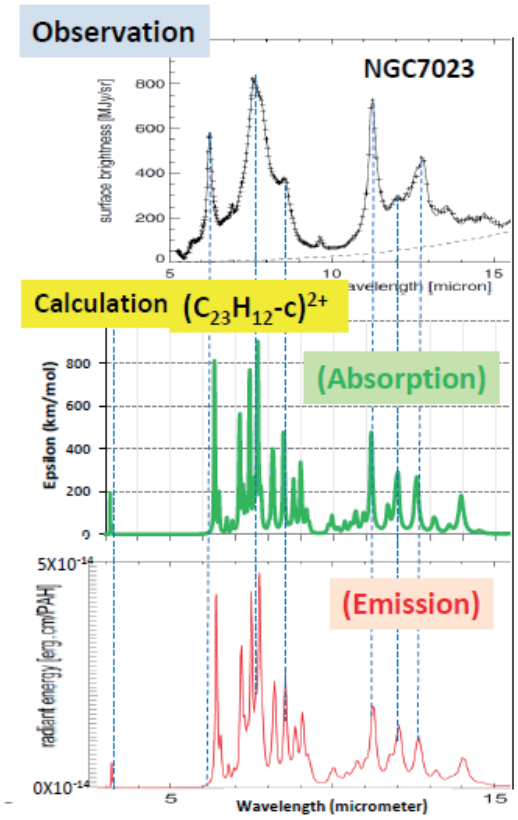

Fig. 8 Calculated emission spectrum on bottom was compared with observed one of NGC7023 nebula on top. Absorbed bands in middle are mirror image of emission one.

Table 1 Fundamental mode of $(C_{23}H_{12}\text{-}c)^{2+}$.

$(C_{23}H_{12}\text{-}c)^{2+}$

Mode number	Energy (cm^{-1})	Wavelength after scaling (μm)	Vibrational Intensity (km/mol)	Vibrational behavior
1	97.0	106.9	4.6	
11	352.3	29.4	86.9	molecular out-of-plane vibration
17	487.0	21.3	46.5	molecular out-of-plane vibration
25	626.4	16.5	45.5	molecular out-of-plane vibration
36	825.6	12.6	81.0	C-H out-of-plane bending at pentagon site
43	927.8	11.2	136.1	C-H out-of-plane bending at all sites
56	1150.7	9.0	101.2	C-H in-plane bending at all sites
61	1221.9	8.5	165.8	C-H in-plane bending, C-C stretching
62	1270.2	8.2	103.4	C-H in-plane bending, C-C stretching
69	1349.8	7.7	290.1	C-H in-plane bending, C-C stretching
70	1369.2	7.6	61.9	C-H in-plane bending, C-C stretching
71	1393.7	7.4	258.5	C-H in-plane bending, C-C stretching
74	1433.1	7.2	57.4	C-H in-plane bending, C-C stretching
75	1451.7	7.1	102.5	C-H in-plane bending, C-C stretching
77	1457.2	7.1	84.6	C-H in-plane bending, C-C stretching
86	1625.3	6.4	60.7	C-C stretching at hexagons
87	1630.6	6.4	239.4	C-C stretching at hexagons
98	3283.5	3.2	42.6	C-H stretching at pentagon sites
99	3284.0	3.2	13.0	

6. Large Molecule ($C_{53}H_{18}$)

6.1 Model molecules

Possible origin of featured spectrum was suggested to be SP3 defect among SP2 network. Such mechanism should not depend on molecular size. Here, we tried large molecule starting from circum-coronene ($C_{54}H_{18}$). As shown on top of Fig. 9, there are 6 kind of void positions named by a, b, c, d, e, and f.

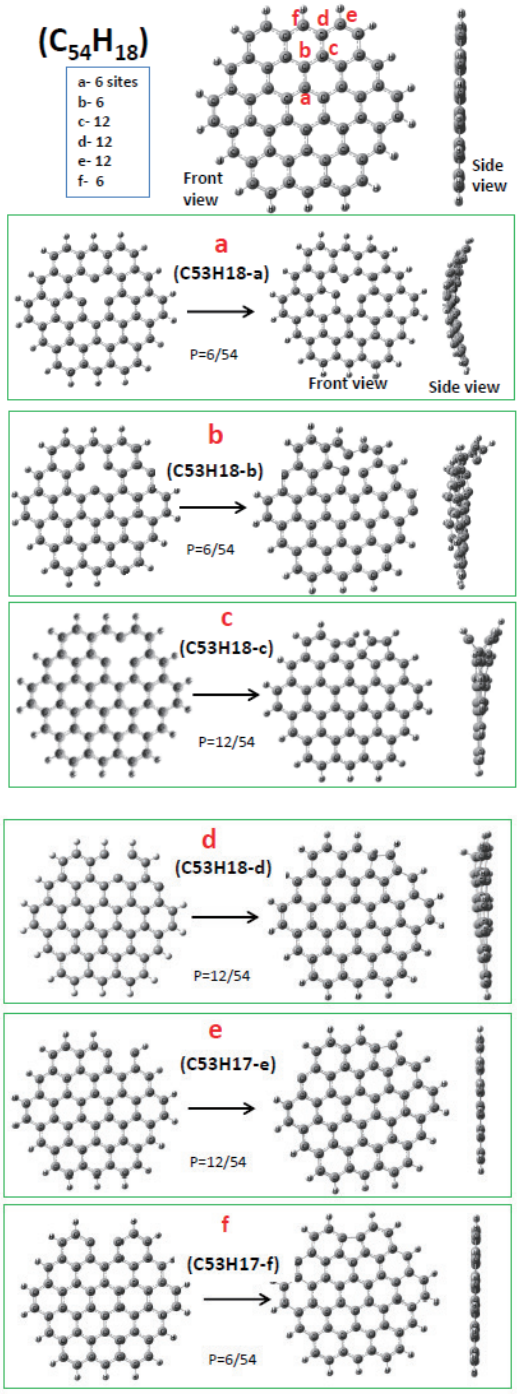

Fig. 9 Void-defect induced species of ($C_{54}H_{18}$) family.

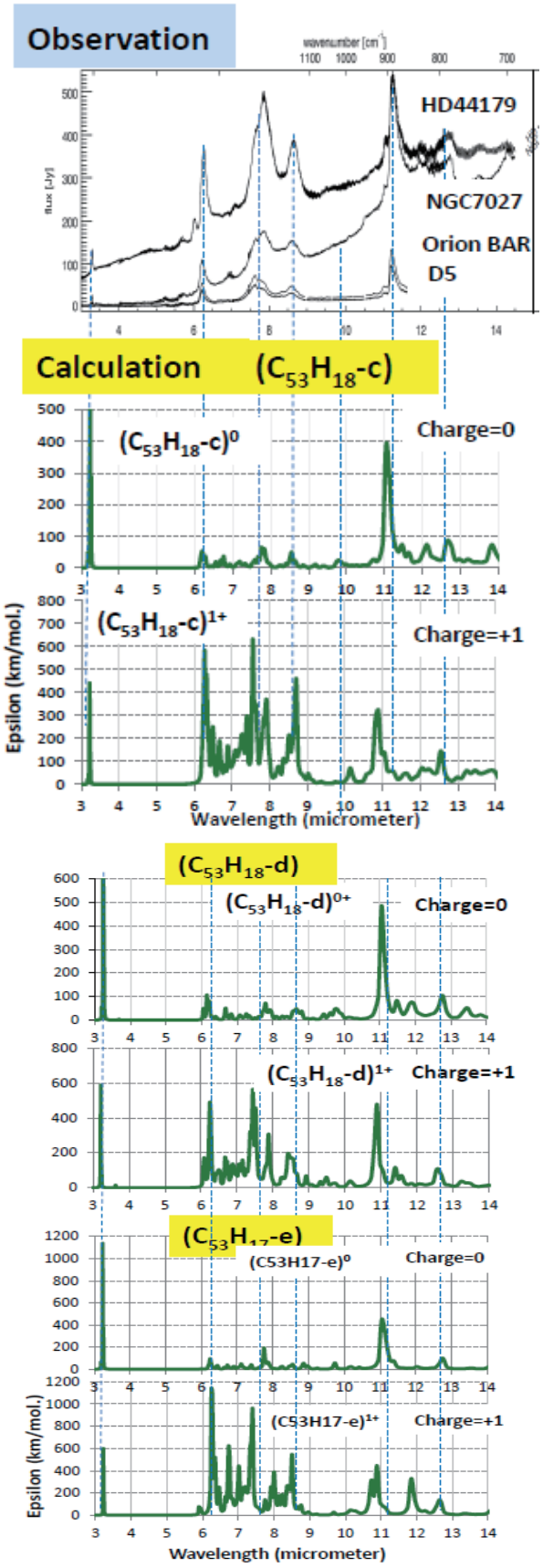

Fig. 10 Calculated spectra of ($C_{53}H_{18}$) species compared with astronomical observation.

Void-a induces a species of ($C_{53}H_{18}$-a) showing an umbrella like structure having one carbon pentagon ring as illustrated in column-a of Fig. 9. Also, ($C_{53}H_{18}$-b) show a similar structure. It is interesting that ($C_{53}H_{18}$-c) has two pentagon rings and show similar structure to previously calculated case of ($C_{23}H_{12}$-c). In ($C_{53}H_{18}$-d), one hydrogen brings an umbrella like structure introduced by SP3-H bond. In case of ($C_{53}H_{17}$-e), C-H fragment was removed, which show flat structure including one pentagon ring. Also, void-f brings a flat molecule of ($C_{53}H_{18}$-f).

6.2 Infrared spectrum

Infrared spectra for charge 0 and +1 of void-c, -d and –e induced species are calculated as shown in Fig. 10. Di-cation spectra were listed on Appendix. Among them, it was amazing that mono-cation molecule of $(C_{53}H_{18}\text{-c})^{1+}$ shows good coincidence with astronomically observed bands at 3.3, 6.2, 7.6, 7.8, and 8.6 μm. Whereas, neutral molecule shows bands at 11.1 and 12.7μm close to observation. Observed spectrum will be a sum of those neutral and ionized molecule's spectrum. Similarly, ($C_{53}H_{18}$-d) also shows good coincidence with observation. In addition, ($C_{53}H_{17}$-e) shows coincidence at 6.2, 7.6, and 8.6 μm with mono-cation, and at 11.1 μm with neutral one. It was concluded that many species could reproduce ubiquitously observed astronomical spectrum. It was revealed that our finding is not an accidental one.

7. Small Molecule ($C_{12}H_8$)

7.1 Model Molecules

We tried small size molecules of ($C_{12}H_9$) and ($C_{12}H_8$) created from mother molecule of ($C_{13}H_9$) as shown in Fig. 11. Void-c induced molecule of ($C_{12}H_9$-c) has a complex structure with void creation capability of p=1/13 (1 void among 13 carbons). Void-d induces umbrella like configuration of ($C_{12}H_9$-d). Void-e and void-f both lose one (C-H) fragment to show the same flat configuration as ($C_{12}H_8$-e), and ($C_{12}H_8$-f). This is a major species having void capability of p=9/13.

7.2 Infrared Spectrum

Calculated spectra are listed in Fig. 12, which show different spectra with ubiquitously observed one as illustrated in Fig. 7. It was amazing that some coincidence of calculated spectra was found with young star's observed spectrum, especially observed at protoplanetary disks around the Herbig Ae/Be and T Tauri stars, which were reported by Acke et al. in 2010[50] and by Seok and Li in 2017[51].

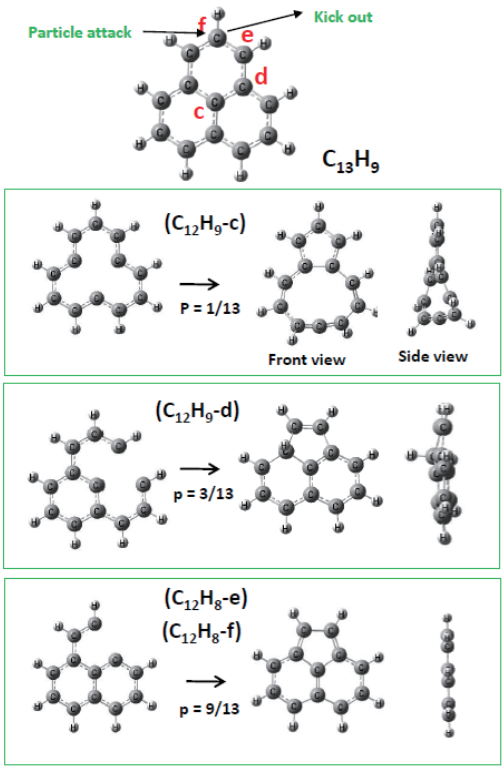

Fig 11 Void induced small size molecules.

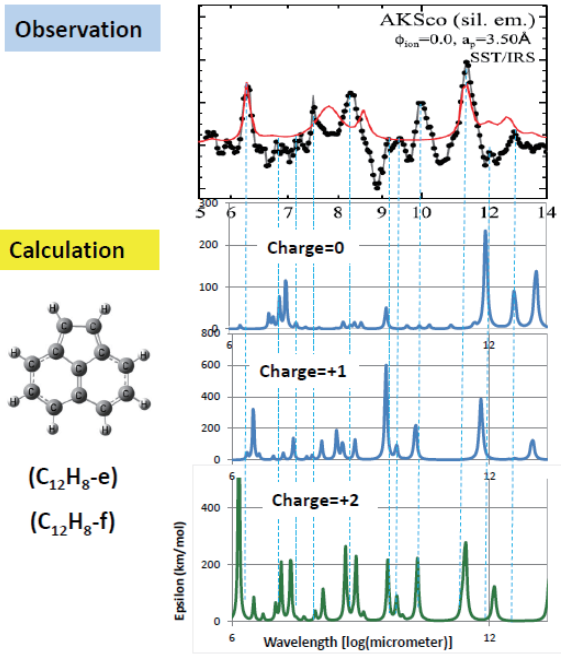

Fig. 13 Observed spectrum of young star AKSco was well reproduced by $(C_{12}H_8\text{-e})^{2+}$.

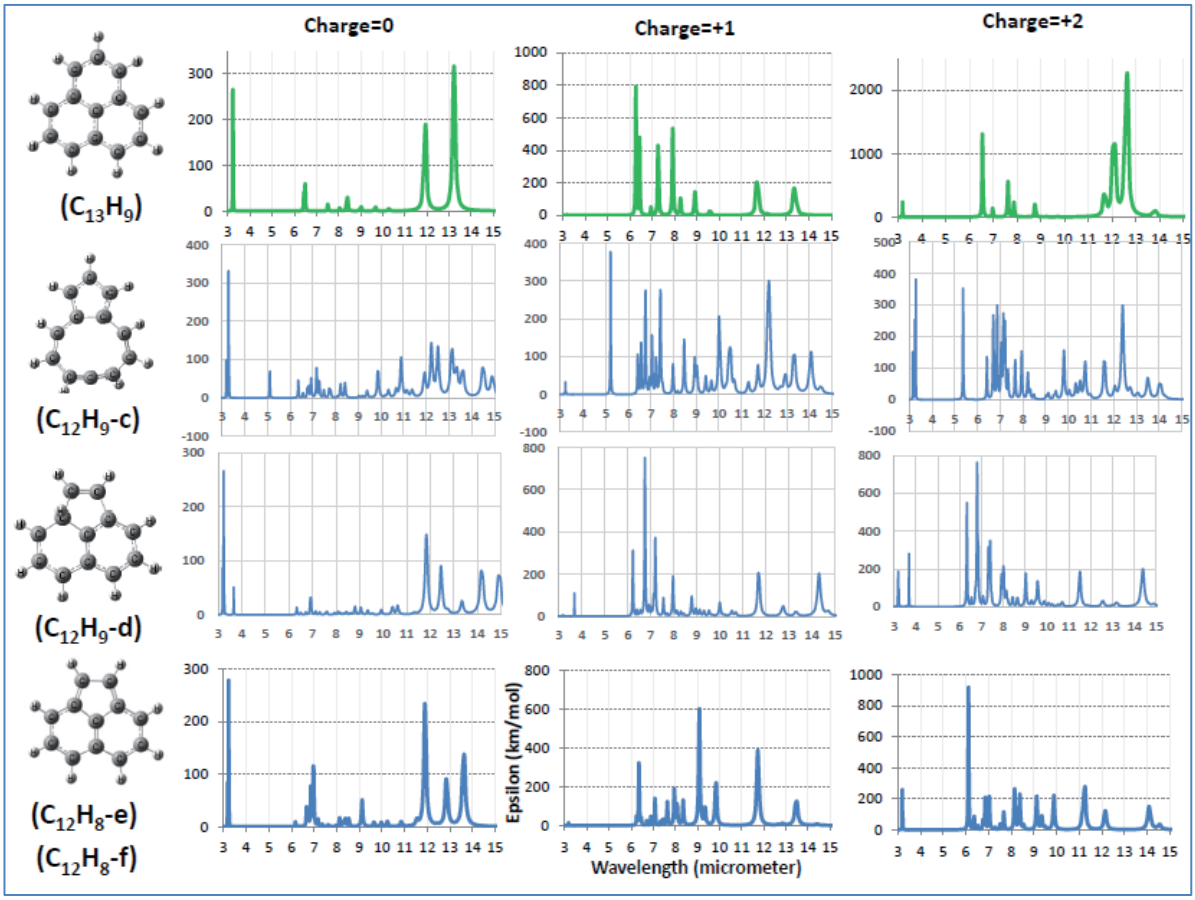

Fig. 12 Small molecule's calculated infrared spectra.

Recently, young star interested many scientists, because it is an analogy of baby age of our solar system and planets. We can understand how planet system will be created in the Universe. Among more than 60 observed spectra by Seok and Li[51], we found 9 samples coincident with spectrum of di-cation $(C_{12}H_8\text{-e})^{2+}$. Typical example is AKSco as shown in Fig. 13. It was a surprise that such complex spectrum can be reproduced well with calculated spectrum of di-cation $(C_{12}H_8\text{-e})^{2+}$. We can see good coincidence at many bands of 6.2, 6.8, 7.2, 7.5, 8.2, 9.1, 10.0, 11.3, 12.0, and 12.7 μm. Another example is shown in Fig. 14 for observed spectrum of HD31648. Again, there are many complex bands. We analyzed that most bands coincide well again with calculated one of $(C_{12}H_8)^{2+}$, which are marked by blue dotted lines. Also, we found that several bands will be identified partly by $(C_{23}H_{12}\text{-c})^{2+}$ marked by red dotted lines. We could reproduce observed spectrum by a sum of those molecules.

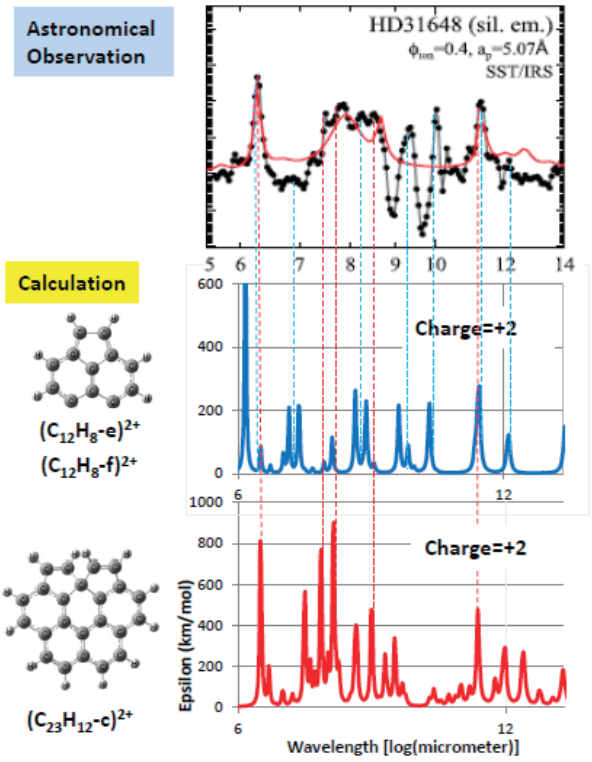

Fig. 14 Complex spectrum of young star HD31648 was reproduced well by a sum of $(C_{12}H_8\text{-e})^{2+}$ and $(C_{23}H_{12}\text{-c})^{2+}$.

8. Conclusion

Void-defect induced magnetism and structure change of polycyclic aromatic hydrocarbon molecules (PAH) were studied by density functional theory (DFT) and by astronomical observation.

(1) Model molecule of $(C_{23}H_{12})$ was introduced by making a void-defect on $(C_{24}H_{12})$. Induced species have one or two carbon pentagon rings among hexagon ring networks.

(2) Single void holds six spins and cause spin multiplicity. Stable spin-state of $(C_{23}H_{12})$ was singlet, which is contrary to pure carbon case of (C_{23}) with triplet one. Hydrogen plays an important role to diminish magnetism by bringing SP3-bond among SP2-networks.

(3) Molecular charge brings serious change on magnetism and structure, which finally affect molecular vibrational spectrum in infrared region. Di-cation molecule $(C_{23}H_{12})^{2+}$ shows featured bands at 3.3, 6.2, 7.6, 7.8, 8.6, 11.2, and 12.7 μm. It was amazing that those calculated bands coincident well with astronomically observed bands. This study will be the first indication to suggest specific PAH in space.

(4) To confirm our finding, large model molecule of $(C_{53}H_{18})$ was tested. Most of mono-cation $(C_{53}H_{18})^{1+}$ showed again featured bands reproducing astronomically observed one.

(5) In addition, small size molecules of $(C_{12}H_9)$ are tested. It was a surprise that calculated spectrum shows good coincidence with young star's unusual complex spectrum.

It was revealed that void induced PAH is a promising candidate of cosmic hydrocarbon molecule.

Acknowledgement

Aigen Li is supported in part by NSF AST-1311804 and NASA NNX14AF68G.

Norio Ota would like to say great thanks to Dr. Christiaan Boersma, NASA Ames Research Center, to provide the calculated emission infrared spectrum based on our DFT analysis, and to apply it to his observation.

References

(Note on abbreviation of astronomical journals,
ApJ: The Astrophysical Journal
ApJL: The Astrophysical Journal Letters
A&A: Astronomy and Astrophysics
MNRAS: Monthly Notices of the Royal Astronomical Society
PNAS: Proceedings of the National Academy of Sciences)

1) P. Esquinazi, D. Spemann, R. Hohne, A.Setzer, K. Han, and T. Butz: *Phys. Rev. Lett.*, **91**, 227201 (2003).
2) K. Kamishima, T. Noda, F. Kadonome, K. Kakizaki and N. Hiratsuka: *J. Mag. Magn. Mat.*, **310**, e346 (2007).
3) T. Saito, D. Nishio-Hamane, S. Yoshii, and T. Nojima: *Appl. Phys. Lett.*, **98**, 052506 (2011).
4) Y. Wang, Y. Huang, Y. Song, X. Zhang, Y. Ma, J. Liang and Y. Chen: *Nano Letters* , **9,** 220 (2009).
5) J. Cervenka, M. Katsnelson and C. Flipse: *Nature Phys.*, **5**, 840 (2009), (https://doi.org/10.1038/nphys1399) .
6) H. Ohldag, P. Esquinazi, E. Arenholz, D. Spemann, M. Rothermal, A. Setzer, and T. Butz: *New Journal of Physics*,

12, 123012 (2010).
7) J. Coey, M. Venkatesan, C. Fitzgerald, A. Douvalis and I. Sanders: *Nature*, **420**, 156 (2002).
8) K. Kusakabe and M. Maruyama: *Phys. Rev. B*, **67**, 092406 (2003).
9) N. Ota, N. Gorjizadeh and Y. Kawazoe: *J. Magn. Soc. Jpn.*, **35**, 414 (2011), also **36**, 36 (2012).
10) N. Ota: *J. Magn. Soc. Jpn.*, **37**, 175 (2013).
11) P. Lehtinen, A. Foster, Y. Ma, A. Krasheninnikov, and R. Nieminen: *Phys. Rev. Lett.* , **93**, 187202 (2004).
12) P.Ruffieux, O. Groning, P. Schwaller, L. Schlapbach, and P. Groning: *Phys. Rev. Lett.*, **84,** 4910 (2000).
13) A. Hashimoto, K. Suenaga, T. Sugai, H.Shinohara, and S. Iijima: *Nature (London),* **430**, 870 (2004).
14) K.Kelly and N.Hales: *Sur. Sci.*, **416**, L1085 (1998).
15) T. Kondo, Y. Honma, J. Oh, T. Machida, and J. Nakamura: *Phys. Rev. B*, **82**, 153414 (2010).
16) M. Ziatdinov, S. Fujii, K. Kusakabe, M. Kiguchi, T. Mori, and T. Enoki: *Phys. Rev. B, 89*, 155405 (2014).
17) N. Ota, and L. Nemes: *J. Mag. Soc. Japan*, **45**, 30 (2021).
18) K.Kelly and N.Hales: *Surface science*, **416**, L1085 (1998).
19) T. Kondo, Y. Honma, J. Oh, T. Machida, and J. Nakamura: *Phys. Rev. B*, **82**, 153414 (2010).
20) M. Ziatdinov, S. Fujii, K. Kusakabe, M. Kiguchi, T. Mori, and T. Enoki: *Phys. Rev. B* **89,** 155405 (2014).
21) N. Ota, A. Li, L. Nemes and M. Otsuka: *J. Mag. Soc. Japan*, **45**, 41 (2021).
22) J. Cami, J. Bernard-Salas, E. Peeters and S. E. Malek: *Science,* **329**, 1180 (2010).
23) M. Otsuka, F. Kemper, M. L. Leal-Ferreira, M. L. Aleman, M. L. Bernard-Salas, J. Cami, B. Ochsendorf, E. Peeters, and P. Scicluna: *MNRAS*, **462,** 12 (2016).
24) C. Moutou,, K. Sellgren, L. Verstraete, and A. L´eger: A & A, **347**, 949 (1999).
25) E. Peeters, S. Hony, C. van Kerckhoven, et al. : A&A, **390**, 1089 (2002).
26) L.Armus, V.Charmandaris, J.Bernard-Salas, ApJ, **656**,148 (2007).
27) J. Smith, B. Draine, A. Dale, et al.: *ApJ* **656**, 770 (2007).
28) K. Sellgren, K. Uchida and M. Werner: *ApJ* **659**, 1338 (2007).
28) A. Ricca, C. W. Bauschlicher, C. Boersma, A.Tielens & L. J. Allamandola: *ApJ*, 754, 75 (2012).
29) A. Li: *Nature Astronomy*, **4**, 339 (2020).
30) J. Szczepanski, and M. Vala: *ApJ* **414**, 646 (1993).
31) S. Schlemmer, D. Cook, J. Harrison, et al.: *Science* **265**, 1686 (1994).
32) D.Hudgins, and L. Allamandola,: *ApJ* **513**, L69 (1999).
33) J. Oomens: *In PAHs and the Universe*: A Symposium to Celebrate the 25th Anniversary of the PAH Hypothesis, EAS Publications Series (2011).
34) S.Langhoff: *J. Phys. Chem.* **100**, 2819 (1996).
35) C. Bauschlicher, and S. Langhoff: *Spectrochim. Acta A*, **53**, 1225 (1997).
36) C. Bauschlicher, E. Peeters, and L. Allamandola: *ApJ,* **678**, 316 (2008).
37) A. Ricca, C. Bauschlicher, C. Boersma, A. Tielens and L. Allamandola: *ApJ* **754**, 75 (2012).
38) C. Boersma, J. Bregman, and L. Allamandola: *ApJ* **769**, 117 (2013).
39) A. Ricca, C. Bauschlicher, C. Boersma, A. Tielens , and L. Allamandola: *ApJ* **754**, 75 (2012).
40) P. Hohenberg and W. Kohn: *Phys. Rev.*, **136**, B864 (1964).
41) W. Kohn and L. Sham: *Phys. Rev.*, **140**, A1133(1965).
42) A. Becke: *J. Chem. Phys.*, **98**, 5648 (1993).
43) M. Frisch, G. Trucks, H. Schlegel et al: Gaussian 09 package software, Gaussian Inc. Wallington CT USA (2009).
44) R. Ditchfield, W. Hehre and J. Pople: *J. Chem. Phys.,* **54**,724(1971).
45) N. Ota: *arXiv,* 1412.0009 (2014), Additional data for scaling factor on *arXiv,* 1502.01766, for emission spectrum on *arXiv,* 1703.05931, for SP3 defect on *arXiv,* 1808.01070.
46) F. Hund: *Z. Phys.* **33**, 345 (1923).
47) C. Boersma, A. L. Mattioda, C. W. Bauschlicher Jr, E. Peeters, A. G. G. M. Tielens, and L. J. Allamandola: *ApJ,* **690**, 1208 (2009).
48) A. Li and B. T. Draine: *ApJ,* **554**, 778 (2001).
49) B. T. Draine and A. Li: *ApJ,* **551**, 807 (2001).
50) B. Acke, J. Bouwman, A. Juhasz, Th. Henning, M.E. van den Ancker, G. Meeus, A.G.G.M. Tielens and L.B.F.M. Waters: *ApJ* **718**, 558 (2010).
51) J. Y. Seok and A. Li: *ApJ,* **835**, 291 (2017).

Appendix Calculated spectrum of ($C_{53}H_{18}$) species.

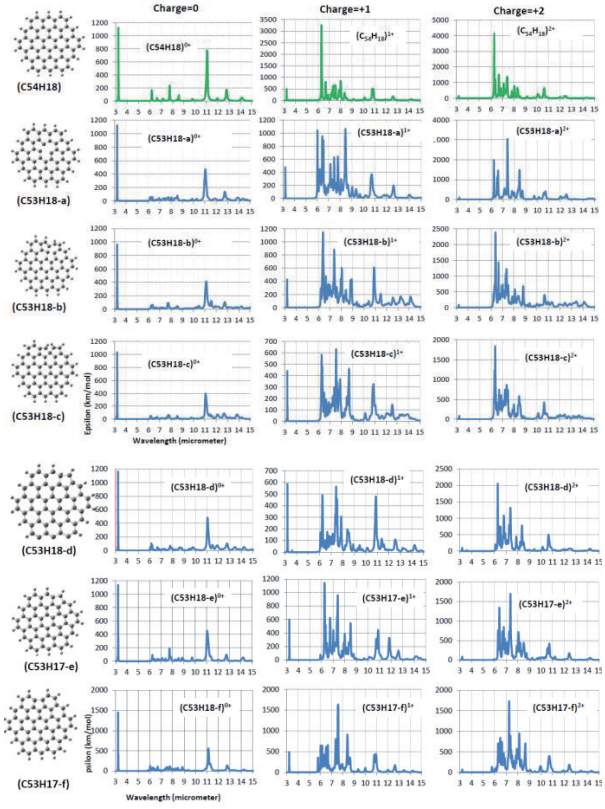

Received Jan. 26, 2021; Accepted April 14, 2021

J. Magn. Soc. Jpn., **45**, 96-100 (2021)

<Paper>

Perpendicular Anisotropy and Damping of MBE-grown MgO/Fe/Au(001) and Au/Fe/Au(001) Trilayers

N. Kamiya, D. Oshima*, S. Iwata**, and T. Kato*

Department of Electronics, Nagoya Univ., *Furo-cho, Chikusa-ku, Nagoya 464-8603, Japan*

*Institute of Materials and Systems for Sustainability, Nagoya Univ., *Fuco-cho, Chikusa-ku, Nagoya 464-8603, Japan*

**Department of Research, Nagoya Industrial Science Research Institute., *1-13 Yotsuya-dori, Chikusa-ku, Nagoya 464-0819, Japan*

MgO/Fe/Au(001) and Au/Fe/Au(001) trilayers with Fe layer thickness from 0.4 to 1.2 nm were grown by the molecular beam epitaxy (MBE) method, and the perpendicular magnetic anisotropy (PMA) and magnetization dynamics of the trilayers were studied. The MgO/Fe/Au trilayer exhibited a slightly larger interface anisotropy than the Au/Fe/Au trilayer, and the effective anisotropy of both trilayers decreased with increasing Fe thickness due to the shape anisotropy. The g-factor of both trilayers decreased from the bulk value with decreasing Fe thickness, and MgO/Fe/Au showed a slightly lower g-factor than Au/Fe/Au. The effective damping constant α of both trilayers increased with decreasing Fe thickness due to the effect of spin pumping, and interestingly the MgO/Fe/Au trilayers showed large damping compared with the Au/Fe/Au ones. These results suggest that the broken inversion symmetry in MgO/Fe/Au leads to a large PMA and damping through Rashba spin-orbit coupling.

Key words: magnetization dynamics, perpendicular anisotropy, Rashba spin-orbit coupling, MgO/Fe/Au

1. Introduction

Perpendicular magnetic anisotropy (PMA) and Gilbert damping are quite important for the efficient writing of the memory cell of spin-transfer-torque magnetic random access memories (STT–MRAM). Recently, insulator / 3d ferromagnet / 5d metal trilayers with broken inversion symmetry along the film normal direction is of great interest, since the broken symmetry is reported to contribute PMA[1] and conversion in-plane current to perpendicular spin current[2] through Rashba spin-orbit coupling. Moreover, PMA of such trilayers is known to be controlled by the application of electric field[3)–6)], which is quite attractive for voltage-torque magnetization switching[7]. The voltage-torque switching is expected to significantly reduce power consumption of MRAM compared to conventional STT–MRAM. In spite of many experimental and theoretical studies of PMA of such trilayers, only few reports on magnetization dynamics[8), 9)], although the magnetization dynamics is also important for the efficient writing of magnetic materials.

In this report, PMA and magnetization dynamics of MgO/Fe/Au trilayers with broken inversion symmetry were investigated and compared with those of Au/Fe/Au with a symmetric structure in order to discuss the influence of Rashba spin-orbit coupling on the magnetization dynamics. Gilbert damping is known to be proportional to the second-order of spin-orbit interaction[10], however, there has been no report on the relationship between magnetization dynamics and broken inversion symmetry to the extent of our knowledge. Here we report the reduction of g-factor and increase of damping constant α of symmetry broken MgO/Fe/Au trilayers compared to symmetric Au/Fe/Au trilayers. These results are different from those of MgO/CoFeB/Ta trilayers which exhibit smaller damping constant compared to Ta/CoFeB/Ta due to the suppress of the spin pumping effect at MgO/CoFeB interface[8), 9)].

Corresponding author: Takeshi Kato
(e-mail: kato.takeshi@b.mbox.nagoya-u.ac.jp).

2. Experiment

MgO(5) / Fe(t_{Fe}) / Au(20) / Cr(5) / MgO(001) and Au(2) / Fe(t_{Fe}) / Au(20) / Cr(5) / MgO(001) (thickness is in nm) were grown by molecular beam epitaxy (MBE) method in an ultra-high vacuum less than 5×10^{-7} Pa. The thickness of Fe layer, t_{Fe}, was varied from 0.4 nm to 1.2 nm. Prior to the deposition, MgO substrate was cleaned by Ar^+ ion bombardment with an acceleration energy of 1 kV followed by annealing at 1000˚C for 2 min. All the layers were deposited at temperature less than 100˚C, and Au(20) under layer was annealed at 400˚C for 30 min to obtain atomically flat Au surface before the deposition of Fe layer. The deposition rate for all layers were fixed at 0.01 nm/s. Sample structure during the deposition was monitored by reflection high energy electron diffraction (RHEED), and hysteresis loops of the samples were measured by alternating gradient field magnetometer (AGM). Time-resolved magneto-optical Kerr effect (TRMOKE) of the MgO/Fe/Au and Au/Fe/Au trilayers were measured by pump-probe method similarly to our previous works[11)–13)]. Laser beam from an ultra-short pulse fiber laser with a wavelength of 1040 nm, pulse width of 500 fs, a repetition frequency of 100 kHz were split into pump and probe beams, where the probe beam was frequency doubled by a heated lithium borate (LBO) crystal. Typical fluences of the pump and probe beams on the sample were 0.6 mJ/cm^2 and 0.05 mJ/cm^2, respectively. During TRMOKE measurements, an external field H_{ext} up to 14 kOe was applied in the direction θ_H = 40–85˚ from the film normal.

3. Results and Discussion

3.1 Film structure

Figure 1 shows RHEED patterns after the deposition of (a), (b) Au(20) under layer, (c), (d) Fe(0.9) layer, (e) MgO(5) upper layer, and (f) Au(2) upper layer, where electron beam was incident along (a), (c), (e), (f) MgO[100] and (b), (d) MgO[110]. As shown in Figs. 1 (a) and (b), atomically flat Au (001) surface with (5 × 1) reconstruction was obtained. The Fe layer was epitaxially grown on Au under layer with a relation Fe(001)[110] // Au(001)[100] as confirmed from RHEED patterns in Figs. 1 (c) and (d). Moreover, the streak patterns show layer-by-layer growth of Fe on Au surface. MgO and Au upper layers were also grown epitaxially on Fe layer as shown in Figs. 1 (e) and (f). All samples in this study were confirmed grow epitaxially on MgO(001) similar to Fig. 1.

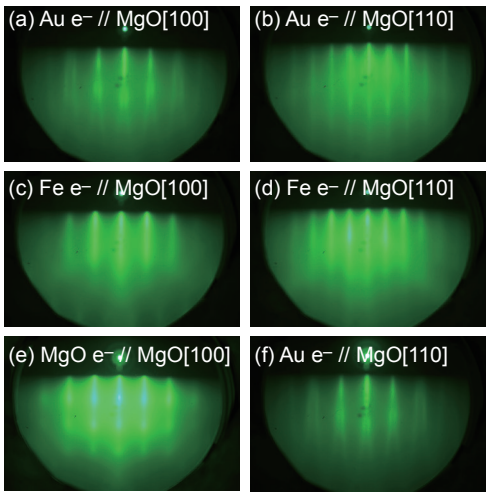

Fig. 1 RHEED patterns after deposition of (a), (b) Au(20) under layer, (c), (d) Fe(0.9) layer, (e) MgO(5) upper layer, and (f) Au(2) upper layer. Electron beam was incident parallel to (a), (c), (e), (f) MgO[100] and (b), (d) MgO[110].

3.2 Magnetic anisotropy

Figure 2 shows *M*–*H* loops of (a) MgO/Fe/Au and (b) Au/Fe/Au trilayers with various Fe thicknesses. The loops were measured applying a field along the film normal direction, and the magnetization is normalized so that saturation magnetization M_s equals to unity. Both trilayers, exhibited smaller saturation field for thinner Fe thickness, indicating the interface anisotropy becomes competitive for the trilayers with t_{Fe} ~ 0.4 nm. By comparing Figs. 2 (a) and (b), MgO/Fe/Au tends to have smaller saturation field than Au/Fe/Au, and obviously MgO / Fe(0.4) / Au exhibited larger PMA than Au / Fe(0.4) / Au. This suggests that PMA was enhanced by the broken inversion symmetry in MgO/Fe/Au trilayers through Rashba spin-orbit coupling[1]. Larger interface

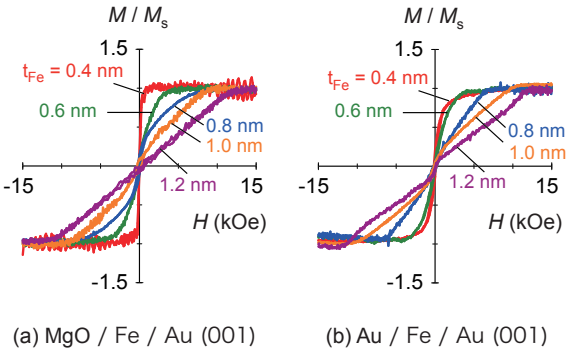

Fig. 2 *M*–*H* loops along film normal direction of (a) MgO/Fe/Au and (b) Au/Fe/Au trilayers with various Fe thicknesses. Magnetization was normalized so that saturation magnetization M_s equaled unity.

anisotropy of MgO/Fe/Au than Au/Fe/Au was also reported in first-principle calculation[14].

3.3 Magnetization dynamics

Figure 3 shows typical TRMOKE waveforms of the Au/Fe(0.6)/Au trilayer measured under various external fields H_{ext} where the field direction was fixed at $\theta_H = 40^\circ$. In Fig. 3, exponentially decayed background in the raw TRMOKE data was subtracted[11]. The solid lines in Fig. 3 are fitted curves with the damped oscillation function, $A\exp(-t/\tau)\sin\omega t$, where τ is the relaxation time and ω is

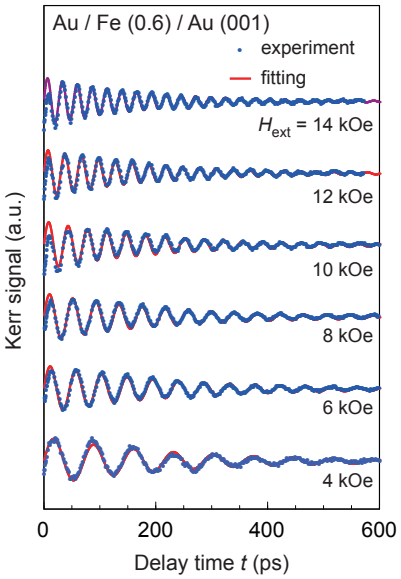

Fig. 3 TRMOKE waveforms of Au/Fe(0.6)/Au trilayer measured under various H_{ext}. Direction of H_{ext} was fixed at $\theta_H = 40^\circ$ from the film normal. Closed circles and solid lines are experimental and fitting results, respectively.

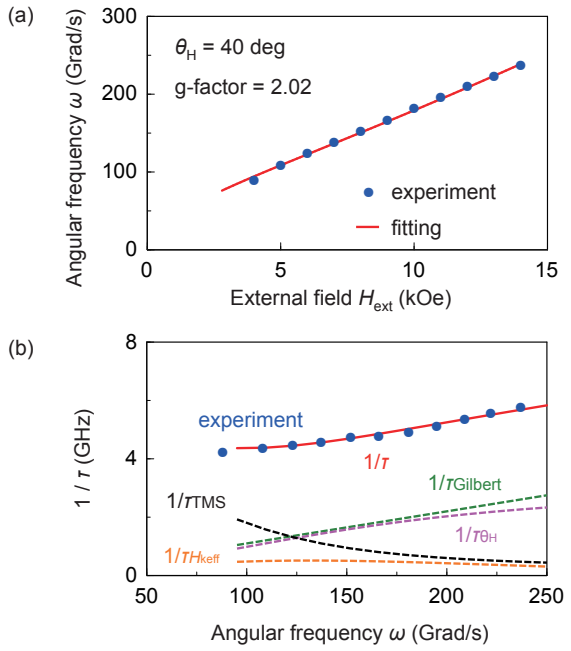

Fig. 4 (a) H_{ext} dependence of angular frequency ω and (b) ω dependence of inverse of relaxation time $1/\tau$ obtained for Au/Fe(0.6)/Au trilayer. Solid lines in Figs. (a) and (b) represent the fitting with Eq. (1) and Eq. (5), respectively. Dashed lines in Fig. (b) represent four contributions in Eq. (5).

the angular frequency of the precession. Figure 4 shows (a) H_{ext} dependence of angular frequency ω and (b) ω dependence of inverse of relaxation time $1/\tau$. The following analytical expressions were used to fit the H_{ext} dependence of ω[15), 16)].

$$\omega = \gamma\sqrt{H_{\theta\theta 0}H_{\phi\phi 0}} \tag{1}$$

$$H_{\theta\theta 0} = H_{\mathrm{ext}}\cos(\theta_H - \theta) + H_{\mathrm{keff}}\cos^2\theta \tag{2}$$

$$H_{\phi\phi 0} = H_{\mathrm{ext}}\cos(\theta_H - \theta) + H_{\mathrm{keff}}\cos 2\theta \tag{3}$$

where $\gamma = \mu_B g/\hbar$ is the gyromagnetic constant, and μ_B, $\hbar$, g, and θ are Bohr magneton, Dirac constant, g-factor, and the stable magnetization angle from the film normal, respectively. θ is estimated by minimizing the following magnetic energy.

$$E = -M_s H_{\mathrm{ext}}\cos(\theta_H - \theta) + \frac{M_s H_{\mathrm{keff}}}{2}\sin^2\theta \tag{4}$$

The solid line in Fig. 4 (a) represents fitting with Eq. (1) to evaluate H_{keff} and g of Au/Fe(0.6)/Au trilayer. The dependence of $1/\tau$ on ω was fitted with the following expression taking into account Gilbert damping α, anisotropy distribution ΔH_{keff}, anisotropy axis distribution $\Delta\theta_H$, and two-magnon scattering (TMS)[16)–20)].

$$\frac{1}{\tau} = \frac{1}{\tau^{\mathrm{Gilbert}}} + \frac{1}{\tau^{\theta_H}} + \frac{1}{\tau^{H_{\mathrm{keff}}}} + \frac{1}{\tau^{\mathrm{TMS}}}$$

$$= \frac{\alpha\gamma}{2}(H_{\theta\theta 0} + H_{\phi\phi 0}) + \frac{1}{2}\left|\frac{\partial\omega}{\partial\theta_H}\right|\Delta\theta_H$$

$$+\frac{1}{2}\left|\frac{\partial\omega}{\partial H_{\mathrm{keff}}}\right|\Delta H_{\mathrm{keff}} + \frac{1}{\tau^{\mathrm{TMS}}} \tag{5}$$

The $1/\tau^{TMS}$ was calculated as described in Appendix. We used α, ΔH_{keff}, and $\Delta\theta_H$ as fitting parameters, and the solid line in Fig. 4 (b) represents fitting with Eq. (5), for α = 0.011, ΔH_{keff} = 225 Oe, and $\Delta\theta_H$ = 1.5°. Four contributions in Eq. (5) are also shown as dashed lines in Fig. 4 (b). Gilbert term has a linear dependence on ω, while TMS term shows a decreasing trend with increasing ω. The sum of TMS and $\Delta\theta_H$ terms tends to move $1/\tau$ upward. The TMS term is proportional to ΔH_{keff}^2 as in Appendix, and thus we fit $1/\tau$ vs ω by varying α, ΔH_{keff}, and $\Delta\theta_H$.

Figure 5 shows the dependence of (a) H_{keff}, (b) g, and (c) α on the reciprocal Fe layer thickness of MgO/Fe/Au and Au/Fe/Au trilayers. ΔH_{keff} and $\Delta\theta_H$ for the fitting were ΔH_{keff} = 150 ~ 400 Oe and $\Delta\theta_H$ = 1.5 ~ 2.5°, respectively, for all the trilayer. The thickness dependence of H_{keff} is expected to follow the equation,

$$H_{\mathrm{keff}} = \frac{2K_s}{M_s t_{\mathrm{Fe}}} - \frac{2K_v}{M_s}, \tag{6}$$

where K_s is the surface anisotropy of both interfaces and

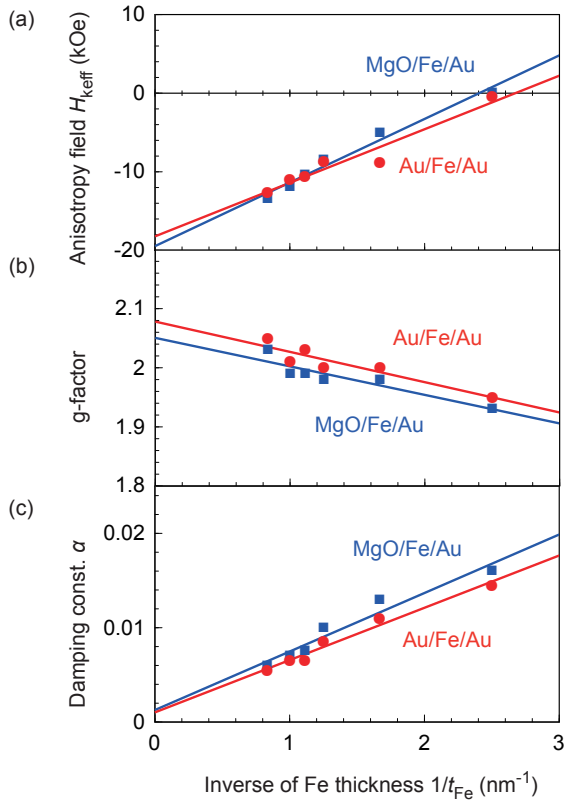

Fig. 5 Dependence of (a) anisotropy field H_{keff}, (b) g-factor, and (c) damping constant α on reciprocal Fe thickness $1/t_{Fe}$ of MgO/Fe/Au and Au/Fe/Au trilayers estimated by fitting with Eq. (5). Solid lines show simple linear fit of the data.

K_v is volume anisotropy consisting of crystalline and shape anisotropies. From Fig. 5 (a), K_v is estimated to be around -1.6×10^7 erg/cc for both trilayers, which is roughly consistent with the shape anisotropy, $2\pi M_s^2 = 1.8 \times 10^7$ erg/cc. Large slope was confirmed for MgO/Fe/Au compared to Au/Fe/Au, and K_s = 0.69 ± 0.05 mJ/cm^2 for MgO/Fe/Au and K_s = 0.58 ± 0.07 mJ/cm^2 for Au/Fe/Au, which agrees with the discussion in Fig. 2. The g-factor of both trilayers decreased from ~2.05 to ~1.95 with decreasing the thickness, and approaches to 2.07 when the thickness of Fe is infinitely thick, which is roughly consistent with the bulk value (g = 2.09)[21]. The decrease of g-factor with decreasing the Fe thickness is expected in the presence of the interfacial anisotropy[22, 23]. MgO/Fe/Au trilayers seem to have slightly lower g-factor, which may be related to Rashba spin-orbit coupling in symmetry broken MgO/Fe/Au trilayers. However, there exists the difference of g-factor between MgO/Fe/Au and Au/Fe/Au even when the thickness of Fe is infinitely thick, and thus we are not sure that the difference is significant.

The damping constants of both trilayers increased with decreasing the Fe thickness as shown in Fig. 5 (c), and approached to $\alpha \sim 0.001$ at $1/t_{Fe} = 0$. The intrinsic Gilbert damping α_{int} is reported to be 0.0025 for Fe, and to reduce to 0.0005 for $Fe_{75}Co_{25}$ due to the shift of Fermi energy[24]. These values roughly agree with the present extrapolated α by considering the error bar of the extrapolation of ±0.001. The increasing trend of α with decreasing t_{Fe} is due to the effect of spin pumping into Au layer. The enhanced damping due to the spin pumping is expressed by using effective spin mixing conductance $g_{eff}^{\uparrow\downarrow}$ as,

$$\Delta\alpha_{sp} = g\mu_B \frac{g_{eff}^{\uparrow\downarrow}}{4\pi M_s} \frac{1}{t_{Fe}}, \tag{7}$$

where μ_B is the Bohr magneton[25, 26]. Spin diffusion lengths of Au and Cr are reported to be λ_{Au} = 35 nm[27] and λ_{Cr} = 4.5 nm[28], respectively, which suggests that injected spin current into Au/Cr under layer will be fully absorbed. Thus the $g_{eff}^{\uparrow\downarrow}$ of Au/Fe/Au trilayer is given by,

$$g_{eff}^{\uparrow\downarrow} = g_{Au}^{\uparrow\downarrow} + g_{Au}^{\uparrow\downarrow}\left(1 - e^{-2t_{Au}/\lambda_{Au}}\right), \tag{8}$$

where $g_{Au}^{\uparrow\downarrow}$ is the spin mixing conductance at Fe/Au interface, and t_{Au} is upper Au thickness[26]. The 2nd term in Eq. (8) represents the spin pumping into upper Au layer. The slope of α of Au/Fe/Au trilayers was estimated to be 0.0055 ± 0.0004 nm^{-1} from Fig. 5 (c), which gives $g_{Au}^{\uparrow\downarrow} = 5.8 \times 10^{14}$ cm^{-2}, where g-factor is approximated to be 2. The estimated $g_{Au}^{\uparrow\downarrow}$ is comparable to the theoretical value[29] of $g^{\uparrow\downarrow} = 1.2 \times 10^{15}$ cm^{-2}. Based on Eq. (8), the effective spin mixing conductance $g_{eff}^{\uparrow\downarrow}$ of MgO/Fe/Au trilayers equals to $g_{Au}^{\uparrow\downarrow}$, because no spin current flows into insulating MgO layer. Thus the slope of α of MgO/Fe/Au trilayer is expected to be ~0.005 nm^{-1} (roughly 10% smaller than that of Au/Fe/Au trilayer, since the 2nd term of Eq. (8) disappears). However, the slope of α of MgO/Fe/Au trilayer is estimated to be 0.0062 ± 0.0007 nm^{-1} from Fig. 5 (c), indicating an additional interface contribution to the damping. Kambersky pointed out the damping constant is influenced by spin-orbit coupling and density of state at the Fermi level[10, 30]. As discussed in Fig. 2, larger PMA in MgO/Fe/Au than Au/Fe/Au may be related to Rashba spin-orbit coupling originated from broken inversion symmetry in MgO/Fe/Au, and Rashba spin-orbit coupling may also be responsible for the increase of the damping of MgO/Fe/Au. The reduction of the bandwidth of Fe is expected when insulating MgO is placed adjacent to Fe, which modifies the density of states.

4. Conclusion

MgO/Fe/Au(001) and Au/Fe/Au(001) trilayers with Fe layer thickness from 0.4 to 1.2 nm were grown by molecular beam epitaxy (MBE) method, and perpendicular magnetic anisotropy (PMA) and magnetization dynamics of the trilayers were studied. From TRMOKE measurements, MgO/Fe/Au trilayers were confirmed to exhibit slightly larger effective anisotropy H_{keff} than Au/Fe/Au trilayers. The large PMA of MgO/Fe/Au compared to Au/Fe/Au was also confirmed by M–H loop measurements. The g-factor of both trilayers decreased with decreasing the Fe thickness, and MgO/Fe/Au trilayers exhibited slightly lower g-factor than Au/Fe/Au trilayers. Damping constant α of both trilayers increased with increasing the Fe thickness due to the effect of spin pumping into Au layer. Surprisingly, MgO/Fe/Au shows larger damping constant than Au/Fe/Au even though no spin pumping is expected in the insulating MgO layer. The increase of the damping of MgO/Fe/Au compared to Au/Fe/Au may reflect the Rashba spin-orbit coupling and/or the variation in the density of states at the Fermi level.

Appendix

The contribution of two-magnon scattering $1/\tau^{TMS}$ in Eq. (5) is calculated as [16–20],

$$\frac{1}{\tau^{TMS}} = N_0 \int \frac{C(k)}{\omega} \mathrm{Im}\left(\frac{1}{\omega_{\mathbf{k}}^2 - \omega^2 + i\omega\delta\omega_{\mathbf{k}}}\right) d\mathbf{k}, \tag{A1}$$

where $\mathbf{k}$ is the magnon wave vector, and k is its amplitude. N_0, $C(k)$, $\omega_{\mathbf{k}}$, and $\delta\omega_{\mathbf{k}}$ are the scattering intensity, the correlation function, the spin wave dispersion, and the inverse lifetime of the spin wave, respectively, and these are expressed as[17, 18],

$$N_0 = \gamma^4\left(4H_{\theta\theta0}^2\cos^4\theta + 4H_{\phi\phi0}^2\cos^2 2\theta - 8H_{\theta\theta0}H_{\phi\phi0}\cos^2\theta\cos 2\theta\right)\Delta H_{keff}^2, \tag{A2}$$

$$C(k) = \frac{2\pi\xi^2}{(1+(k\xi)^2)^{3/2}}, \tag{A3}$$

$$\omega_{\mathbf{k}} = \gamma\sqrt{H_{\theta\theta}(\mathbf{k})H_{\phi\phi}(\mathbf{k})}, \tag{A4}$$

$$\delta\omega_{\mathbf{k}} = \alpha\gamma\left(H_{\theta\theta}(\mathbf{k}) + H_{\phi\phi}(\mathbf{k})\right), \tag{A5}$$

where ξ is the correlation length. $H_{\theta\theta}(\mathbf{k})$ and $H_{\phi\phi}(\mathbf{k})$ are given by[17],

$$H_{\theta\theta}(\mathbf{k}) = H_{\theta\theta 0} + \frac{M_s}{\mu_0}(1 - N_k)\cos^2\phi_{\mathbf{k}} + \frac{2A_{ex}}{M_s}k^2, \quad \text{(A6a)}$$

$$H_{\phi\phi}(\mathbf{k}) = H_{\phi\phi 0} + \frac{M_s}{\mu_0}(1 - N_k) \times\left\{ -\sin^2\theta + \cos^2\theta\sin^2\phi_{\mathbf{k}}\right\} + \frac{2A_{ex}}{M_s}k^2, \quad \text{(A6b)}$$

where μ_0 is the permeability of vacuum, A_{ex} the exchange stiffness, and $\phi_{\mathbf{k}}$ the azimuth angle of the spin wave. The wave number dependent demagnetizing factor N_k is given by[17],

$$N_k = \frac{1 - e^{kt_{Fe}}}{kt_{Fe}}. \quad \text{(A7)}$$

Here we set A_{ex} = 20 pJ/m, ξ = 2 nm, and M_s =1700 emu/cc, respectively to obtain the dashed line of the two-magnon contribution $1/\tau^{TMS}$ shown in Fig. 4 (b).

Acknowledgements The authors thank Mr. M. Kumazawa of Nagoya University for assistance in the experiments. This work was supported in part by JSPS KAKENHI Grant Number 17H03249, 17K18878, 17K19068, 19K15044, 20H02182, and by TATEMATSU foundation, and Tanaka Kikinzoku Memorial Foundation. This work was also supported in part by the Project of Creation of Life Innovation Materials for Interdisciplinary and International Researcher Development of the Ministry of Education, Culture, Sports, Science and Technology (MEXT), Japan. A part of this work was performed under the Research Program of "Dynamic Alliance for Open Innovation Bridging Human, Environment and Materials" in "Network Joint Research Center for Materials and Devices." A part of this work was conducted at the Nagoya University Nanofabrication Platform, supported by "Nanotechnology Platform Program" of MEXT, Japan.

References

1) S. E. Barnes, J. Ieda, and S. Maekawa: *Sci. Rep.*, **4**, 4105 (2014).
2) I. M. Miron, G. Gaudin, S. Auffret, B. Rodmacq, A. Schuhl, S. Pizzini, J. Vogel, and P. Gambardella: *Nat. Mater.*, **9**, 230 (2010).
3) T. Maruyama, Y. Shiota, T. Nozaki, K. Ohta, N. Toda, M. Mizuguchi, A. A. Tulapurkar, T. Shinjo, M. Shiraishi, S. Mizukami, Y. Ando, and Y. Suzuki: *Nat. Nanotech.*, **4**, 158 (2009).
4) Y. Shiota, S. Murakami, F. Bonell, T. Nozaki, T. Shinjo, and Y. Suzuki: *Appl. Phys. Express.*, **4**, 043005 (2011).
5) M. Tsujikawa, S. Haraguchi, T. Oda, Y. Miura, and M. Shirai: *J. Appl. Phys.*, **109**, 07C107 (2011).
6) X. W. Guan, X. M. Cheng, T. Huang, S. Wang, K. H. Xue, and X. S. Miao: *J. Appl. Phys.*, **119**, 133905 (2016).
7) Y. Shiota, T. Nozaki, F. Bonell, S. Murakami, T. Shinjo, and Y. Suzuki: *Nat. Mater.*, **11**, 39 (2012).
8) S. Iihama, S. Mizukami, H. Naganuma, M. Oogane, Y. Ando, and T. Miyazaki: *Phys. Rev. B*, **89**, 174416 (2014).
9) A. Okada, S. He, B. Gu, S. Kanai, A. Soumyanarayanan, S. T. Lim, M. Tran, M. Mori, S. Maekawa, F. Matsukura, H. Ohno, and C. Panagopoulos: *Prcc. Natl. Acad. Sci. USA*, **114**, 3815 (2017).
10) V. Kambersky: *Czech. J. Phys. B*, **26**, 1366 (1976).
11) T. Kato, K. Nakazawa, R. Komiya, N. Nishizawa, S. Tsunashima, and S. Iwata: *IEEE Trans. Magn.*, **44**, 3380 (2008).
12) T. Kato, Y. Matsumoto, S. Okamoto, N. Kikuchi, O. Kitakami, N. Nishizawa, S. Tsunashima, and S. Iwata: *IEEE Trans. Magn.*, **47**, 3036 (2011).
13) T. Kato, Y. Matsumoto, S. Kashima, S. Okamoto, N. Kikuchi, S. Iwata, O. Kitakami, and S. Tsunashima: *IEEE Trans. Magn.*, **48**, 3288 (2011).
14) M. Tsujikawa, S. Haraguchi, and T. Oda: *J. Appl. Phys.*, **111**, 083910 (2012).
15) H. Shul: *Phys. Rev.*, **97**, 555 (1955).
16) J. -M. Beaujour, D. Ravelosona, I. Tudosa, E. E. Fullerton, and A. D. Kent: *Phys. Rev. B*, **80**, 180415(R) (2009).
17) R. D. McMichael and P. Krivosik: *IEEE Trans. Magn.*, **40**, 2 (2004).
18) P. Landeros, R. E. Arias, and D. L. Mills: *Phys. Rev. B*, **77**, 214405 (2008).
19) S. Iihama, A. Sakuma, H. Naganuma, M. Oogane, S. Mizukami, and Y. Ando: *Phys. Rev. B*, 94, 174425 (2016).
20) T. Kato, D. Oshima, and S. Iwata, *Crystals*, **9**, 27 (2019).
21) A. J. P. Meyer, G. Asch: *J. Appl. Phys.*, **32**, 330S (1961).
22) J. M. Shaw, H. T. Nembach, and T. J. Silva: *Phys. Rev. B*, **87**, 054416 (2013).
23) J. M. Shaw, H. T. Nembach, T. J. Silva, and C. T. Boone: *J. Appl. Phys.*, **114**, 243906 (2013).
24) M. A. W. Schoen, D. Thonig, M. L. Schneider, T. J. Silva, H. T. Nembach, O. Eriksson, O. Karis, and J. M. Shaw: *Nat. Phys.*, **12**, 839 (2016).
25) J. Foros, G. Woltersdorf, B. Heinrich, and A. Brataas: *J. Appl. Phys.*, **97**, 10A714 (2005).
26) J. M. Shaw, H. T. Nembach, and T. J. Silva: *Phys. Rev. B*, **85**, 054412 (2012).
27) H. Kurt, W. -C. Chiang, C. Ritz, K. Eid, W. P. Pratt Jr., and J. Bass: *J. Appl. Phys.*, **93**, 7918 (2003).
28) A. Zambano, K. Eid, R. Loloee, W. P. Pratt Jr., and J. Bass: *J. Magn. Magn. Mat.*, **253**, 51 (2002).
29) M. Zwierzycki, Y. Tserkovnyak, P. J. Kelly, A. Brataas, and G. E. W. Bauer: *Phys. Rev. B*, **71**, 064420 (2005).
30) V. Kambersky: *Phys. Rev. B*, **76**, 134416 (2007).

Received Mar. 21, 2021; Accepted May 28, 2021

J. Magn. Soc. Jpn., **45**, 101-105 (2021)

<Paper>

Structural, Magnetic, and Electric Properties of Pt/Co/Au/Cr_2O_3/Pt Thin Film with Cr_2O_3 Layer below 25 nm

Yu Shiratsuchi,* Jiaqi Shen, Yiran Tao, Kohei Takahara, Kentaro Toyoki, and Ryoichi Nakatani
Graduate School of Engineering, Osaka University, *2-1 Yamadaoka, Suita, Osaka 565-0871, Japan*

Perpendicular exchange bias using magnetoelectric Cr_2O_3 has an electric-field triggered switching ability, and the thickness limit of the Cr_2O_3 layer for inducing this bias is a topic of research. In this paper, we investigated the structural, magnetic, and electric properties of Pt/Co/Au/Cr_2O_3/Pt thin films with a Cr_2O_3 layer in the thickness range of 5.7 to 25 nm. By using a magnetron sputtering method, a well-crystallized Cr_2O_3(0001) layer was formed in 5.7-nm-thick Cr_2O_3. All studied films showed perpendicular magnetic anisotropy. The uniaxial magnetic anisotropy energy density increased as the Cr_2O_3 thickness decreased, and 810±90 kJ/m^3 was obtained for the film with 5.7-nm-thick Cr_2O_3. Perpendicular exchange bias was evaluated above 80 K, and an exchange anisotropy energy density of 0.30 mJ/m^2 was observed for the film with a 25-nm-thick Cr_2O_3 at 80 K. The exchange bias could not be observed below 18 nm. Instead, coercivity enhancement, which yields the exchange bias by precisely controlling interfacial exchange coupling, was observed. The electric resistivity was about 5×10^5 Ω·m for the 5.7-nm-thick Cr_2O_3 layer, which is sufficiently high for magnetoelectric applications.

Keywords: Cr_2O_3, antiferromagnet, thin film, perpendicular magnetic anisotropy, insulator

1. Introduction

Future memory/logic devices beyond CMOS require several severe working conditions such as low-energy operation below 10 atto-J (aJ) and fast switching below 1 ns [1]. The magnetoelectric (ME) effect, which results from coupling between magnetic and electric fields, can be a solution for creating low energy input methods for these devices. The ME effect is recognized as the effect of spontaneous magnetization (M) induction by an electric field (E) or electric polarization (P) induction by a magnetic field (H) [2,3]. The strength of the ME effect is characterized by using ME susceptibility as follows.

$$\alpha_{ij} = dM_i/dE_j = dP_i/dH_j \quad (1)$$

The ME effect is sometimes observed in antiferromagnetic (AFM) insulators where α_{ij} is coupled with an AFM order parameter [4]. Eventually, the sign of α_{ij} is reversed and accompanied with the reversal of the Néel vector. The driving force of the reversal is expressed by [4]

$$2\alpha_{ji}E_iH_j, \quad (2)$$

which is reminiscent of the Zeeman energy of ferromagnetic (FM) materials in that the spontaneous magnetization of the FM layer is replaced with the E-induced magnetization $\alpha_{ij}E_i$.

Cr_2O_3 is a well-known ME-AFM insulator, and the above-mentioned reversal of α_{ij} was first detected by directly measuring α_{ij} for bulk Cr_2O_3 [4]. Although Cr_2O_3 is a proto-typical ME-AFM material, it has advantages compared with other single-phase multiferroic materials, such as simple preparation based on a conventional sputtering technique and a sole cation species that can prevent the crystalline quality from being deteriorated by the incorrect site occupation of other cations. Despite these advantages, the application of the ME effect in Cr_2O_3 has been regarded as difficult because the ME effect for Cr_2O_3 is a linear effect; the ferroic feature vanishes by removing E or H [2,3,5]. In 2005, Borisov *et al.* complemented the linear ME effect by using an exchange bias [6]. In this scheme, the interfacial AFM spin/domain state, which is coupled with an AFM order parameter (the Néel vector), is detected by exchange bias polarity. When the AFM spin/domain state (the Néel vector) is reversed by the ME effect, this reversal is accompanied with a change in the exchange bias polarity. In particular, when the exchange bias field is higher than the coercivity, the magnetization direction of the FM layer after the field is removed reverses definitely. This scheme has been experimentally proven using the FM/Cr_2O_3(0001) thin film system [7,8].

The above device scheme is designed upon the prerequisite that the film has a perpendicular exchange bias higher than the coercivity, and hence, the lowest Cr_2O_3 thickness at which perpendicular exchange bias can be induced would determine the low thickness limit of the device. According to the magnetic domain wall (DW) model [9,10], the critical AFM layer thickness for inducing exchange bias is relevant to the DW width of the AFM layer along the film thickness direction. For the case of Cr_2O_3(0001) thin film, the DW width along the c-axis was calculated in the range of 20-70 nm depending on the lattice parameter [11]. Recently, ME-induced switching of the perpendicular exchange bias was demonstrated using 30-nm-thick Cr_2O_3(0001) thin film [12], and perpendicular exchange bias using a Cr_2O_3(0001)

Corresponding author: Y. Shiratsuchi (e-mail: shiratsuchi@mat.eng.osaka-u.ac.jp).

layer was confirmed for film with 20-nm-thick Cr_2O_3 [13]; for both cases, the Cr_2O_3 thickness was near the DW width. In this paper, we explored the possibility of the perpendicular exchange bias persisting below the 20-nm-thick Cr_2O_3(0001) layer as well as the electric properties that are also important for electric field application.

2. Experimental methods

The stacking structure of the fabricated sample was a Pt(2 nm)/Co(0.5 nm)/Au(0.5 nm)/Cr_2O_3(t_{Cr2O3} = 5.7, 12, 18, 25 nm)/Pt(20 nm)/α-Al_2O_3(0001) substrate. The thicknesses of the Co and Au layer were in a few monolayer regime, and these were the nominal thicknesses. The Au space layer was used to tune the interfacial exchange coupling strength between the Co and Cr_2O_3 so that the coercivity enhancement could be suppressed when the exchange bias was manifested [14]. The substrate was ultrasonically cleaned using acetone, ethanol, pure water, and isopropanol. Each layer was deposited by using a DC magnetron sputtering method. The Pt, Co, and Au layers were deposited using pure Ar, and the Cr_2O_3 layer was deposited by using a reactive sputtering method with a gas mixture of Ar and O_2. Before the deposition, the substrate was degassed at 873 K and, subsequently, the Pt buffer layer was deposited at 873 K. The deposition temperature of the Cr_2O_3 layer was 773 K. The Pt capping layer, Co, and Au layers were deposited at room temperature.

Structural characterizations were carried out using reflection high-energy electron diffraction (RHEED), X-ray reflectometry (XRR), and high-angle X-ray diffraction (XRD). For the RHEED observations, the sample was once cooled down to room temperature after the deposition and transferred to a RHEED chamber that was directly connected to the deposition chamber through an ultra-high vacuum gate valve. The XRR and XRD measurements were carried out using Cu $K\alpha$ irradiation with a Ge (220) × 2 monochromator.

Magnetic properties were characterized on the basis of magnetization curves measured using a vibrating-sample magnetometer (VSM) and magneto-optic Kerr effect (MOKE) measurements. The VSM measurements were done at room temperature (~300 K) for the applied magnetic field direction parallel and perpendicular to the film plane. MOKE loops were measured with a polar configuration where the incident angle of light (λ = 670 nm) was 10° from the surface normal. The MOKE measurements were carried out in a temperature regime from 80 K to 300 K.

3. Results and discussions

3.1 Structural characterizations

Figure 1 shows RHEED images of the 5.7-nm-thick Cr_2O_3 layer, which was the lowest case in this paper. For both electron azimuths, equally spaced streaks were observed, which indicate the flat surface and aligned

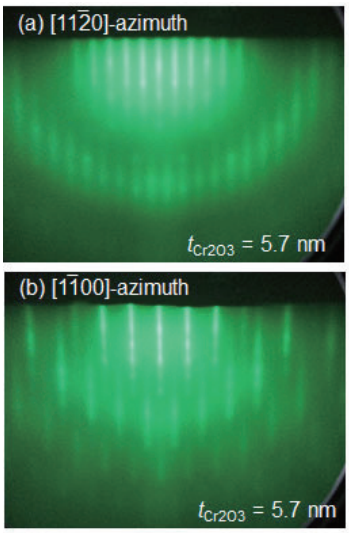

Fig. 1 RHEED images for 5.7-nm-thick Cr_2O_3 layer. Electron azimuth was (a) [11$\bar{2}$0] and (b) [1$\bar{1}$00] of α-Al_2O_3(0001) substrate.

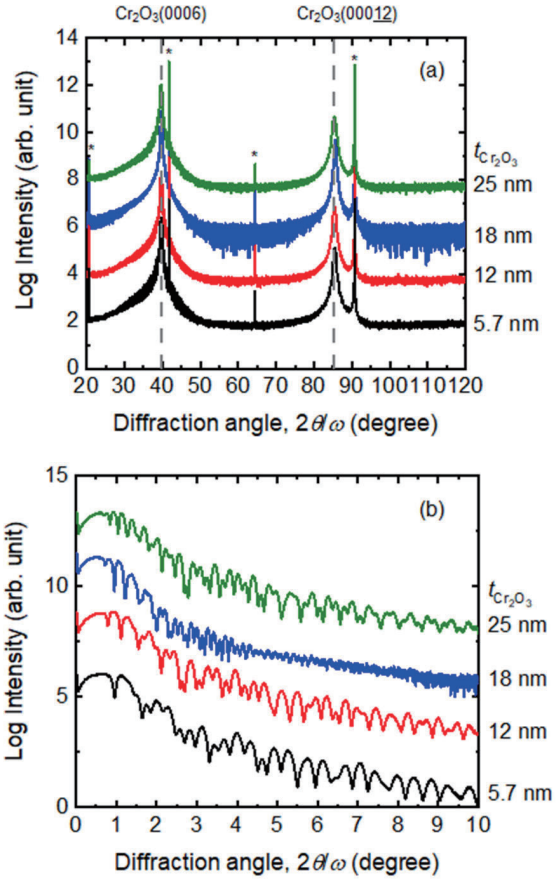

Fig. 2 (a) High-angle XRD profiles and (b) XRR profiles for films with different t_{Cr2O3}. * in (a) represents diffraction from substrate. Dotted gray line shows guide line for diffraction peak position of Pt(111) and Pt(222) calculated using bulk lattice parameter.

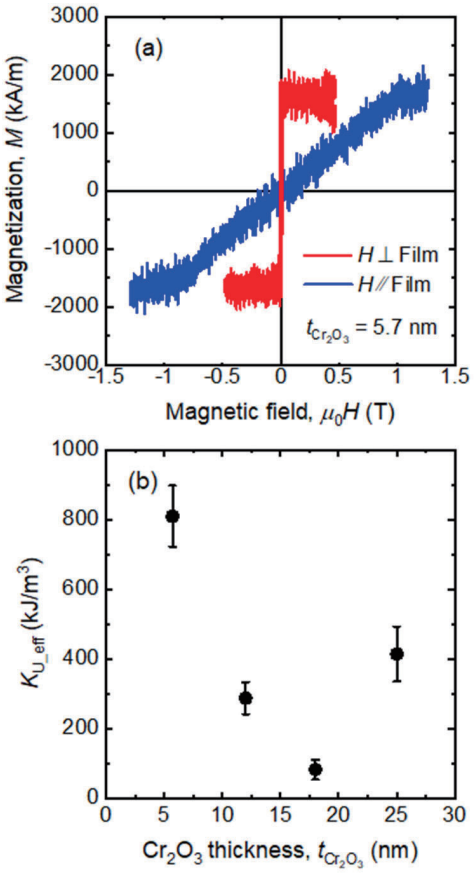

Fig. 3 (a) Magnetization curves for film with t_{Cr2O3} = 5.7 nm. Red and blue curves represent curves for applied magnetic field direction perpendicular and parallel to film plane, respectively. (b) Change in K_{U_eff} with t_{Cr2O3} evaluated from magnetization curves.

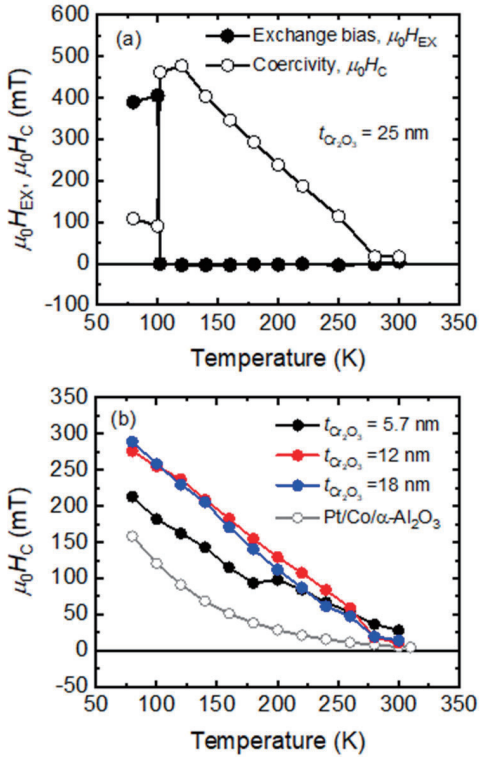

Fig. 4 (a) Temperature dependence of $\mu_0 H_{EX}$ and $\mu_0 H_C$ for film with t_{Cr2O3} = 25 nm. (b) Temperature dependence of $\mu_0 H_C$ for films with t_{Cr2O3} = 18 nm (blue), 12 nm (red), and 5.7 nm (black). Magnetization curves for film with t_{Cr2O3} = 5.7 nm. Open gray circles are $\mu_0 H_C$ for reference film, Pt/Co bilayer on α-Al_2O_3(0001) substrate.

crystallographic orientation in the growth direction. The diffraction patterns can be explained by the corundum (0001). In addition, the symmetric pattern in the [11$\bar{2}$0]-azimuthal RHEED pattern indicates twin formation with a twin boundary along [11$\bar{2}$0]. Similar RHEED patterns were observed for every t_{Cr2O3}. In our previous reports [14], the Au layer grown on the Cr_2O_3(0001) layer was poly-crystalline, and the subsequent Co and Pt layer showed a weak (111) orientation. We confirmed a similar structure for the films studied in this paper. Figure 2(a) shows high-angle XRD profiles wherein the diffraction peaks were near 2θ = 40° and 85° except for the diffractions from the substrate (indicated by *). The former and latter diffraction peaks originated from Pt(111) [or Cr_2O_3(0006)] and Pt(222) [or Cr_2O_3(00012)], respectively, which was consistent with the RHEED observations. Because the *d*-spacings for Pt(*l l l*) and Cr_2O_3(000*l*) were almost same, it was difficult to distinguish these two in the XRD profiles. Nonetheless, the peak intensity was almost independent of t_{Cr2O3}, and thus, we believe that the diffraction was mainly from the Pt buffer layer. This should be reasonable because the atomic scattering factor of Pt is higher than those of Cr^{3+} and O^{2-}.

For qualitative discussion on the interfacial magnetic properties shown below, we indirectly evaluated interface roughness on the basis of XRR measurements. Figure 2(b) shows XRR profiles of the fabricated films. The profiles show clear oscillation up to 2θ = 10° except for the film with t_{Cr2O3} = 18 nm, where the oscillation disappeared at about 2θ = 4°. The results indicate that films except for that with t_{Cr2O3} = 18 nm had a sharp interface, and that with t_{Cr2O3} = 18 nm was relatively rough. The theoretical fitting implies that the interface roughness at the FM(Pt/Co/Au)/Cr_2O_3 interface was about 0.3 nm for the former three films and about 0.8 nm for the film with t_{Cr2O3} = 18 nm.

3.2 Magnetic properties

Figure 3 shows magnetization curves (*M*-*H* curves) measured at room temperature for the film with t_{Cr2O3} = 5.7 nm. The saturation magnetization was about 1600 kA/m, which was higher than the value for the bulk Co (~1400 kA/m) possibly because of the sizable spin

polarization of Pt (and Au) [15,16]. The M-H curve with H perpendicular to the film plane showed a rectangular hysteresis with the remanence ratio of unity. In contrast, the M-H loop with H parallel to the film plane was almost linear below $\mu_0 H$ at about 1 T, and no clear hysteresis was observed. The results show that the film showed perpendicular magnetic anisotropy. The uniaxial magnetic anisotropy energy density K_{U_eff} was evaluated using

$$K_{U\_eff} = \left(\int_0^{M_S} HdM \right)_{H//Film} - \left(\int_0^{M_S} HdM \right)_{H\perp Film}, \quad (3)$$

where M_S denotes the saturation magnetization. In Fig. 3(b), the change in K_{U_eff} with t_{Cr2O3} is shown. K_{U_eff} is typically within several 100 kJ/m^3. The dispersion of the values may be due to the difference in the micro-structure of the Co layer because the Co thickness was in a few monolayer regime. The reduction in K_{U_eff} for the film with t_{Cr2O3} = 18 nm should be due to the large roughness mentioned above.

Figure 4(a) shows the temperature dependence of the exchange bias field ($\mu_0 H_{EX}$) and the coercivity ($\mu_0 H_C$) for the film with t_{Cr2O3} = 25 nm measured on the basis of polar MOKE. An exchange bias field of $\mu_0 H_{EX}$ = 390 mT was observed at 80 K and increased to 410 mT at 100 K. The increase in $\mu_0 H_{EX}$ as temperature increased is attributed to interfacial Cr^{3+} spin canting [17]. The exchange bias abruptly disappeared at 102 K, and the coercivity was enhanced, accompanied with a disappearance of the exchange bias. This abrupt disappearance was observed for the FM/Cr_2O_3(0001) stacked film [13,18] and is likely to be a unique feature of this system. Details on this unique temperature dependence can be found in our previous review [19]. Below a t_{Cr2O3} of 18 nm, the exchange bias could not be observed above 80 K. In Fig. 4(b), the temperature dependence of $\mu_0 H_C$ for the films with t_{Cr2O3} below 18 nm are shown. The $\mu_0 H_C$ (open gray circle) for the Pt/Co bilayer on the α-Al_2O_3(0001) substrate is also shown as a reference. As in the case of t_{Cr2O3} = 25 nm above 102 K, the coercivity increased as the temperature decreased. Although a direct comparison of the absolute value of coercivity is difficult because coercivity can be affected by structural defects and micro-structures, it is likely that the $\mu_0 H_C$ values at 300 K were similar for the Pt/Co/Au/Cr_2O_3/Pt films and the reference sample (Pt/Co bilayer on the α-Al_2O_3 substrate).

Below 280 K (~Néel temperature of Cr_2O_3 thin film [20]), the coercivity of the Pt/Co/Au/Cr_2O_3/Pt films seemed to be enhanced compared with the reference sample, and this enhancement was observed for the film with t_{Cr2O3} = 5.7 nm.

As previously discussed, the onset temperature of the exchange bias in the FM/Cr_2O_3 system can be controlled by the spacer layer thickness [14,21], i.e., the strength of the interfacial exchange coupling. Hence, when we precisely control the interfacial exchange coupling, it is expected that exchange bias might be achieved for a low t_{Cr2O3} below 18 nm. That is, in this work, the Au spacer thickness was fixed at 0.5 nm. If a little thicker, the Au spacer layer would reduce the interfacial exchange coupling, which would yield the perpendicular exchange bias in the high temperature regime. In comparison, a thicker Au layer would also reduce the exchange bias field. To realize this, very precise control of the Au spacer thickness is necessary; this is future work.

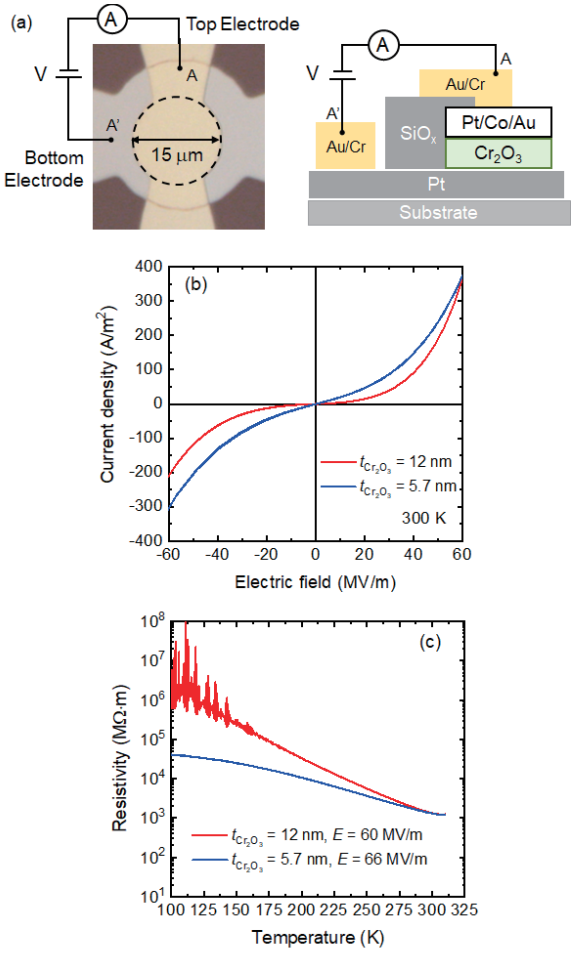

Fig. 5 (a) Optical microscope image of devices used for electric characterizations. Electric circuit is also drawn. Right image is schematic drawing of cross-section of device. (b) I-V curve and (c) temperature dependence of resistivity for films with t_{Cr2O3} = 12 (red) and 5.7 (blue) nm.

3.3 Electric properties

For electric-field triggered switching including the ME-based mechanism, sufficient resistivity is also essential. In most previous reports on ME-induced switching of the perpendicular exchange bias using Cr_2O_3 thin film, thick Cr_2O_3 above 100 nm was often used [7,8,22], although, very recently, we reported a scheme using Cr_2O_3 thin film below 50 nm [12,23]. There are few reports on the insulating properties of the Cr_2O_3 layer in the thickness regime below 30 nm. To investigate the electric properties, the micro-dot with a 30-μm diameter shown in Fig. 5(a) was fabricated by photolithography, Ar ion milling, and a lift-off technique. Using this device, I-V curves and the temperature dependence of the resistivity were measured on the basis of a two-terminal method. Figure 5(b) shows an I-V curve

measured at 300 K. For both films with t_{Cr2O3} = 12 and 5.7 nm, the *I*-*V* curves showed a non-linear increase, which indicates that the device had an insulating feature. The asymmetry in the *I*-*V* curves should be due to the different materials of the top (Pt/Co/Au) and bottom (Pt) electrodes. As shown in Fig. 5(c), the resistivity increased as temperature decreased in an exponential manner, which also supports the insulating feature of the fabricated Cr_2O_3 layer. The resistivity, evaluated by the derivative of the *I*-*V* curve [Fig. 5(b)], was about 3×10^6 Ω·m and 5×10^5 Ω·m for the films with t_{Cr2O3} = 12 and 5.7 nm, respectively. These values are similar to the reported resistivity for 300-nm-thick Cr_2O_3 [24]. In addition, the leakage current density at E = +60 MV/m was about 300 A/m^2, which is similar to the case of the 30-nm-thick Cr_2O_3 film where ME-induced switching of the exchange bias was confirmed [12]. That is, the resistivity was sufficiently high enough to apply the scheme to the ME-induced switching of perpendicular exchange bias.

4. Summary

We investigated the structural, magnetic, and electric properties of Pt/Co/Au/Cr_2O_3/Pt thin films with a Cr_2O_3 thickness below 25 nm. Well-crystallized Cr_2O_3 thin film could be prepared in a 5.7-nm thickness by using a reactive magnetron sputtering method. The film showed perpendicular magnetic anisotropy at room temperature. The uniaxial magnetic anisotropy energy density is typically on the order of several 100 kJ/m^3. Perpendicular exchange bias, evaluated above 80 K, was observed for a film with t_{Cr2O3} = 25 nm. Although below 18 nm, the bias was not observed above 80 K, a comparison with a Pt/Co bilayer on an α-Al_2O_3 substrate suggested a coercivity enhancement. Hence, the exchange bias is expected to appear through the precise control of the interfacial exchange coupling strength. An insulating feature was maintained for the 5.7-nm-thick Cr_2O_3 layer, and the resistivity was about 5 MΩ·m, which is comparable to the reported value for thick film above 30 nm and is sufficiently high enough to apply the ME-induced switching device scheme.

Acknowledgements This work was partly supported by JSPS KAKENHI (Grant No. 19H000825) and the Photonics Advanced Research Center (PARC) at Osaka University.

References

1) S. Maniparruni, D. E. Nikonov, and I. A. Young: *Nature Physics*, **14**, 338 (2018).
2) D. N. Astrov: *Sov. Phys. JETP*, **11**, 708 (1960).
3) V. J. Folen, G. T. Rado, and E. W. Stalder: *Phys. Rev. Lett.*, **6**, 607 (1061).
4) T. J. Martin and J. C. Anderson: *IEEE Trans. Magn.*, **2**, 446 (1966).
5) A. Iyama and T. Kimura: *Phys. Rev. B*, **87**, 180408(R) (2013).
6) P. Borisov, A. Hochstrat, C. Chen, W. Kleeman, and Ch. Binek: *Phys. Rev. Lett.*, **94**, 117203 (2005).
7) T. Ashida, M. Oida, M. Shimomura, T. Nozaki, T. Shibata, and M. Sahashi: *Appl. Phys. Lett.*, **104**, 152409 (2014).
8) K. Toyoki, Y. Shiratsuchi, A. Kobane, S. Yoshida, and R. Nakatani: *Appl. Phys. Express*, **13**, 043003 (2014).
9) D. Mauri, H. C. Siegmann, P. S. Bagus, and E. Kay: *J. Appl. Phys.*, **62**, 3047 (1987).
10) C. Mitsumata, A. Sakuma, K. Fukamichi, M. Tsunoda, and M. Takahashi: *J. Phys. Soc. Jpn.*, **77**, 044602 (2008).
11) Y. Kota and H. Imamura: *Appl. Phys. Express*, **10**, 013002 (2017).
12) Y. Shiratsuchi, Y. Tao, K. Toyoki, and R. Nakatani: *Magnetochemistry*, **7**, 26 (2021).
13) Y. Shiratsuchi, D. Tokunaga, and R. Nakatani: *Jpn. J. Appl. Phys.*, **59**, SEEF02 (2020).
14) Y. Shiratsuchi, W. Kuroda, T. V. A. Nguyen, Y. Kotani, K. Toyoki, T. Nakamura, M. Suzuki, K. Nakamura, and R. Nakatani: *J. Appl. Phys.*, **121**, 073902 (2017).
15) F. Wilhelm, M. Anglekreis, N. Jaouen, P. Poulopoulos, E. Th. Papaioannour, Ch. Mueller, P. Fumagalli, A. Rogalev, and N. K. Flevaris: *Phys. Rev. B*, **69**, 220404(R) (2004).
16) M. Suzuki, H. Muraoka, Y. Inaba, H. Miyagawa, N. Kawamura, T. Shimatsu, H. Maruyama, N. Ishimatsu, Y. Isohara, and Y. Sonobe: *Phys. Rev. B*, **72**, 054430 (2005).
17) X. He, Y. Wang, N. Wu, A. N. Caruso, E. Bescovo, K. D. Belashchenko, P. A. Dowben, and C. Binek: *Nature Materials*, **9**, 579 (2010) and supplementary information.
18) Y. Shiratsuchi, T. Fujita, H. Oikawa, H. Noutomi, and R Nakatani: *Appl. Phys. Express*, **3**, 113001 (2010).
19) Y. Shiratsuchi and R. Nakatani: *Mater. Trans.*, **57**, 781 (2016).
20) T. Iino, T. Moriyama, H. Iwaki, H. Aono, Y. Shiratsuchi, and T. Ono: *Appl. Phys. Lett.*, **114**, 022402 (2019).
21) Y. Shiratsuchi, T. Fujita, H. Noutomi, H. Oikawa, and R. Nakatani: *IEEE Trans. Magn.*, **47**, 3909 (2011).
22) Y. Hui, W. Lin, Q. Xie, S. Chen, X. Miao, and J. Chen: *J. Phys. D; Appl. Phys.*, **52**, 24LT03 (2019).
23) Y. Shiratsuchi, K. Toyoki, Y. Tao, and R. Nakatani: *Appl. Phys. Express*, **13**, 043003 (2020).
24) A. Mahmood, M. Street, W. Echtenkamp, C. P. Kwan, J. P, Bird, and C. Binek: *Phys. Rev. Mater.*, **2**, 044401 (2018).

Received Apr. 13, 2021; Accepted May 11, 2021.

J. Magn. Soc. Jpn., **45**, 106-111 (2021)

<Paper>

Iron Loss Evaluation in Consideration of Anomalous Loss for PAM Inverter Excitation in Finite Element Analysis

Kenya Naruse [1], Keisuke Fujisaki [1], and Nguyen Gia Minh Thao [1,2]

[1] Electromagnetic Energy Systems Laboratory, Toyota Technological Institute, Nagoya 468-8511, Japan

[2] Department of Aerospace Engineering, Graduate School of Engineering, Nagoya University, Nagoya 464-8603, Japan

This paper presents a model efficiently considering the anomalous loss as post-processing after the finite element analysis (FEA), and it is applied to the inverter excitation evaluation, especially the pulse-amplitude-modulation (PAM) inverter. The effectiveness of the designed FEA model is validated by non-oriented (NO) ring core experiments. The calculation result can express the iron loss obtained in experiments well. A new pulse pattern of the PAM excitation method is evaluated under two operating conditions. Under the first condition with the fixed maximum magnetic flux density B_{max} considered as the conventional material evaluation, the iron loss with the PAM inverter excitation is smaller than that with the PWM inverter and sinusoidal excitations, and has the smallest value at the excitation angle of 165° in the PAM excitation. On the other hand, under the second condition with a fixed fundamental component value of the magnetic flux density B_{f0}, the iron loss becomes smaller in the order of the PWM, sinusoidal and PAM excitations, which heavily depends on magnitudes of the time harmonics of the flux density; the result obtained in this case has a different tendency with that in the first case where the B_{max} is fixed.

Key words: Iron loss, anomalous loss, magnetic field analysis, finite element method, PAM inverter excitation.

Nomenclature

H	Magnetic field intensity
B	Flux density
B_{max}	Maximum flux density
f	Frequency
f_0	Fundamental frequency
N_1	The number of turns of primary coil
N_2	The number of turns of secondary coil
l	Average magnetic path length
S	Cross section area of ring core
ρ	Steel plate density
I_1	Primary input current in measurement
V_2	Secondary open-circuit voltage
n	Element number
σ	Conductivity of steel plate
κ	Anomaly factor
$j_{xn}(t)$	Classical eddy current density
$J_{xn}(f)$	Fourier transform of $j_{xn}(t)$
W_{fe}	Iron loss
$W_{e,c}$	Classical eddy current loss
$W_{e,a}$	Anomalous loss
W_{hys}	Hysteresis loss

1. Introduction

With the large demand of electrical power conversion for the realization of electric vehicles (EVs) and advanced society, progresses of power electronics technology such as inverters are increasing year by year. A high-efficient motor drive system for EVs is a typical example. With the recent power electronics technology, the voltage and frequency can be flexibly and quickly controlled by the switching operation of power semiconductors used in a power electronics circuit, and the magnetic material in it is also excited at the same time. Due to the rectangular waveform of the voltage in the circuit, the power electronics excitation may lead to an increase of the iron loss generated in the magnetic material [1),2)]. Therefore, the reduction of the iron loss in the power electronics excitation is a crucial issue, which should be appropriately examined and resolved for EVs and the environment-friendly society.

With the power electronics technology, an optional pulse pattern of the output voltage can be generated and modified; it is also considered as a crucial issue to be studied and discussed on which pulse pattern is more efficient to reduce the iron loss. Hence, a new pulse pattern in the pulse-amplitude modulation (PAM) excitation method is investigated here for the reduction of the iron loss due to its simple excitation [3)-5)], although the pulse-width modulation (PWM) excitation is often utilized.

To evaluate the iron loss characteristics, the numerical calculation as finite element method (FEM) of electromagnetic field is a useful method for the design and development of the inverter excitation or motor drive systems. The calculation of the hysteresis loss is improved due to analytical methods that consider the hysteresis properties of magnetic materials [6),7)], and the classical eddy current loss can be obtained from the Maxwell equations. However, the anomalous loss cannot be easily obtained. It is necessary to consider the microscopic phenomenon derived from the magnetic domain wall motion, so that it is not possible to determine the anomalous loss with a macro model such as an electrical motor. A well-known method for calculating the anomalous loss was proposed by Bertotti [8)]; however, we develop a simpler method for efficiently

Corresponding author: K. Fujisaki (e-mail: fujisaki@toyota-ti.ac.jp).

obtaining the anomalous loss in this study. Furthermore, the macro-sized calculation usually uses the finite element analysis (FEA).

Therefore, in this paper, the FEA carefully taking account of the anomalous loss in the conventional magnetic field analysis is studied and applied to the macro-model separately excited by the PAM inverter, PWM inverter and sinusoidal excitation methods. In particular, the detailed investigation of the iron loss characteristics in a ring core under the PAM inverter excitation method with different excitation angles is one of the key uniqueness and contributions of this research. The simulation results with the proposed FEA model are also validated by comparison with the measured iron loss data of the ring core obtained in experiments. Moreover, physics-based insights and explanations on the obtained results are provided.

2. Finite Element Analysis

Because of the difficulty in direct analysis and calculation of the magnetic field movement in an electrical motor core, the anomalous loss can be investigated with a post-processing technique after the FEA of electrical apparatus. It is important to possibly consider and cope with the inverter excitation case that includes a lot of harmonic components of eddy currents.

2.1 Finite Element Analysis Model

Magnetic hysteresis characteristics are investigated with a play-model in the FEA [7]. The B-H curve used in FEM calculation is introduced from the measured data to be considered to DC characteristics [9]. A cut-out part of an actual ring core is used as a FEA model as shown in Fig. 1. The upper figure is a schematic view of the actual ring core whose characteristics are given in Table 1. The lower figure is a model, that is used in the analysis, is an enlarged version of the upper figure. While the actual ring core has 20 laminated layers, this model has only one layer of the electrical steel with electrical insulation coating due to the symmetry in the laminating direction (y-direction). Furthermore, the designed model is a rectangular parallelepiped by dividing the circumferential direction (z-direction) into 5000 along the average magnetic path length. A steel sheet is magnetized by applying a current in y-direction determined by an external circuit as a natural boundary condition to both ends. Therefore, the electromotive force is introduced in the steel in y-direction though the eddy current flows in x-direction at the surface of the steel owing to the electrical insulation. The introduced current causes a magnetic flux to flow in z-direction. In the case where the inverter excitation is utilized, the ON voltage of the semiconductor should be considered [10]. The FEA results introduce the time series of the flux density and eddy current at each element of the considered NO material.

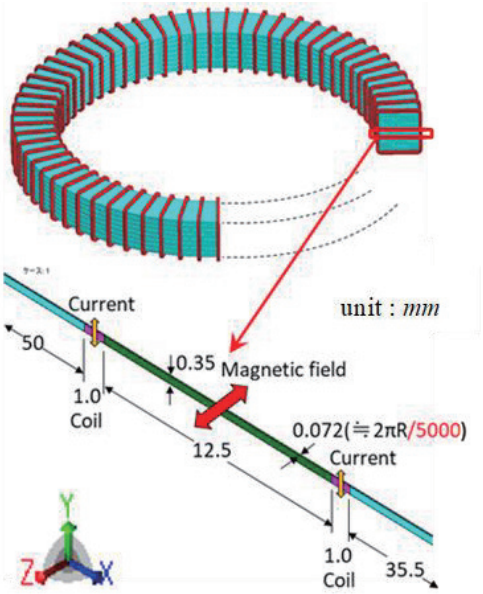

Fig. 1. Symmetrical 2-D FEM ring model.

Table 1. Ring core characteristics

Steel plate material	NO (35H300)
Primary coil N_1	254 turns
Secondary coil N_2	254 turns
Average magnetic path length l	0.36 m
Cross section area of ring core S	87.5 mm^2
Steel plate density ρ	7650 kg/m^3
Conductivity of steel plate σ	1.92 MS/m
Inner diameter	46.5 mm
Outer diameter	67.5 mm
Hight of ring core	15.5 mm

2.2 Iron Loss Calculation for Analysis

The central part of the NO steel in the width of 12.5 mm is picked up for evaluation. The calculated eddy current $j_{xn}(t)$ at element number n is called the classical eddy current, not the abnormal one. Therefore, the classical eddy current loss $W_{e,c}$ is calculated as below.

$$W_{e,c} = \frac{1}{\rho n}\sum_{n}\frac{j_{xn}(t)^2}{\sigma} \tag{1}$$

The classical eddy current loss $W_{e,a}$ and the anomalous loss $W_{e,a}$ have a relation by the introduction of an anomaly factor κ [11] as expressed in (2).

$$\kappa = \frac{W_{e,c} + W_{e,a}}{W_{e,c}} \tag{2}$$

It is necessary to identify an anomaly factor κ for each material since the generation of abnormal eddy current depends on the magnetic domain structure. The anomaly factor κ of this steel sheet was measured by another work [12] as depicted in Fig. 2, where κ has a parameter of frequency. Therefore, by means of Fourier transform of $j_{xn}(t)$ to $J_{xn}(f)$, the anomalous loss is calculated by the

following equation.

$$W_{e,a} = \frac{1}{\rho n}\sum_{n}\sum_{f}(\kappa(f)-1)\frac{J_{xn}(f)^2}{\sigma} \tag{3}$$

Due to the consideration of the magnetic hysteresis curve with the play model, the inner area of B-H curve at each element n is a sum of the magnetic hysteresis loss and classical eddy current loss. Since the analysis does not take into account anomalous eddy currents, anomalous loss is not included. Hence, the hysteresis loss can be calculated by

$$W_{hys} = \frac{f_0}{\rho n}\sum_{n}\int H\,dB_n - W_{e,c} \tag{4}$$

Finally, the total iron loss of the ring core, which consists of the hysteresis loss, classical eddy current loss and anomalous loss, is computed as follows.

$$W_{fe} = W_{e,c} + W_{e,a} + W_{hys} \tag{5}$$

3. Measurement Method

To evaluate effectiveness of the designed FEA model in careful consideration of the anomalous loss, the measurement of iron loss is also carried out in experiments. Both the PAM and PWM inverter excitations are performed. In this research, all the inverter and sinusoidal excitation methods are conducted for the same NO ring core as will be presented in Section 4.

3.1 Measurement System

The outline of the measurement system is shown in Fig. 3. A single-phase inverter unit equipped with the IGBT module (named PM75RSd060) is utilized for the inverter excitation, where the DC-bus voltage V_{DC} can be fixed or changed manually. On the other hand, a function generator connected with a linear amplifier is used for the sinusoidal excitation method. The primary input current I_1 and secondary open-circuit voltage V_2 are measured by a hall-effect current probe, differential voltage probe and analog-to-digital (AD) converter with a sampling rate of 50 MS/s and resolution of 14 bits. After that, the measured data is collected and processed in a personal computer by using MATLAB software.

3.2 Iron Loss Measurement

The iron loss is calculated from the measured primary input current I_1 and secondary open-circuit voltage V_2 of the ring core. The magnetic field strength H and the flux density B are calculated by (6) and (7), respectively; after that, the iron loss of the ring core W_{fe} is computed by (8).

$$H = \frac{N_1 I_1}{l} \tag{6}$$

$$B = \frac{1}{N_2 S}\int V_2\,dt \tag{7}$$

$$W_{fe} = \frac{f_0}{\rho}\int H\,dB \tag{8}$$

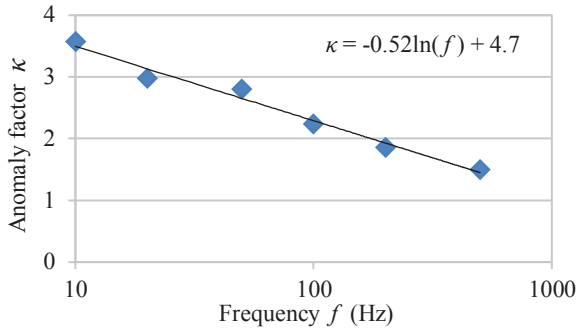

Fig. 2. Frequency characteristics of anomaly factor [12].

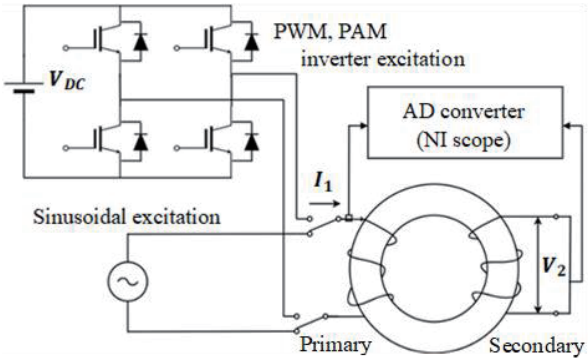

Fig. 3. Outline of the measurement system.

4. Excitation Methods for Ring Test

In this paper, three different excitation methods such as the PAM inverter, PWM inverter and sinusoidal excitations are used, where the fundamental frequency is fixed on f_0 = 50 Hz. The sinusoidal excitation is officially used for evaluation of magnetic materials according to the Japanese Industry Standard (JIS) and the International Electrotechnical Commission (IEC). The PWM excitation is usually used for motor drive systems in EVs; hence, conditions of the variable voltage and frequency should be carefully examined to efficiently lower the harmonics components. The PAM inverter excitation is newly evaluated for the iron loss characteristics. The input voltage V_{DC} of the inverter is changed to obtain the desired flux density conditions.

4.1 Sinusoidal Excitation

The sinusoidal voltage waveform is depicted in Fig. 4.

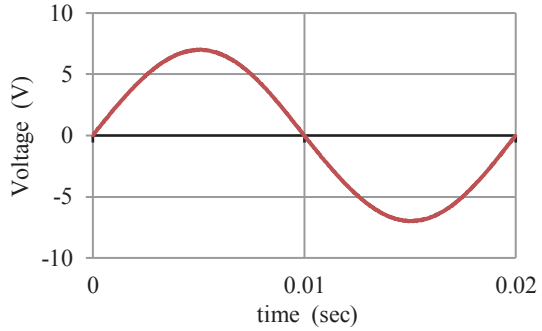

Fig. 4. Sinusoidal voltage waveform for excitation.

4.2 PWM Excitation

The carrier frequency is 1 kHz, and modulation index is 0.5. Only one period is conducted for reference. Fig. 5 shows the voltage waveform excited by the PWM inverter.

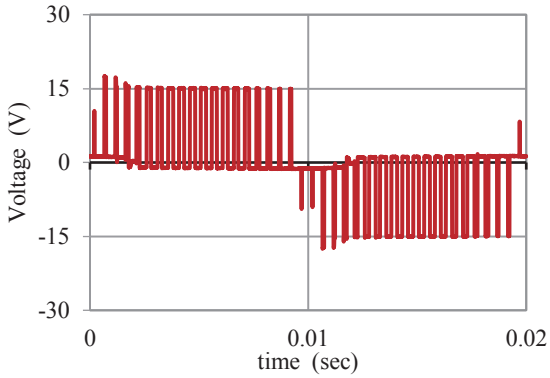

Fig. 5. PWM inverter excitation voltage waveform.

4.3 PAM Excitation

The PAM excitation voltage waveform is shown in Fig.6.

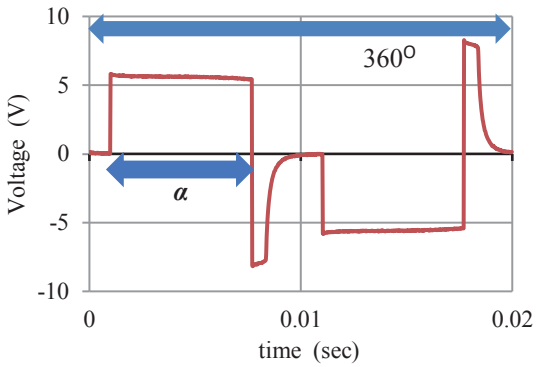

Fig. 6. Voltage waveform with PAM excitation ($\alpha = 120^{o}$).

The excitation angle α for the PAM-based inverter was often only set as 120^{o} or 180^{o}. In this research, five different values of the excitation angle such as $\alpha = 120^{o}$, 135^{o}, 150^{o}, 165^{o}, and 180^{o} are set and evaluated in the ring core test.

5. Measured and Simulation Results

The fixed value condition of the maximum flux density is usually used for the evaluation of magnetic materials because the flux density makes an electromagnetic torque. However, only a fundamental component of the flux density is said to be contributed to the torque of electrical motors, not harmonics components. The fixed maximum flux density condition and the fixed fundamental component condition of the flux density are often different especially in the inverter excitation method.

Therefore, two different types of the excitation condition are conducted and examined for the careful evaluation in this study. The first condition is to keep the maximum flux density B_{max} to be fixed, which is performed in both the analysis and experiment. Besides, the second condition is to keep the fundamental frequency component of the flux density B_{f0} to be fixed, which is only performed in experiments.

5.1 Fixed maximum flux density $B_{\max}$

The B-H curves obtained from measurements and the FEA with the designed play-model under the PAM inverter method with the excitation angle of 120^{o} are shown in Fig. 7. The red line is the measured result in experiments, and the blue line is the analysis one in simulation. We can see that the hysteresis model can be considered in the FEA, and the two shapes match well. The coercivity of the B-H curve obtained in the FEA is reduced slightly because of the ignorance of the abnormal eddy current for the FEA.

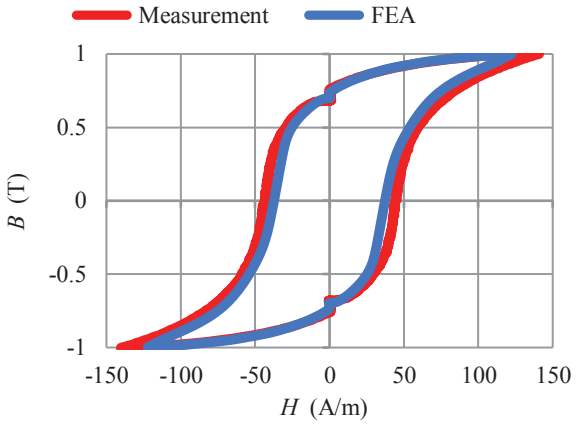

Fig. 7. B-H curve at 120^{o} of PAM inverter excitation.

In the loss calculation after the FEM analysis, classical eddy current is mainly used to equation (1), (3). So, the time-series of classical eddy current density on the outermost surface of the steel sheet is shown in Fig. 8. Then, Fig. 9 shows the frequency spectrum regarding Fig. 8. The odd-order harmonics can be confirmed, and the anomalous loss $W_{e,a}$ is calculated by equation (3).

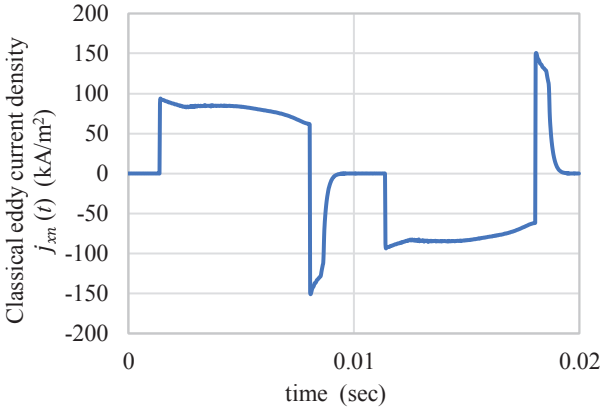

Fig. 8. The classical eddy current density $j_{xn}(t)$ on the outmost surface of steel sheet in the analysis.

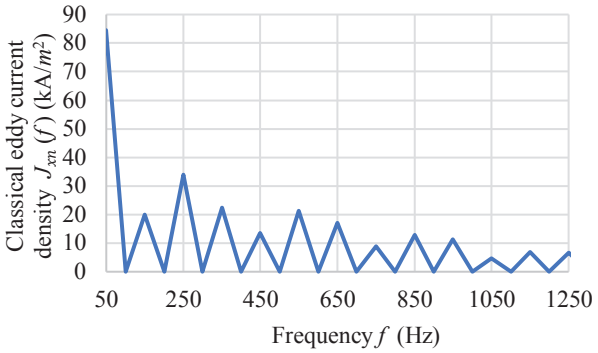

Fig. 9. The classical eddy current density $J_{xn}(f)$ on the outmost surface of steel sheet in the analysis.

The iron loss, where the NO ring core is excited at the fixed maximum flux density B_{max} = 1 T, is shown in Fig. 10. The dot plot shows the experimental results, while the bar graph shows the calculation results. The anomalous loss $W_{e,a}$, the classical loss $W_{e,c}$ and the hysteresis loss W_{hys} can be separately expressed in the order from the top of the bar graph. We see that the calculation results can well express and match the measured results under each excitation condition.

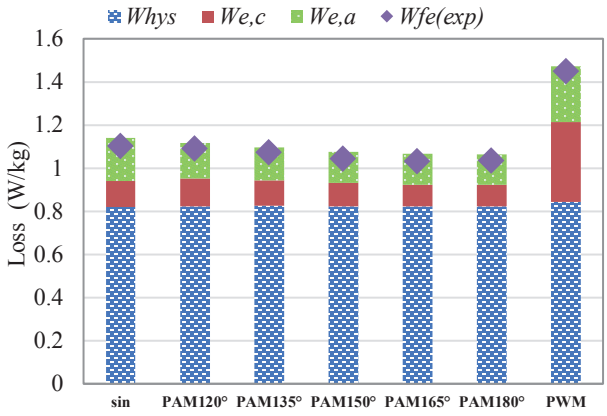

Fig. 10. Iron loss characteristics under fixed B_{max}= 1 T.

The iron loss becomes smaller in the order of the PWM inverter, sinusoidal, and PAM inverter excitation. In addition, when the PAM excitation angle increases, the iron loss decreases with the minimum value at the angle of 165°. In particular, the result demonstrates that the hysteresis loss W_{hys} has the nearly similar values in the three different excitations; however, the eddy current loss, that is the sum of $W_{e,c}$ and $W_{e,a}$, can be decreased remarkably with the PAM inverter excitation.

The relation between the measured iron loss W_{fe} and the fundamental frequency component of the flux density B_{f0} in experiments is shown in Fig. 11. These results show the same trend that the smallest iron loss point is at the excitation angle of 165° in the PAM method. It is considered that the fundamental frequency component of the flux density is reduced in the condition where maximum flux density B_{max} is fixed; hence, the fundamental frequency component of the induced electromotive voltage or the eddy current generated in the steel sheet is also reduced, and the result shown in Fig. 10 was obtained.

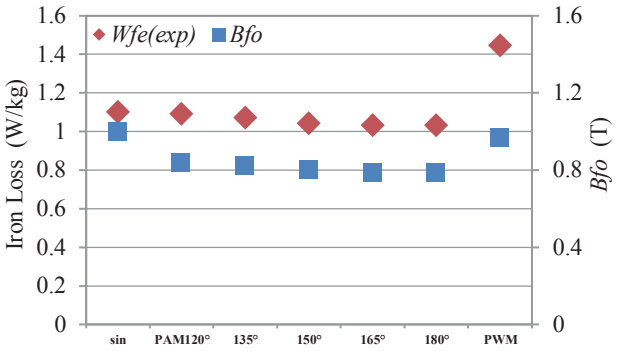

Fig. 11. Relationship between iron loss and B_{f0} in experiments.

5.2 Fixed fundamental flux density B_{f0}

In this section, the iron loss is measured while the fundamental frequency component of the flux density is fixed. The result is presented in Fig. 12, in which the square plot is the iron loss when the fundamental frequency component of the flux density is fixed at 1 T, while the triangular plot for comparison is the result when the maximum flux density is fixed at B_{max}= 1 T. When the fundamental component is constant, in the PAM excitation, the iron loss is smallest at 135°. The iron loss of constant B_{f0} condition becomes small in the order of the sinusoidal, PWM inverter and PAM inverter excitations. This trend is quite different than that with the fixed B_{max} condition. The trend of the iron loss can be considered from a point of view of harmonic components in the flux density. This phenomenon is closely related to the tendency of the total harmonic distortion (THD) of the flux density as described in Fig. 13; the THD of the flux density is defined in (9) and used to evaluate the magnitudes of harmonic components. B_{fn} means n-th flux density harmonic component ($n \geq 2$).

$$\mathrm{THD} = \sqrt{\sum_{n=2}^{N} B_{fn}^2} \Big/ B_{f0} \tag{9}$$

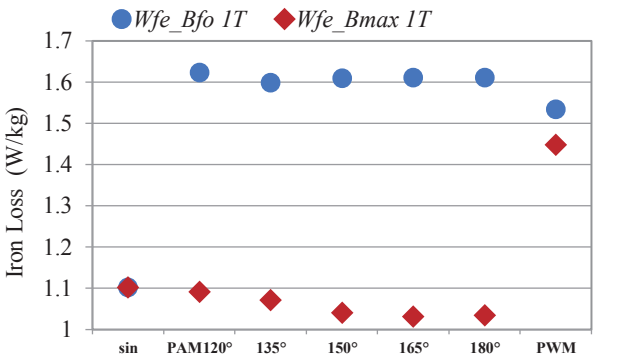

Fig. 12. Iron loss characteristics under B_{max} = 1 T and B_{f0} = 1 T.

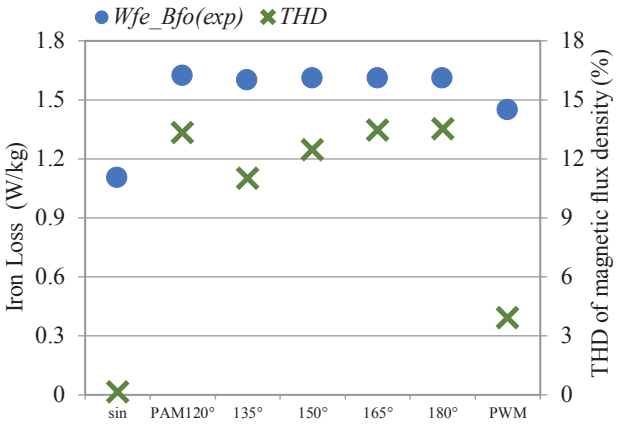

Fig. 13. Iron loss with B_{f0} = 1 T fixed and THD of flux density in experiments.

6. Conclusion

This paper has carefully studied on the calculation model considering the anomalous loss as post-processing procedure after the FEA, and it has been suitably applied to the inverter excitation evaluations, especially the PAM inverter excitation. The efficacy of the designed FEA model is verified by many experiments of the ring core. Furthermore, the calculation result can express the iron loss data obtained in experiments well.

A novel pulse pattern for the PAM inverter excitation method has been evaluated under two conditions. Firstly, under the fixed B_{max} condition often utilized as the conventional material evaluation, the iron loss in the PAM excitation is smaller than that in the PWM inverter and sinusoidal excitations, and is the smallest at the angle of 165^{o} in the PAM excitation. On the other hand, under the fixed B_{f0} condition, the iron loss becomes smaller in the order of the PWM, sinusoidal and PAM excitations, which strongly depends on the magnitudes of the time harmonic components of the flux density. This result is different than that under the fixed B_{max} condition. In future work, the effectiveness of the sinusoidal, PWM and PAM excitation methods in reducing the iron loss under the fixed-torque motor experiment will be studied and evaluated.

Acknowledgment

This work was partly supported by the Ministry of Education, Culture, Sports, Science and Technology Program, Japan, for private universities, and JSPS KAKENHI Grant Number 18K04112.

References

1) M. Kawabe, T. Noriyama, A. Shiozaki, H. Kaihara, N. Takahashi, and M. Nakano: *IEEE Trans. Magn.*, Vol. 48, No. 11, pp. 3458-3461, November 2012.
2) A. Yao, T. Sugimoto, S. Odawara, and K. Fujisaki : *AIP Advances* 8, 056804, December 2018.
3) A. M. Howladery, N. Urasaki, T. Senju, A. Yona, and A. Y. Saber : *Journal of Power Electronics*, Vol. 10, No. 5, pp. 477-484, 2010.
4) G. M. T. Nguyen, Z. Shungshuang, K. Fujisaki, F. Iwamoto, T. Kimura, and T. Yamada : *IET Electric Power Applications*, Vol. 14, No. 4, pp. 622 -637, April 2020.
5) G. M. T. Nguyen, S. Odawara, T. Endo, C. Taki, K. Fujisaki, F. Iwamoto, T. Yamada, and Y. Sasaya : *Proceedings of 2018 IEEE International Magnetics Conference*, Singapore, 2018, pp. 1-2.
6) S. E. Zirka, Y. I. Moroz, P. Marketos, and A. J. Moses : *IEEE Trans. Magn.*, Vol. 42, No. 9, ID: 880685, September 2006.
7) T. Matsuo and M. Shimasaki : *IEEE Trans. Magn.*, Vol. 41, No. 10, ID: 854892, September 2005.
8) G. Bertotti : *IEEE Trans. Magn.*, Vol. 24, No. 1, pp.621-630, January 1988.
9) S. Odawara and K. Fujisaki, T. Matsuo, Y. Shindo : *IEEE Trans. on Industry Applications*, Vol. 135, No. 12, pp.1191-1198, December 2015.
10) S. Odawara and K. Fujisaki : *IEEE Trans. Magn.*, Vol. 54, No. 5, May 2018.
11) C. Kaido : *J. Magn. Soc. Jpn.*, Vol. 33, No. 2, pp.144-149, 2009.
12) S. Odawara and K. Fujisaki : *Japanese Magnetic & Linear Drive Joint Research Symposium*, MAG-16-043, paper ID: LD-16-035, pp. 1-5, June 2016.

Received Mar. 08, 2021; Revised Mar. 23, 2021; Accepted Mar. 30, 2021

J. Magn. Soc. Jpn., **45**, 112-117 (2021)

<Paper>

A Novel Reluctance Network Model Applicable for Open Magnetic Circuits

Y. Hane, K. Sugahara*, and K. Nakamura

Graduate School of Engineering, Tohoku Univ., *6-6-11 Aoba Aramaki, Aoba-ku, Sendai 980-8579, Japan*

*Graduate School of Science and Engineering, Kindai Univ., *3-4-1 Kowakae, Higashiosaka 577-8502, Japan*

In previous research, we have developed a reluctance network analysis (RNA) to calculate various electric machines' characteristics, including electric motors, with high accuracy and high speed. However, those researches were limited to the closed magnetic circuits. This paper presents a novel RNA model for open magnetic circuits with the Kelvin transformation concept. The proposed method applies to analyzing the particle accelerator magnets, wireless power transfer systems, *etc.*

Key words: reluctance network analysis (RNA), open magnetic circuit, Kelvin transformation

1. Introduction

The finite element method (FEM) is widely used in many fields of engineering. Since its application in electrical engineering in the 1960s, it has been an essential tool in electromagnetic design and analysis. However, this method generally requires a long calculation time and a large computer memory which is a significant problem in practical use. The authors proposed a reluctance network analysis (RNA) to overcome this issue, which expresses an analytical object by one reluctance network. All the reluctances can be determined by the *B-H* curve of the material and dimensions [1]. The RNA has some advantages: simple model, fast calculation, easy coupling with external electric circuits and motion equation, *etc.* The RNA was applied to calculate various electric machines' characteristics, including transformers and motors [2)-7)]. However, the previous researches on the RNA were limited to the closed magnetic circuits, and it has never been studied for the open magnetic circuits, that is, in the case of including unlimited domain.

A wireless power transfer (WPT) system is a typical example that has open magnetic circuits. In reference 8), the RNA is applied to the WPT system analysis; however, the calculation accuracy is insufficient due to the limited analytical domain. Another example is a particle accelerator. Its electromagnet usually has a gapped iron core, which does not essentially have open magnetic circuits. However, since very high calculation accuracy is required in particle accelerators, the analytical region must be broad enough.

In order to expand the scope of application of the RNA for the WPT systems and particle accelerator magnets, this paper presents a novel RNA model for open magnetic circuits with the concept of the Kelvin transformation [9)-15)], which has been utilized in the open boundary problems in the FEM. When using the Kelvin transformation in the FEM, the analytical region is truncated by circular and spherical boundaries in two-dimensional (2-D) and three-dimensional (3-D) analysis, respectively, and connected to another exterior region. The Kelvin transformation can calculate for all the space elements, including the point at infinity, with high accuracy. Furthermore, the Kelvin transformation can have a high affinity with the RNA by extending its concept which only requires simple region transformation since the RNA has no boundary. By incorporating the Kelvin transformation into the RNA, there is no restriction on the shapes of a circle and sphere, and it is possible to analyze objects with various shapes. This paper proposes applying the Kelvin transformation to the RNA by expanding its concept, and its validity is proved by comparing the calculation results of some examples with the FEM.

Corresponding author: Y. Hane (e-mail: yoshiki.hane.e2@tohoku.ac.jp).

2. Derivation of RNA Model for Open Magnetic Circuits

In this chapter, first, the Kelvin transformation principle is described by using a 2-D analysis as an example. Next, a method for deriving the proposed RNA model incorporating the Kelvin transformation concept is described in the 2-D and 3-D analysis (here, the 3-D analysis is in the case of axisymmetric).

2.1 Principle of Kelvin transformation

Fig. 1 shows a schematic diagram of a 2-D FEM model using the conventional Kelvin transformation [9), 10)]. As shown in this figure, an analytical region including the point at infinity is divided into interior and exterior regions truncated by a circular boundary, and the unknown boundary condition connects both. Although the interior and exterior regions have the same mesh as just an example in Fig. 1, the actual analytical model does not necessarily have to be made in this way. In the figure, the interior and exterior regions' coordinate systems are (x, y) and (x', y'), respectively, where each origin is the center of the circle. Here, x' and y' are given by the following equations:

$$x' = \frac{a^2}{x^2 + y^2} x, \tag{1}$$

$$y' = \frac{a^2}{x^2 + y^2} y, \tag{2}$$

where a radius of interior and exterior regions is a.

In the previous papers, it was demonstrated that the open boundary problems can be solved by using the Kelvin transformation [9), 10)]. Moreover, this method is known to be extended to a 3-D analysis [11)-14)]. Besides, in this method, the interior and exterior regions can be separated in magnetic materials, though they are generally separated in air region[15)].

2.2 Derivation of RNA model for open magnetic circuits

The following formulation is common in 2-D and 3-D axisymmetric analysis and can be extended to 3-D analysis in general. To facilitate the RNA formulation, let the coordinate systems of the interior and exterior regions be (r, θ, z) and (r', θ', z') in a 2-D analysis, and (r, θ, φ) and (r', θ', φ') in a 3-D axisymmetric analysis, respectively. Here, each origin is the center of the circle, and each divided element is fan-shaped.

Fig. 2 shows a method for deriving the proposed RNA model for open magnetic circuits. First, as shown in Fig. 2(a), the analytical region, including the point at infinity, is divided into interior and exterior regions truncated by a circular boundary, and each is divided into multiple elements. As shown in Fig. 2(b), each divided element can be expressed in a unit magnetic circuit composed of four reluctances in the r- and θ-axis directions. The following equation gives each reluctance:

$$R_m = \frac{l}{\mu_s \mu_0 S}, \tag{3}$$

where the relative permeability of the material is μ_s, and the vacuum permeability is μ_0, and the average cross-sectional area and magnetic flux path length of each element are S and l, respectively. S and l can be determined by l_r, l_θ, l_z, l_φ, l_r', l_θ', l_z', and l_φ', which are dimensions of each element as shown in Fig. 2(b). Among them, l_r, l_θ, l_r', and l_θ' are given by the following equations, respectively:

$$l_r = |r_1 - r_2|, \tag{4}$$

$$\begin{aligned} l_\theta &= r_1 |\theta_1 - \theta_3| \\ &= r_3 |\theta_1 - \theta_3|, \end{aligned} \tag{5}$$

$$l_r' = \left| \frac{a^2}{r_1'} - \frac{a^2}{r_2'} \right|, \tag{6}$$

$$\begin{aligned} l_\theta' &= \frac{a^2}{r_1'} |\theta_1' - \theta_3'| \\ &= \frac{a^2}{r_3'} |\theta_1' - \theta_3'|. \end{aligned} \tag{7}$$

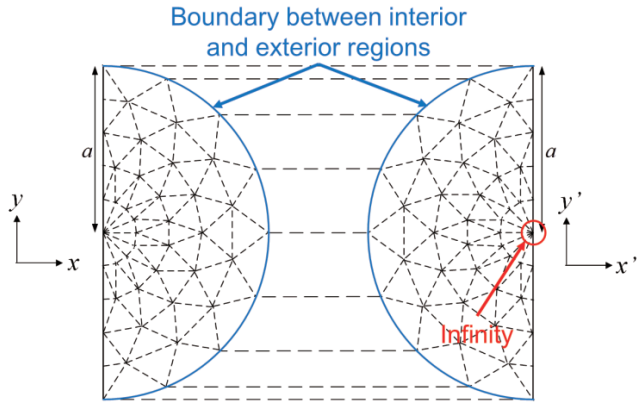

Fig. 1 Schematic diagram of FEM model using Kelvin transformation.

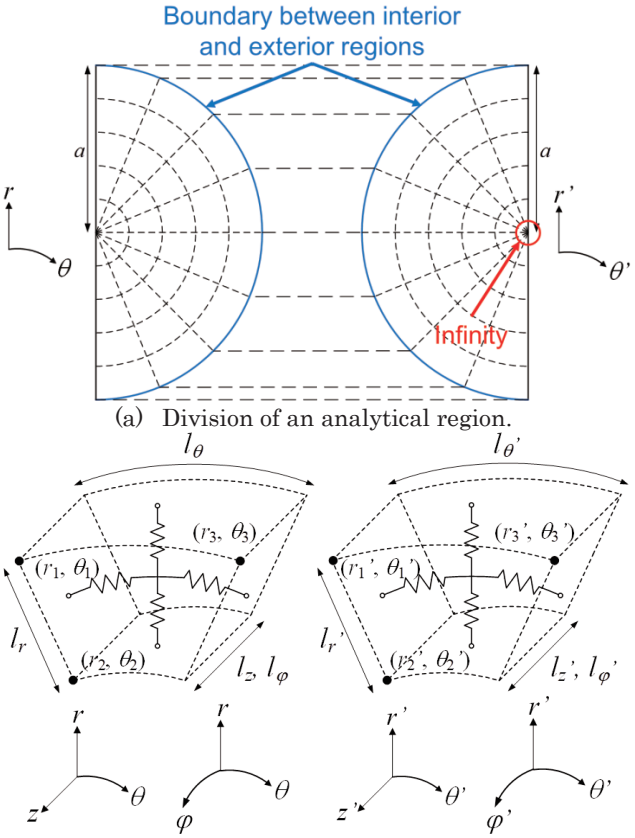

(a) Division of an analytical region.

(b) Unit magnetic circuit.
(left: interior region, right: exterior region)

Fig. 2 Derivation method of RNA model for open magnetic circuits.

Even when the element includes the point at infinity, each element's reluctances can be calculated by the above equations. Thus, in this way, the point at infinity can be expressed by only a few reluctances.

On the other hand, l_z, l_φ, l_z', and l_φ' are the thicknesses of each element in the interior and exterior regions in the 2-D and 3-D models, respectively. Among them, l_φ, and l_φ' are given by the following equations, respectively:

$$l_\varphi = 2\pi r' \sin \frac{|\theta_1 + \theta_3|}{2}, \tag{8}$$

$$l_\varphi' = 2\pi r' \sin\frac{|\theta_1' + \theta_3'|}{2}. \quad (9)$$

By using the above-derived RNA model, it is possible to analyze considering infinity. However, the RNA has a lower degree of freedom in the element shape than the FEM since a unit magnetic circuit represents each element in the RNA. Thus, it is generally difficult to construct the RNA model with only fan-shaped elements. Therefore, it is necessary to extend the above method to apply the proposed RNA model to the analytical objects with arbitrary shapes.

For example, when the analytical object has a rectangular shape, the element division, shown in Fig. 3(a), is desirable in the RNA. The RNA allows any shapes of mesh as long as the boundaries between the interior and exterior regions are common, due to the nature of the circuit. This figure reveals that the RNA has a higher degree of freedom in the model topology since it does not have complicated shape functions, unlike the FEM. In this model, there is a rectangular region at the center, and quadrant ones sandwich both sides.

In the quadrant regions, each element can be expressed in the same manner as the unit magnetic circuit shown in Fig. 2(b). On the other hand, in the rectangular region, the unit magnetic circuit can be represented as shown in Fig. 3(b). In this figure, l_x, l_y, l_z, l_φ, l_x', l_y', l_z', and l_φ' are dimensions of each element. Among them, l_x and l_x' are given by the following equations, respectively:

$$\begin{aligned} l_x &= |x_1 - x_2| \\ &= |r_1 - r_2|, \end{aligned} \quad (10)$$

$$\begin{aligned} l_x' &= |x_1' - x_2'| \\ &= \left|\frac{a^2}{r_1'} - \frac{a^2}{r_2'}\right|. \end{aligned} \quad (11)$$

Same as in the quadrant regions, in the elements including the point at infinity, the reluctances in the y-axis direction can be calculated by taking the limit values of l_x', while the ones in the x-axis direction, which are connected to the point at infinity, are open. On the other hand, l_y and l_y' are determined by only the number of divisions in the y-axis direction, not the coordinates on the x-axis. l_z, l_φ, l_z', and l_φ' are the thicknesses of each element in the interior and exterior regions in the 2-D and 3-D models, respectively. Among them, l_φ and l_φ' are given by the equations (8) and (9), respectively.

3. Simulation Results by Using Proposed Method

In this chapter, the validity of the proposed RNA model described in chapter 2 is proved. First, the analytical object composed of a bar magnet and iron is analyzed as a primary study. Next, a gapped iron core is analyzed to indicate the proposed method's applicability to particle accelerator magnets.

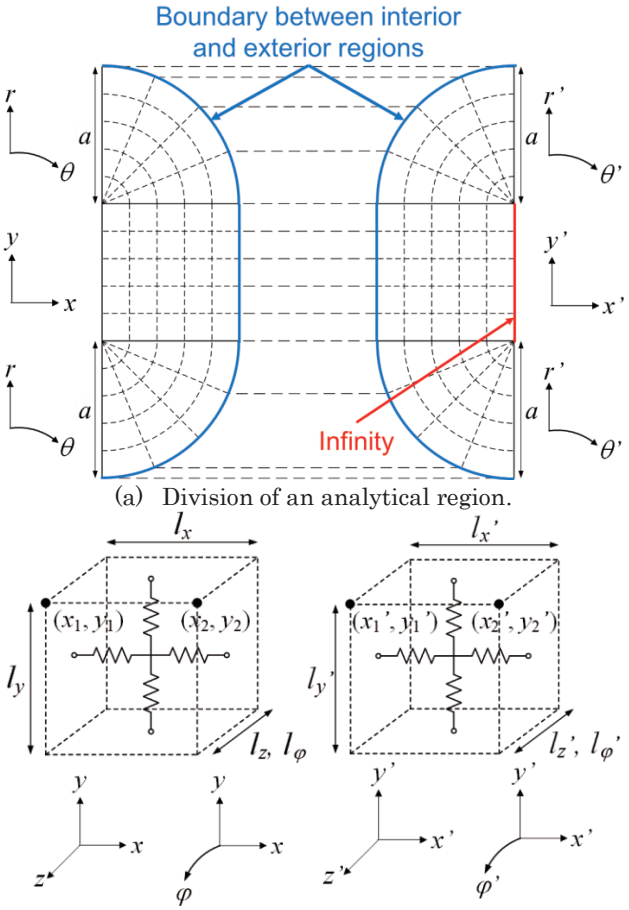

Fig. 3 An example of extension method for arbitrary shape of the proposed RNA model.

3.1 Analysis of object composed of bar magnet and iron

Fig. 4 and Fig. 5 show the analytical object's specifications and its RNA model when a = 50, 40, 30 mm, respectively. As mentioned in the section 2.1, the interior and exterior regions can be connected via not only the air but also the magnetic core [15]. Here, the MMF f_c of the magnet is expressed by the following equation using the coercive force H_c and the average magnet length l_m:

$$f_c = H_c l_m, \quad (12)$$

and inserted in series for each reluctance in the magnet in the y-axis direction.

In this section, the validity of the proposed method's calculation results is proved by comparing with those of the FEM by using the FEMM [16], which is general-purpose electromagnetic simulation software. In the FEM, the Kelvin transformation is used as the boundary condition to consider the influence of the exterior region. Here, the radius of the interior and exterior regions is a = 100 mm, which is large enough to obtain highly accurate calculation results. The distribution of the x-component of the magnetic flux density on the dashed line (x = 20 mm) shown in Fig. 4 is compared between the RNA and FEM.

Fig. 6(a) and (b) show the comparison of the

calculation results of the magnetic flux distribution of the RNA and FEM in the cases of 2-D and 3-D axisymmetric analysis. The RNA is carried out for three cases of a = 50 mm, 40 mm, and 30 mm. Besides, the RNA and FEM when there is only the internal region are also carried out for reference. From these figures, it is clear that the calculation results of the RNA hardly change even if the value of a changes within the range of the necessary and sufficient spatial resolution. Moreover, when analyzing only the internal region, the calculation results are quite different from those when considering the exterior region for both the RNA and FEM. Furthermore, comparing the RNA and FEM in the 2-D analysis, the maximum error is 1.16%, which indicates that the calculation accuracy of the proposed method is high. On the contrary, in the 3-D axisymmetric analysis, the minimum and maximum errors are 0.88% and 11.2%, respectively, which indicates that the calculation accuracy is not necessarily sufficient and has a considerable variation depending on the position. The cause of the errors is considered discretization due to constant values of l_φ and l_φ' in each element.

3.2 Analysis of gapped iron core

Fig. 7 and Fig. 8 show dimensions of a gapped iron core used for consideration and its RNA model in the core and air regions, respectively. In the air region, the point at infinity is considered by using the Kelvin transformation concept in the same way as in the previous section. In this model, the number of reluctances is 190 in the core region and 2567 in the air one. Here, the RNA model is halved in the z-axis direction due to the symmetry.

In this section, the validity of the proposed RNA model is verified by comparing the calculation results with the FEM by using the OPERA 3D [17], which is

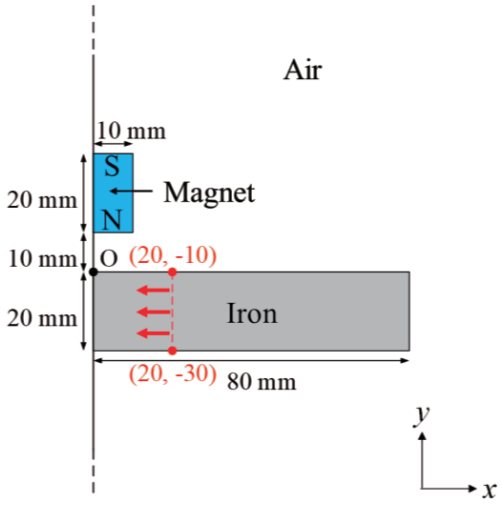

Relative permeability of iron	1000
Relative permeability of a magnet	1
Coercive force of a magnet (kA/m)	300

Fig. 4 Specifications of analytical object.

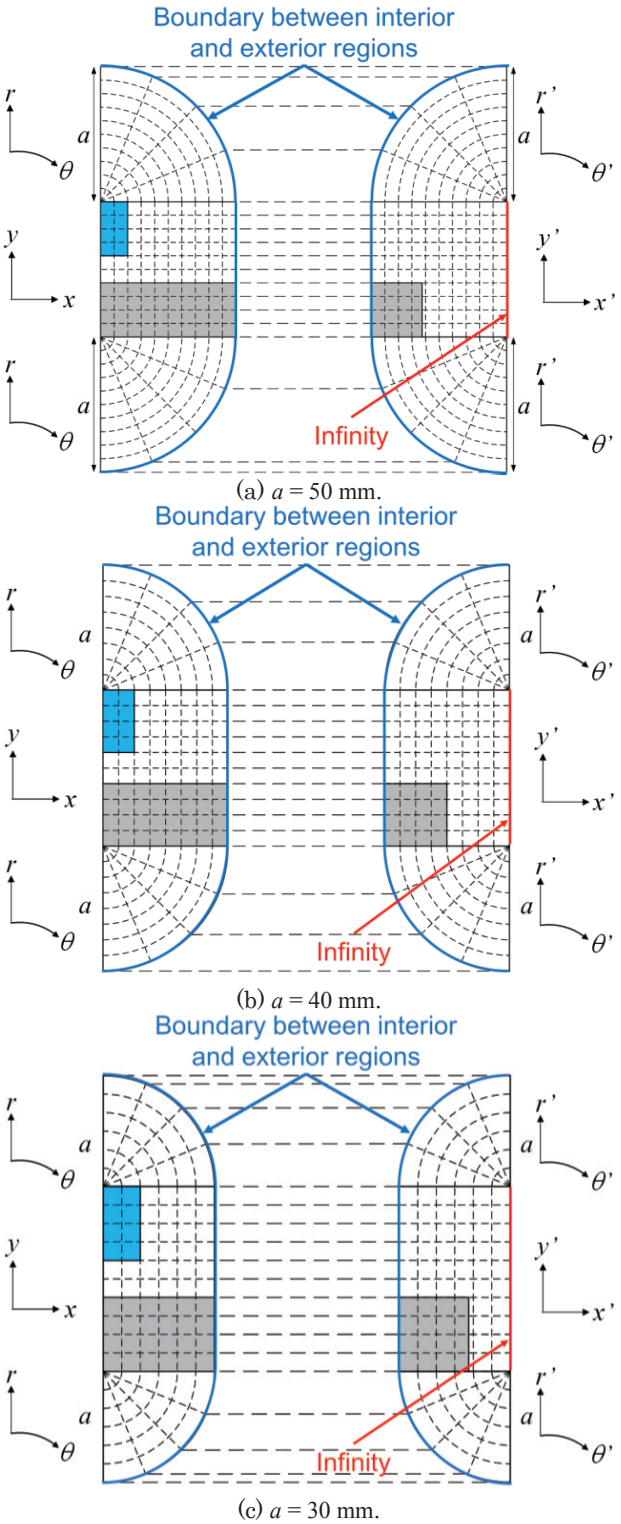

Fig. 5 Constructed RNA model.

general-purpose electromagnetic simulation software. In the FEM, the Improvised Absorbing Boundary Condition [18), 19)] is used as the boundary condition. The number of layers is eight so that the effect of the boundary edge can be reduced with necessary and sufficient accuracy. Here, as analysis conditions, the relative permeability of the iron core is set to be three cases of 100, 1000, and 10000, and the MMF of a coil is

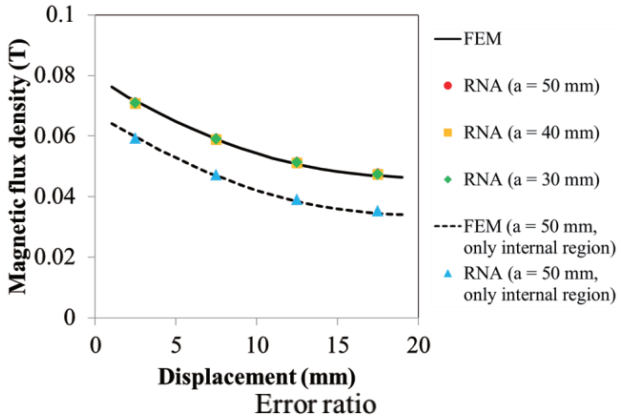

Error ratio

	a = 50 mm	a = 40 mm	a = 30 mm
2.5mm	+0.74%	+1.01%	+0.89%
7.5mm	-0.11%	+0.22%	+0.07%
12.5mm	-0.88%	-0.50%	-0.68%
17.5mm	-1.16%	-0.75%	-0.94%

(a) 2-D model.

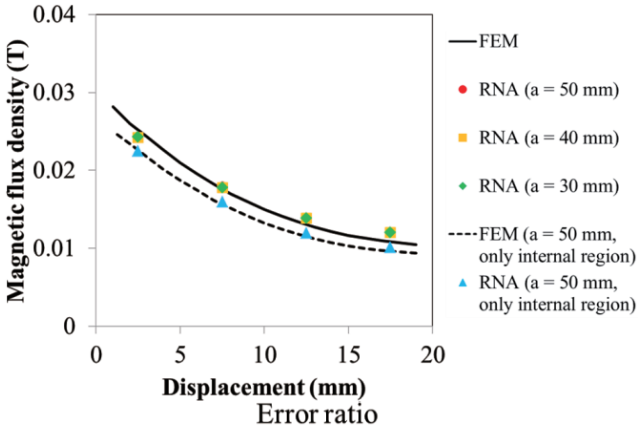

Error ratio

	a = 50 mm	a = 40 mm	a = 30 mm
2.5mm	+3.55%	+3.70%	+3.62%
7.5mm	-1.08%	-0.88%	-1.00%
12.5mm	-6.12%	-5.88%	-6.02%
17.5mm	-11.2%	-11.0%	-11.1%

(b) 3-D axisymmetric model.

Fig. 6 Comparison of calculation results of magnetic flux distribution between RNA and FEM.

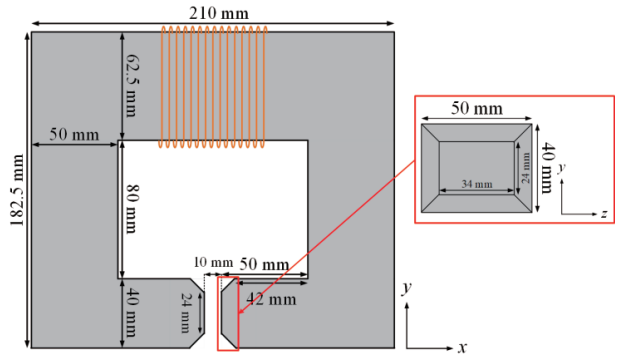

Fig. 7 Dimensions of a gapped iron core used for consideration.

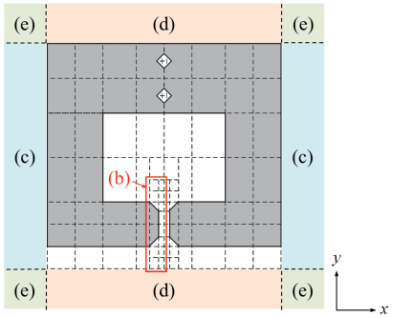

(a) Core region (x-y plane).

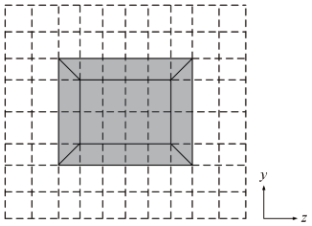

(b) Air gap region (z-y plane).

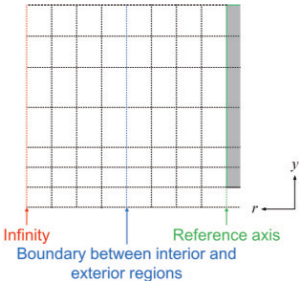

(c) Air region (r-y plane, axisymmetric).

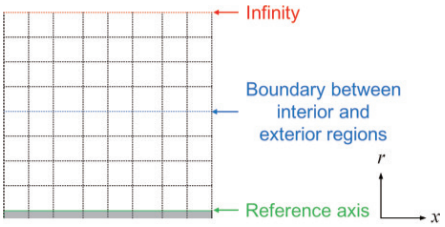

(d) Air region (x-r plane, axisymmetric).

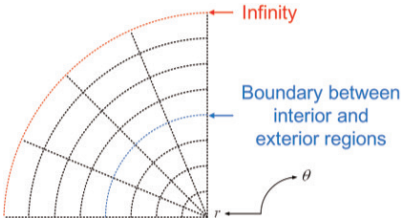

(e) Air region (r-θ plane).

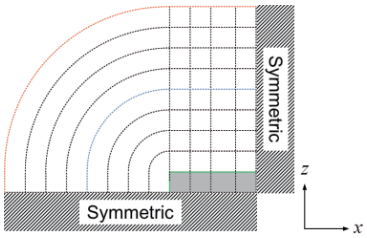

(f) Air region (x-z plane).

Fig. 8 Comparison of calculation results of magnetic flux distribution between RNA and FEM.

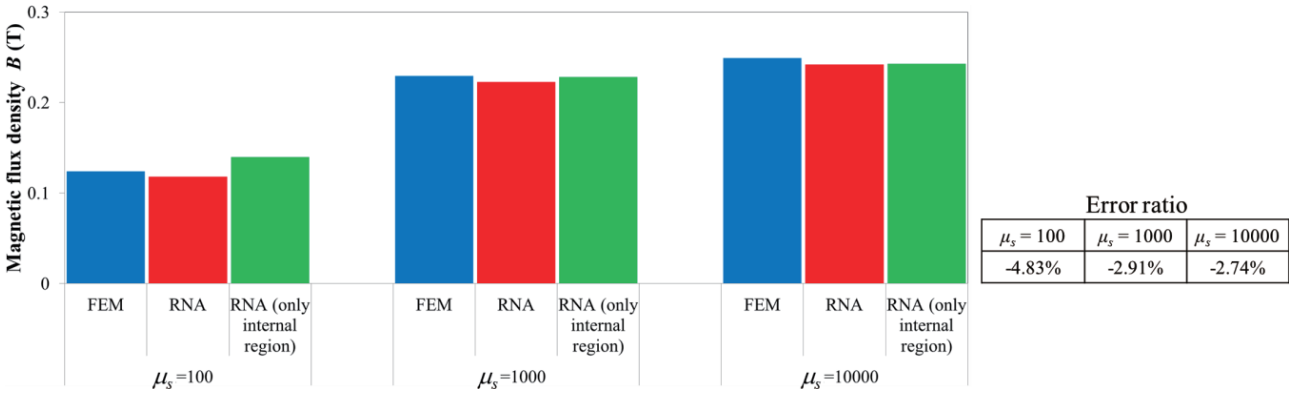

Error ratio

μ_s = 100	μ_s = 1000	μ_s = 10000
-4.83%	-2.91%	-2.74%

Fig. 9 Comparison of calculation results of magnetic flux density at the center of air gap between RNA and FEM.

2000 A.

In this section, the calculation results of the magnetic flux density at the center of the air gap are compared between the RNA and FEM. The relevant value is defined as the *x*-component of the average magnetic flux density of the elements, including the center point of the air gap in the RNA, while it is obtained from integration by using the Biot-Savart's law in the post-processing for the electromagnetic field analysis in the FEM.

Fig. 9 shows the comparison of the calculated magnetic flux density at the center of the air gap between the RNA and EFM. As shown in the figure, the maximum error is 4.9%, which is in almost good agreement. Moreover, the calculation accuracy of the RNA with only internal region reduced to 12.8% error when the relative permeability is 100. From these results, the validity of the proposed model is apparent.

4. Conclusion

This paper presented a novel RNA model for open magnetic circuits by incorporating the Kelvin transformation concept. To prove the validity of the proposed method, the analytical object, which consists of a bar magnet and iron, was analyzed as an introductory study. By comparing the calculated values between the RNA and FEM, it was clear that the errors are always about 1% or less, which is extremely high accuracy in the 2-D analysis. On the contrary, in the 3-D axisymmetric analysis, although the overall tendency is almost in good agreement, the errors at several points are more than 10% due to the discontinuity of dimensions of elements.

Next, a gapped iron core is analyzed by using the proposed method to verify the applicability to the particle accelerator magnets. As a result, it was clear that the errors of the calculated values of the gap flux density between the RNA and FEM are less than 5%, which is almost in good agreement in different permeabilities.

In the future, we aim to apply the proposed method to analyze the wireless power transfer systems and particle accelerator magnets.

Acknowledgements This work was supported by Grant-in-Aid for Scientific Research (C) (20K04454) and Grant-in-Aid for JSPS Fellows (JP19J20572).

References

1) K. Nakamura and O. Ichinokura, *IEEJ Trans. FM*, **128**, 506 (2008).
2) K. Nakamura, K. Kimura, and O. Ichinokura, *J. Magn. Magn. Mat.*, **290-291**, 1309 (2005).
3) M. Fukuoka, K. Nakamura, and O. Ichinokura, *IEEE Trans. Magn.*, **47**, 2414 (2011).
4) K. Nakamura, K. Honma, T. Ohinata, K. Arimatsu, T. Shirasaki, and O. Ichinokura, *J. Magn. Soc. Jpn.*, **38**, 174 (2014).
5) Y. Hane, H. Tanaka, and K. Nakamura, *T. Magn. Soc. Jpn.*, **2**, 25 (2018) [in Japanese].
6) Y. Hane and K. Nakamura, *Proc. IEEE Int. Magn. Conf. (INTERMAG 2018)*, 1800038 (2018).
7) Y. Hane, K. Nakamura, T. Ohinata, and K. Arimatsu, *IEEE Trans. Magn.*, **55**, 8401306 (2019).
8) K. Furukawa, K. Kusaka, and J. Itoh, *Proc. 2019 IEEE 20th Int. Symp. Power Electronics* (Ee) (2019).
9) E. M. Freeman and D. A. Lowther, *IEEE Trans. Magn.*, **24**, 2934 (1988).
10) D. A. Lowther, E. M. Freeman, and B. Forghani, *IEEE Trans. Magn.*, **25**, 2810 (1989).
11) S. H. Wong and I. R. Ciric, *COMPEL*, **4**, 123 (1985).
12) I. R. Ciric and S. H. Wong, *COMPEL*, **5**, 109 (1986).
13) E. M. Freeman and D. A. Lowther, *IEEE Trans. Magn.*, **25**, 4135 (1989).
14) K. Sugahara, *IEEE Trans. Magn.*, **49**, 5399 (2013).
15) K. Sugahara, *dengakukenshi*, SA-20-38/RM-20-62 (2020) [in Japanese].
16) D. Meeker, Finite element Method Magnetics, https://www.femm.info/wiki/HomePage.
17) J. Simkin and C. W. Trowbridge, *IEE Proc. B – Elec. Power Appl.*, **127**, 368 (1980).
18) D. Meeker, *IEEE Trans. Magn.*, **49**, 5243 (2013).
19) K. Sugahara, *IEEE Trans. Magn.*, **53**, 7205604 (2017).

Received Mar. 15, 2021; Revised Apr. 20, 2021; Accepted Apr. 30, 2021

Journal of the Magnetics Society of Japan

Vol. 45 No. 4 (通巻第316号) 2021年7月1日発行

Vol. 45 No. 4 Published Jul. 1, 2021
by the Magnetics Society of Japan
Tokyo YWCA building Rm207, 1–8–11 Kanda surugadai, Chiyoda-ku, Tokyo 101–0062
Tel. +81–3–5281–0106 Fax. +81–3–5281–0107

Printed by JP Corporation Co., Ltd.
Sports Plaza building 401, 2–4–3, Shinkamata Ota-ku, Tokyo 144–0054
Advertising agency: Kagaku Gijutsu-sha

発行：（公社）日本磁気学会 101–0062 東京都千代田区神田駿河台 1–8–11 東京YWCA会館 207 号室
製作：ジェイピーシー 144–0054 東京都大田区新蒲田 2–4–3 スポーツプラザビル401 Tel.（03）6715–7915
広告取扱い：科学技術社 111–0052 東京都台東区柳橋 2–10–8 武田ビル4F Tel.（03）5809–1132